University Of Trento

Department of Cellular, Computational and Integrative Biology (CIBIO)

International PhD Program in Biomolecular Sciences

XXXV Cycle

Recombinant DDX58 associates with SOD1 protein and selective miRNA changes in secreted EVs

Tutor

Prof. Vito Giuseppe D'Agostino

CIBIO – University of Trento

PhD thesis of

Fabrizio Fabbiano

CIBIO – University of Trento

Academic Year 2022 – 2023

Declaration of original authorship

I, Fabrizio Fabbiano, confirm that this is my own work and the use of all material from other sources have been properly and fully acknowledged.

Fabrizio Fabbiano

Table of contents

List of figures

ABSTRACT

Amyotrophic lateral sclerosis (ALS) is a neurodegenerative disease which results in the focal degeneration of motor neurons. The contribution of different cell types in the disease progression leads to hypothesize non-cell-autonomous defects, and possibly intercellular miscommunication. Extracellular Vesicles (EVs) are cell-secreted nanosized heterogenous particles proposed as vehicles of neurotoxic cargoes contributing to ALS progression. EVs are ubiquitously released by cells and can be detected in biofluids. Their biological content, reflecting the cell of origin, includes proteins, lipids, and nucleic acids, and could represent a precious source of disease biomarkers. The vesicular RNA content can be intended as a result of the post-transcriptional control exerted by RNA-binding proteins at intracellular level.

Here, we studied a novel EV-associated function for DExD/H-Box Helicase 58 (DDX58) RNA-binding protein, also known as RIG-I (retinoic acid inducible gene I). DDX58 is a cytosolic RNA sensor involved in innate immunity against viruses. Upon viral RNA (as well as host ncRNA) binding, it associates to mitochondria and activates the interferon response. Interestingly, DDX58 recently emerged as a novel RBP associated to ALS, as it was found upregulated in SOD1 and TDP-43 ALS models. Therefore, we decided to investigate DDX58 in connection to EVs and their paracrine effects.

In NSC34 cells, we observed that recombinant DDX58-tGFP displays an intracellular distribution that partially reaches the organelle-enriched fraction of the endogenous Ddx58. We showed DDX58 local interactions with wt and G93A mutant SOD1 proteins, but not with TDP-43. By processing the cell secretome with orthogonal approaches for EV isolation, we found that DDX58 is included as EV cargo and influences SOD1 protein EV-enrichment. Interestingly, we observed that an acute overexpression of recombinant DDX58 resulted in significant EV-RNA release, further enhanced upon DDX58-tGFP and SOD1 G93A co-expression. This increase was also confirmed in the secretome of SOD1 G93A mouse primary astrocytes. RNA from NSC34 and astrocyte cellular models, along with corresponding EVs samples, was therefore analysed by RNA-Seq. Exploiting FACS, we included tGFP-positive and negative NSC34 cells and corresponding EVs samples.

From tGFP-sorted cells, we identified clusters of differentially expressed miRNAs at intracellular level but with surprisingly no effect on EV release, except for a couple of miRNA targets. In astrocytes EVs, we identified 8 miRNAs modulated upon G93A mutation. Interestingly, in NSC34, DDX58 and SOD1 G93A co-expression resulted in a significant enrichment of miRNA transcripts in EVs compared to DDX58 overexpression, confirming an indirect role of SOD1 in EV-miRNA trafficking. We started a preliminary validation of DDX58-associated miRNAs in HEK293T cells and iPS-derived motor neuron progenitors. In mature motor neurons, we also observed increased DDX58 mRNA upon TDP-43 silencing.

In conclusion, we explored the involvement of DDX58 in EV biology, describing some molecular clues of selective EV-RNA and protein cargo in ALS cellular models.

1. INTRODUCTION

1.1 Amyotrophic Lateral Sclerosis: pathophysiology and progression

Amyotrophic Lateral Sclerosis (ALS) is a neurodegenerative pathology resulting in the cellular death of both upper and lower motor neurons. Being the most common motor neuron disease, it affects 2 out of 100,000 persons worldwide every year (Mead et al. 2023). The histopathological features of ALS are complex, though clinicians agree that the degeneration originates in a precise district of the central nervous system (CNS) and then diffuses focally in the brain and spinal cord (Eshima et al. 2023). Heterogeneity also characterizes ALS onset and progression.

ALS is one of the most frequent neurodegenerative disorders in middle-adult life, with onset in patients in the late 50s. Nevertheless, there are juvenile cases occurring in the late teenage years, not always indicating a clear hereditary linkage. Indeed, 90% of ALS cases is defined as “sporadic” (or sALS) in contrast to cases with reported genetic association defined as “familial” (fALS) (R. H. Brown and Al-Chalabi 2017). Recently, studies on ALS heritability are suggesting that up to 50% of the total cases shows an estimated genetic heritability that, in the case of sALS is mainly based on rare variants (Ryan et al. 2019).

Clinical ALS manifestations include cognitive involvement in roughly 50% of the cases, in fact behavioral impairment symptoms in ALS are overlapped with frontotemporal dementia (FTD) in a condition known as ALS-FTD spectrum disease (Goldstein and Abrahams 2013).

Clinically, patients are classified as fast or slow progressors depending on the disease progression and survival. A median of 2 to 4 years after the onset is reported as survival time in the literature, but it is remarkable that a sixth of patients survives longer than ten years (Witzel et al. 2022). The impairment of lower motor neurons is associated with a shorter prognosis as well as behavioral symptoms correlate with more aggressive

progression. The etiology of this phenomenon is multifactorial, although pathogenetic variants among familial cases have been described (Witzel et al. 2022). Even though a small percentage of ALS cases is acknowledged as fALS, most of their molecular features and hallmarks are well recapitulating the sporadic pathogenesis.

Up to now, >30 genes have been described as causative of ALS, representing an estimated 60-70% of the 10% defined as familial (Mead et al. 2023). Nevertheless, research is also highlighting rare genetic variants through genome wide association studies (GWAS) (van Rheenen et al. 2021).

Among the most important ALS-related genes, TARDBP is the human gene locus encoding for TDP-43 protein and is mutated in familiarities of both motor neuron disease and rare FTD cases, and specifically accounts for 5% of fALS. TDP-43 in ALS patients form ubiquitinated and phosphorylated inclusions in neurons and, marginally, in glial cells, recognized as a hallmark of the disease (Tamaki and Urushitani 2022). TDP-43 is a DNA/RNA binding protein belonging to heterogenous nuclear ribonucleoprotein (hnRNP) family and is involved in a plethora of functional processes in the cell. In ALS-FTD TDP-43 shows both gain of toxic functions and loss of physiological activity that trigger neuronal death. The nuclear depletion of the protein alters its role in the regulation of RNA processing and allows the formation of the post-translationally modified aggregates. This mechanism is responsible for the aberrant proteostasis, oxidative status and metabolic functionality in TDP-43 models (Tamaki and Urushitani 2022).

Historically, SOD1 was the first gene associated to ALS in early 1990s (Rosen et al. 1993). Up to 20% of fALS cases show mutations in this gene, encoding for the antioxidant enzyme Cu, Zn superoxide dismutase (Berdyński et al. 2022). SOD1 protein is involved in the response against reactive oxygen species (ROS) and is ubiquitously expressed in the body. Apparently, patients harboring mutant SOD1 protein suffer from a gain of function due to toxic oligomers of misfolded SOD1 and partially from a lack of active protein (Berdyński et al. 2022). Misfolded SOD1 generates oxidative stress, mitochondrial dysfunction with consequent axonal transport defects and impairment of proteasome homeostasis among other alterations (Mead et al. 2023). Interestingly,

SOD1 mouse models fail to recapitulate TDP-43 proteinopathy which is a *quasi*-ubiquitous clinical manifestation (present in more than 97% of all ALS subtypes) characterized by cytoplasmic inclusions of TAR DNA binding protein 43 (Mead et al. 2023).

Independently from the genetic background, several biological pathways have been associated to ALS: 1) oxidative stress; 2) dysregulation of mitochondrial function; 3) protein homeostasis; 4) RNA processing; 5) axonal transport and nucleocytoplasmic transport (NCT); 6) neuroinflammation; 7) excitotoxicity; 8) DNA damage.

1.2 Molecular features of ALS

1) **Oxidative stress** results from impairment of the natural defenses against reactive oxygen or nitrogen chemical species. ROS significantly affect the viability of CNS neurons as they are responsible for peroxidation reactions damaging cells at the lipid, protein and nucleic acids level. Oxidative stress is also shown to alter the post-translational modification (PTM) status of TDP-43 increasing the degree of acetylation and phosphorylation. Such biochemical conditions compromise the RNA binding properties and aggregation propensity of TDP-43 (Tamaki and Urushitani 2022). In addition, neuroinflammation can trigger the increase of oxidation byproducts formation like the activation of myeloperoxidase expressing glial pro-inflammatory cells (Xiong et al. 2022).
2) Excessive generation of ROS is strictly linked to **altered mitochondrial function** which is a determining molecular feature of ALS. Axonal degeneration occurs following energy supply disruption upon mitochondria network perturbation. Mutations in SOD1 protein are reported to reduce the function of the electron transport chain in the mitochondria membrane. Similarly, also C9ORF72-derived dipeptide repeats and TDP-43 protein localize in the inner mitochondria membrane and affect the activity of respiratory complex I (Tamaki and Urushitani 2022)(W. Wang et al. 2016). Besides, TDP-43 sequestration in the

cytosol creates altered post-transcriptional regulation of mitochondrial proteins expression (Tamaki and Urushitani 2022).

3) The accumulation of incorrectly folded proteins due to **deficits in the protein quality control (PQC)** system is a common feature in ALS. Many of the proteins associated with the disease are indeed substrate of the pathways that regulate the presence of aberrant protein products in aging cells (Tamaki and Urushitani 2022). The relative expression of ubiquitin proteasome complex proteins in motor neurons could explain an enhanced susceptibility of these cells to PQC disruption mechanisms (Brockington et al. 2013). Proteins like TDP-43 and FUS show an increase proneness to form phase separation inclusions due to the presence of low-complexity domains in their primary sequence. Such prion-like domains facilitate the co-aggregation of these proteins in stress-induced membraneless organelles termed stress granules (SGs). SGs are formed by multiple RNA and protein species and are dynamic structures originated in response to stress. The availability of misfolded proteins in the cytoplasm is responsible for SGs missing disassembly in ALS, together with the impaired ALS autophagic degradation (Baradaran-Heravi, Van Broeckhoven, and van der Zee 2020).
4) **RNA metabolism** is of key importance in the definition of ALS. RNA-binding proteins (RBPs) are trans-acting factors regulating the fate of many RNA species. ALS-RBPs such as TDP-43 and FUS are involved in stability, export, splicing and biogenesis of microRNAs. It does not surprise how the generalized dismantling of the functionality of such RBPs in ALS generates a cascade of altered gene expression. In addition, RNA foci have been described in C9ORF72 genetic variants which act as sequestration sponges of RBPs and other RNA maturation factors (Tamaki and Urushitani 2022). TDP-43 dysfunctions are associated with the creation of cryptic exons deriving from aberrant splicing processing of transcripts, as demonstrated for example by Brown et al for UNC13A mRNA (A. L. Brown et al. 2022).
5) **Defective transport** is observed in ALS at the level of NCT machinery, endosomal vesicular pathway and axonal structure. Enhanced exportin 1 activity is responsible for augmented TDP-43 cytoplasmic mislocalization, thereby exportin

1 is a promising therapeutic target to prevent TDP-43 aggregates. Exportin 1 works in concert with Ran GTPases present in the nucleoplasm which determine the rate of nuclear export across the nuclear pore complex (NPC). In ALS, the integrity of the NPC is compromised and the gradient of GTPases is altered. This was observed initially in G4C2 C9ORF72 expansions genetic variants (the most common ALS genetic cause) and later on also in TDP-43 and sporadic models (Tamaki and Urushitani 2022) (Fallini et al. 2020). Almost one third of confirmed risk genes happens to be encoding for proteins involved in intracellular trafficking. TDP-43 regulates the maturation and exocytosis of synaptic vesicles that, in turn, affect neurons excitability. Also, axonal transport is perturbed in ALS pathophysiology. Pharmacological strategies to ameliorate the integrity of microtubules in ALS patients' neurites are currently under investigation since, interestingly, axonal accumulation of organelles upon impaired retrograde endosomal trafficking is observed in multiple models (Tamaki and Urushitani 2022).

6) Post-mortem imaging revealed evidence of **neuroinflammation** in most of ALS specimens. In particular, it is possible to observe extensive astrogliosis and microglia M1 neurotoxic phenotype activation (Hardiman et al. 2017). The switch from neuroprotective to neurotoxic phenotype in SOD1 transgenic mice occurs during disease onset and is a putative trigger for faster disease progression. Consequently NF-κB activation in microglia leads to worsen prognosis in the animals, being a master regulator of pro-inflammatory gene transcription. Additionally, both TARDBP and C9ORF72 protein products are involved in cGAS-STING derived immune response, by either activating the pathway upon generating mtDNA release (TDP-43 case), or preventing STING degradation (C9ORF72 case) (Tamaki and Urushitani 2022)(McCauley et al. 2020). Loss-of-function mutations occurring in ALS hamper this physiological role which could partially explain such an increased susceptibility of patients towards glial activation.
7) **Excitotoxicity** is the process through which hyperstimulation of postsynaptic glutamate receptors results in excessive calcium intake. Motor neurons present a lower calcium buffering ability as they express more Ca^{+2} permeable AMPA

receptors (Nijssen, Comley, and Hedlund 2017). Furthermore, EAAT2, the main astroglial glutamate reuptake transporter is impaired in ALS mouse models and patients. However, it is unclear whether excitotoxicity is a common hallmark to all ALS subtypes or is just an indirect indication (Hardiman et al. 2017).

8) Several markers of **DNA damage** response (DDR) have been associated with ALS. Oxidized deoxyguanosine, apurinic/apyrimidinic sites were reported in patients' biofluids, as well as yH2AX histone foci (a marker of DNA repair) and R-loops formation (DNA-RNA hybrids prone to double strand break) were described in C9ORF72 and TDP-43 models (Mead et al. 2023). In addition, liquid-liquid phase separation (LLPS) characterizing neurodegenerative disease like ALS and driven by aggregation-prone low complexity domains is proposed to generate DDR as shared DNA repair factors are altered in similar pathological conditions such as Alzheimer's or Huntington disease (Pessina et al. 2021).

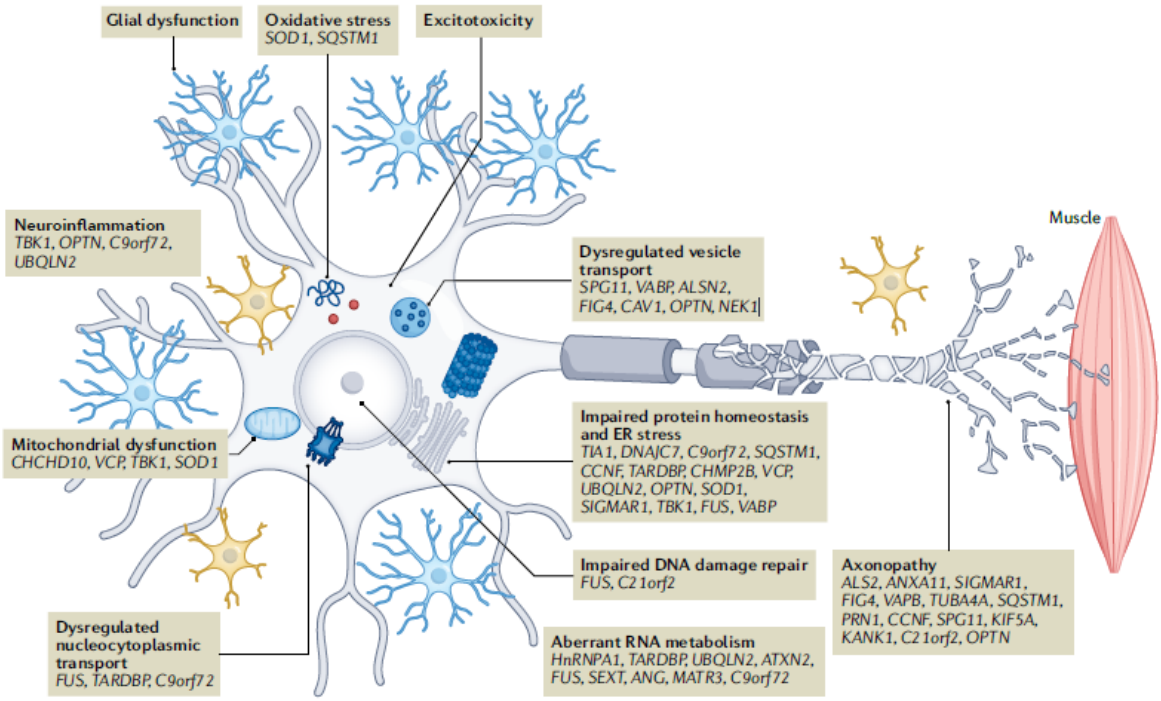

Figure 1.1 ALS-associated molecular hallmarks and pathogenetic mechanisms. *Whole genome sequencing highlights the different familial genes identified. Genetic variants are associated to key dysregulation common to motor neurons and neighboring cells. Adapted from Mead et al. 2023*

Besides motor neural-borne intracellular dysfunctions, the attention of the ALS scientific community has shifted towards a more comprehensive view of the pathophysiology. In

particular, non-neuronal cells-dependent mechanisms are being described and defined as non-cell autonomous ALS dysfunctions.

1.3 ALS non-cell autonomous disease hypothesis

Studies conducted with transgenic mouse models indicated the involvement of non-neuronal cells in ALS pathogenesis. (Weydt et al. 2004). Although a withstanding neurocentric view of the disease exists, evidence of mechanisms involving cells other than motor neurons (MNs) gave rise to the so-called non-cell autonomous disease hypothesis, involving a combination of neuronal intracellular defects and inter-cellular events. An initial hint came from non-neuronal wild type glial cells extending the survival of mSOD1 cells in vitro, as well as wt MNs acquiring protein aggregates when exposed to mSOD1-expressing non-neuronal cells (Van Harten, Phatnani, and Przedborski 2021) (Weydt et al. 2004). It is notable that a neuron-restricted deletion of mSOD1 in transgenic mice is sufficient to delay the onset of the disease, even if paralysis develops with signs of protein aggregation in MNs. This supported the hypothesis that *in vivo* there must be mechanisms by which cells other than MNs are able to induce phenotypic alterations towards receiving cells (Van Harten, Phatnani, and Przedborski 2021).

Astrocytes, microglia and peripheral blood cells are among the non-neuronal cells supposed to affect the wellbeing of MNs. Studies to investigate this hypothesis usually generate a cell-type specific deletion of ALS mutant protein expression. For example, selective removal of mSOD1 from astrocytes of SOD1 transgenic mice is able to extend the survival of the animals. Interestingly, in this context different SOD1 mutants with distinct biochemical properties showed variable onset outcomes (L. Wang, Gutmann, and Roos 2011). Studies on TDP-43 mutant primary cultures and human induced pluripotent stem cells (iPSCs)-derived MNs and astrocytes co-cultures prove that similar gain-of-function and loss-of-function neurotoxic mechanisms exist also in astrocytes from TDP-43 models (Vahsen et al. 2021). It cannot be excluded that astrocytes neurotoxicity is exerted upon the interaction with other non-neuronal cell types such as

microglia or non-glial immune cells. In a key study on SOD1 model, microglia bearing misfolded aggregates was demonstrated to create a pro-inflammatory environment by secreting soluble factors in the culture media (Xiao et al. 2007). Finally, monocytes and macrophages derived from the peripheral blood of ALS patients have shown pro-inflammatory profiles, concordantly with the production of immune-attractive chemokines in the brainstem and consequent infiltration of monocytes (Vahsen et al. 2021). Also, in slow progressors, Treg CD4+ cells are increased; this induces the maturation of M2 neuroprotective microglial phenotype. Conversely, in shorter prognosis cases, M1 cell type is favored by the depletion of Treg cells suggesting how the dysfunctional crosstalk between immune cells affects the progression of cell death in a non-neuronal autonomous way (Vahsen et al. 2021).

The most accredited hypothesis is that cell death originates upon a two-way crosstalk between MNs and the surrounding cells. This does not rule out MN-autonomous toxicity. It is still unclear why MNs are selectively affected by glial and non-glial cells with respect to other less vulnerable neuronal cell types.

Nevertheless, much effort is needed to elucidate how cell secreted factors control cell-to-cell miscommunication in ALS.

Extracellular vesicles are proposed as an attractive tool to intercept mechanisms by which the MN-surrounding cell network affects the onset, progression and follow-up of the disease.

1.4 Extracellular Vesicles (EVs): biogenesis and content

Extracellular vesicles (EVs) are heterogeneous membranous particles composed of lipid bilayers secreted by cells. EVs are found in all biofluids and take part to various biological processes. Their content reflects the one deriving from the EV-secreting cells, and includes proteins, lipids, and nucleic acids. According to the tissue of origin, physiology and EV subtypes the constituents of EVs differ in a highly dynamic manner (Abels and Breakefield 2016). Current classification divides EVs in three main subtypes: exosomes, microvesicles, and apoptotic bodies. There is not a clear distinction as the populations

are often overlapped in terms of size and the absence of unilateral biomarkers hampers a net separation. An active discussion is present in the literature on the use of “small EVs” and “large EVs” (sEV and lEV) , while the generic term EVs is preferred (Théry et al. 2018).

Exosomes are EVs usually defined with a 30–100 nm diameter and derive from the endosomal pathway. They originate from invagination of intraluminal vesicles (ILVs) in the core of multivesicular endosomes (MVEs). The endosomal sorting complex required for transport (ESCRT), is implicated in the maturation of early endosomes towards MVEs. It is a protein machinery made out of more than thirty proteins operating in four subcomplexes. Specifically, the ESCRT-0 and ESCRT-I subunits recruit cargo proteins to the membrane of MVEs by means of ESCRT-I TSG101 protein. TSG101 tether the ESCRT-III subcomplex, bridging it through the ESCRT-II. After the whole complex formation budding and fission occurs (Christ et al. 2017). Ubiquitinated membrane and soluble proteins are packaged in EVs exploiting an ESCRT-dependent process, to which other accessories proteins like syntenin and ALG-2 interacting protein X (ALIX) are involved to sustain the invagination and the membrane curvature formation. Footprints of the complex functioning are found as protein cargoes of EVs at different maturation steps and are recognized as EV protein markers (van Niel et al. 2022).

Nevertheless, knock-out experiments to delete ESCRT subcomplexes protein members revealed that exosomes are formed also in an ESCRT-independent way (Van Niel, D’Angelo, and Raposo 2018). This comprises the activity of neutral type II sphingomyelinases (nSMases) that convert sphingomyelin into ceramide responsible for enhanced membrane negative curvature. Syntenin and ALIX are involved also in the ESCRT-independent cargo sorting. Tetraspanins (transmembrane proteins spanning the lipid bilayer in four helices) like CD63, CD81, CD9 direct the formation of exosomes by creating protein microdomains that cluster the cargo without involving the ESCRT complex (Van Niel, D’Angelo, and Raposo 2018).

MVEs’ fate after maturation is diverse: they can be directed to degradation in lysosomes or autophagosome to recycle its constituents or docked to the plasma membrane for fusion and consequent release of exosomes in the extracellular milieu. Rab-GTPases are proteins affecting the directionality of MVEs and controlling the vesicular intracellular trafficking. Rab11, Rab35, Rab27a have been shown to actively regulate the docking of

MVEs towards extracellular release. Soluble NSF-attachment protein receptor (SNARE) proteins are instead responsible for the fusion with the plasma membrane and ILVs secretion (van Niel et al. 2022).

Microvesicles (MVs) are defined in a size range of 100-150 up to 1000 nm. A different biogenesis is observed for cell membrane budding microvesicles. Similarly to exosomes the process can involve the ESCRT machinery, except for the absence of ESCRT-0 to recognize ubiquitylation. A Ca2+-dependent rearrangement of cytoskeleton is necessary as well as the action of enzymes required for membrane plasticity known as flippases or scramblases (Jin et al. 2022). These modifications alter the symmetric disposition of phospholipids in the bilayer and destabilize the local surface tension, rendering the vesicle conformation thermodynamically more favored. In astrocytes, the activation of acid sphingomyelinase was shown to generate an ESCRT-independent microvesicles budding. Small GTPases like Rho-associated protein kinase (ROCK) are required to finalize the secretion of MVs (van Niel et al. 2022).

The biomolecular content of EVs is mainly characterized by proteins, lipids and nuclei acids passively of actively loaded as EV cargo prior secretion.

Proteins

Vesicular proteins are present both as transmembrane of lipid-anchored insoluble proteins and as luminal soluble proteins. In a recent quantitative proteomic analysis carried out on 14 human cell lines derived EVs, almost 1200 common ubiquitous proteins were identified in exosomes. Among these, tetraspanins heterogeneity reflected that of the cells of origin, whilst biogenesis proteins (especially syntenin-1) can be considered exosomes biomarkers across different cell lines derived from different tissues. Interestingly, other members, identified as ubiquitous, belong to biogenesis mechanisms such as GTPases, ESCRT members, SNARE members; or to stabilizing functions which could be necessary to all EVs as for the case of CD47, protecting EVs from phagocytosis (Kugeratski et al. 2021). Abundance of cations channels packed in the membrane of secreted vesicles has also been reported in other circumstances, as well as for aquaporin water channels (Clarke-Bland, Bill, and Devitt 2022). At the luminal

level, EVs contain heat shock proteins (HSP), cytoskeleton components and other cytosolic abundant proteins (Yáñez-Mó et al. 2015). Interestingly up to 25% of EV protein content present RNA binding features (Sork et al. 2018). A dedicated section around EV packaged RNA-binding proteins will be implemented in the paragraph 1.6.

Importantly, besides the protein content derived from EV-secreting cells, EVs acquire a surface protein cargo in biofluids, constituting in this way the so-called EV protein corona. Indeed, EV preparations from plasma present a high number of blood-derived proteins such as lipoproteins or serum albumin (Onódi et al. 2018). There is an active discussion regarding whether the surface interactome constitutes inherent EV content or a purification contaminant (Tóth et al. 2021). It is widely demonstrated, though, that the depletion of protein corona from plasma-EVs can functionally affect the properties of vesicles in terms of pro-inflammatory effect (Tóth et al. 2021) or angiogenesis and tissue regeneration (Wolf et al. 2022).

Lipids

As for the lipid content, most of EVs are enriched with phosphatidyl serine, sphingomyelin, cholesterol, and ceramide. These lipids are often organized in detergent-resistant raft like structures which confer stability to the membrane (Donoso-Quezada, Ayala-Mar, and González-Valdez 2021) and forming lipid microdomains that are involved in EVs secretion and function (Ouweneel, Thomas, and Sorci-Thomas 2020). A specific reference goes to ceramide, as already said, implicated in ESCRT-independent exosomes biogenesis. In addition, ceramide forms subdomains in the endosomal membrane that guides RNA cargo segregation and proteolipid protein sorting (Horbay et al. 2022).

Nucleic Acids

Nucleic acids, mostly RNA, represent a precious cargo delivered through secreted vesicles. Vesicular RNA is secreted by different cell types and depends on their physiological/pathological state. It reflects the cellular RNA content of the donor cell, but also EV specific sequences characterize EVs transcriptomics, while they present differences in the relative abundance of cell-derived transcripts (Sork et al. 2018). Both

coding and non-coding entries are found in the main databases like Vesiclepedia (http://microvesicles.org). In 2023, the website reports 27,646 mRNAs and 10,520 entries for microRNAs (miRNAs) registered as found in EVs. (Fabbiano et al. 2020). MicroRNAs are not the only class of ncRNAs represented inside EVs: Y-RNAs, transfer RNAs (tRNAs), piwi-interacting RNAs (piRNAs) small nuclear RNAs (snRNAs), small nucleolar RNAs (snoRNAs), long noncoding RNAs (lncRNAs), circular RNAs (circRNAs), but also ribosomal RNAs (rRNAs) were all described in transcriptomic analyses of EV-RNA (Pérez-Boza, Lion, and Struman 2018). For some of them, specific functions have been associated to their presence in EVs and consequent delivery to recipient cells, as in the case of intact mRNAs or miRNAs. Nevertheless, bioinformatic analysis have clarified the relative abundance of fragmentation products in EV-RNA, that would reasonably imply that some extent of degradation-derived non functional RNAs could be loaded in EVs as recycling material (O'Brien et al. 2020).

Messenger RNAs were initially discovered in EVs as intact RNAs and their functional delivery to recipient cells was demonstrated in glioblastoma cells by Valadi et al (Valadi

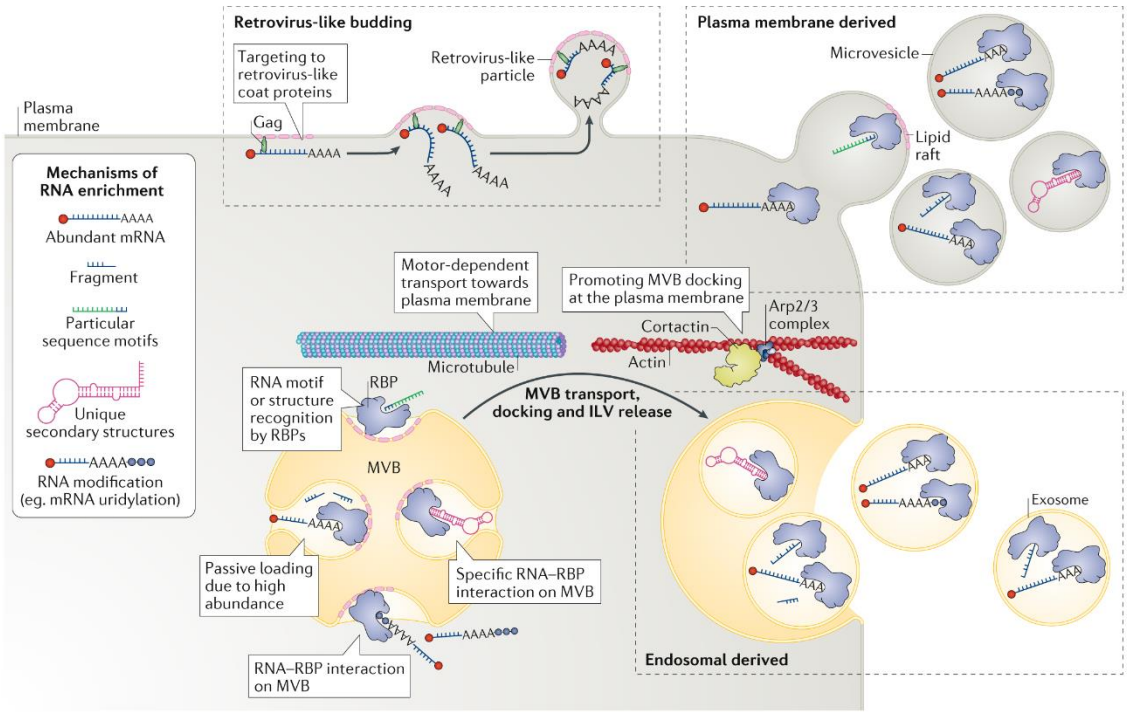

***Figure 1.2 Mechanisms of RNA enrichment in EVs**. The variety of EV-secreted RNA mirrors the heterogenous EV-RNA loading described. Adapted from O'Brien et al. 2020*

et al. 2007). It was also shown via Cre recombinase experiments that mRNAs are translated when delivered upon EV uptake (Kim et al. 2017) (Zomer et al. 2016).

MicroRNAs are small noncoding RNAs of a size range between 19-24 nt. In their mature, single-stranded form they can interact with the RISC complex to exert post-transcriptional gene expression regulation on target mRNAs. In EVs, miRNAs are thought to be one of the most represented small ncRNA species along with tRNA fragments, piRNAs and Y-RNAs (Kim et al. 2017) (Pérez-Boza, Lion, and Struman 2018). This means roughly 30% of the reads in a small RNA NGS library preparation map on secreted miRNAs (Cheng et al. 2014). The main function associated to EV-delivered miRNAs is the gene expression control in receiving cells, however it is possible that miRNA transfer has a role in the immune cell activation upon binding to endosomal Toll-like receptors, as shown in prometastatic tumor microenvironment (Fabbri et al. 2012). Concordantly, recent findings on primary M1 pro-inflammatory macrophages-derived exosomal miRNAome revealed a higher abundance of this RNA species compared to M2 anti-inflammatory counterparts (Pantazi et al. 2022).
About small noncoding RNAs, in this thesis we will refer to a well-represented class of secreted EV-RNA, namely Y-RNAs. This family of sncRNAs (84-112 nt) was first discovered in early 1980s as targeted by autoantibodies derived from patients with systemic lupus erythematosus (Lerner et al. 1981). In humans hY1, hY3, hY4, hY5 Y-RNA have been described, although there is evidence of more than 1000 pseudogenes of these four genes. Y-RNAs form secondary structures rich in CU stretches that are involved in the binding with Ro60 ribonucleoparticles in the cytoplasm. This RNPs participate to non-coding RNA quality control and stress responses and the RNA component serves to stabilize their structure and to allow the subcellular localization (Billmeier et al. 2022). Y-RNAs were detected in EVs deriving from multiple cell types isolated by different purification methods (Driedonks and Nolte-T'Hoen 2019) and the ratio of all of the subtypes has been proposed as a biomarker for immune-related diseases (Driedonks et al. 2020).

For their key role in cell-to-cell communication, EVs have attracted ALS research field since the fact that secreted content is actively taken up by receiving cells. In the context

of the non-cell autonomous hypothesis, EVs could represent vehicles of “pathogenic messages” contributing to disease spreading across different cells and tissues.

1.4.1 EVs in prion-like ALS spreading hypothesis

In the last decade, besides EVs role in physiological intercellular communication, a common hypothesis conceiving EVs as accelerators of the diffusion of toxic ALS-proteins was postulated. EV protein and genetic cargo might rapidly propagate cell death in the CNS contributing to the observed focal neurodegeneration (Gagliardi et al. 2021).
Interestingly, many genes associated to fALS are directly involved in vesicular trafficking as shown in Figure 1.3. Mutations in C9ORF72, VAPB, FIG4, ALS2, CHMP2B, SPG11, SQSTM1, OPTN, UBQLN2, VCP, TBK1 have all been associated to altered endo-lysosomal trafficking, autophagy or EV secretion itself (McCluskey et al. 2022).
ALS proteins forming ubiquitylated inclusions in the cytoplasm (i.e. TDP-43, C9ORF72-derived dipeptide repeats, FUS, SOD1) have been shown to be transferred among cells and act as aggregation seeding foci (McAlary et al. 2019).

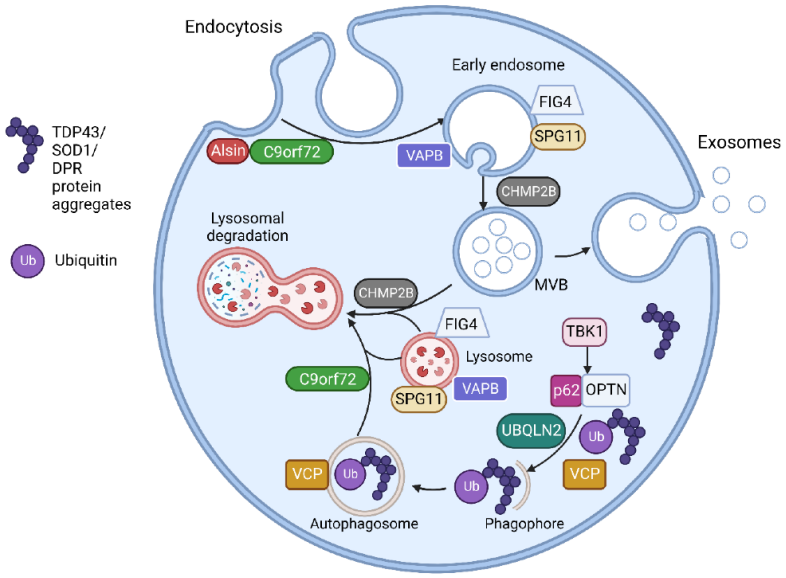

Figure 1.3 EVs proposed role in ALS progression upon protein packaging. *ALS related genes are directly involved in vesicular trafficking and autophagolysosome biogenesis (adapted from McCluskey et al. 2022)*

In other prion-like diseases such as Alzheimer's, Parkinson's or Creutzfeldt-Jakob disease, EVs have already been described as active characters operating the spreading of misfolded proteins such as respectively amyloid β, α-synuclein or the transmissible spongiform-associated prion protein (PrP^{TSE}) (Gabrielli et al. 2022) (Lööv et al. 2016) (Saá et al. 2014). Tau oligomers are known to be carried by exosomes and are involved in several neurodegenerative disease like AD but also FTD (Jackson, Guerrero-Muñoz, and Castillo-Carranza 2022). Similarly, in ALS mutant SOD1, TDP-43 and FUS are described as cargo of neurotoxic EVs, as reviewed by Ferrara and colleagues (Ferrara et al. 2018).

Importantly, misfolded SOD1 was initially found in ALS patients cerebrospinal fluid (CSF) (Zetterström et al. 2011). Later on, Basso et al showed an altered secretory pathways protein expression with consequent exosome release burst in primary SOD1 G93A astrocytes from mice. Astrocytes exosomes were visualized in recipient primary MNs and the exposure to mutant-derived EV resulted in a decreased viability of neurons (Basso et al. 2013). Recently, it was demonstrated that misfolded SOD1 is carried on the surface of SOD1 murine brain-derived extracellular vesicles and confirmed on human SOD1 fALS spinal cord specimens (Silverman et al. 2019).

Similarly, TDP-43 was reported to be transferred horizontally in a cell-to-cell fashion (Feiler et al. 2015). The association of TDP-43 misfolded protein as permanent EV cargo is controversial, although several studies have shown how EVs preparation from TDP-43 models can propagate cellular inclusions in EV-receiving cells (McCluskey et al. 2022). TDP-43 clearance has been shown to be dependent on autophagy and on EV secretion, in fact a pharmacological blockage of exosomes biogenesis resulted in exacerbated TDP-43 intracellular aggregation in mice (Iguchi et al. 2016).

The finding of FUS (along with FUS interacting proteins) and of C9-derived DPRs in EVs completes the picture of EV-encapsulated ALS proteins described in the literature (Ferrara et al. 2018).

As said before, EVs also mediate the transfer of RNAs which can potentially affect the spreading of the disease altering the surrounding gene expression, without involving direct protein material exchange.

Of note, RNA-binding proteins dysfunction occurring in ALS could generate an aberrant RNA cargo sorting in EVs.

In the following paragraph, we will focus on the role of RBPs as determinant EV-RNA sorting factors and providing the rationale of the central hypothesis of the present work.

1.5 Proposing EV-RNA as ALS biomarker source

1.5.1 EV-RNA delivery in ALS affects phenotype of receiving cells

In the paragraph 1.4.1, we described the putative role of EVs in being responsible for the focal spreading of ALS in the CNS, as they could act as carriers of misfolded proteins.

Given EVs role on RNA vehiculation and the abundance of RNA-binding proteins in the context of the disease, EV-RNA content has attracted researchers as a source of neural damage readout for diagnostic purposes. The ability of EVs to protect their cargo from circulating RNases digestion makes them an ideal tool to retrieve a "RNA message" from the donor cells.

In vitro studies with motor neuron-like NSC-34 cells revealed that exosomes secreted from cells transfected with SOD1 G93A are able to affect N9 microglia cell line phenotype through miRNA transfer (Pinto et al. 2017). In detail, miR-124 in G93A exosomes was identified to induce loss of phagocytic ability, senescence, M1 polarization and expression of inflammation markers in N9 cells, already in the first 2 hours after treatment with EVs (Pinto et al. 2017). Furthermore the same target was found in CSF-derived EVs from patients and in EVs from primary SOD1 mouse MNs, in both cases correlating with disease severity (Yelick et al. 2020).

Using a model of iPS-differentiated astrocytes from C9-ALS patients, Varcianna et al identified the downregulation of hsa-miR-494-3p to affect the viability of EV-receiving MN cultures (Varcianna et al. 2019).

Recently, a strong evidence supporting the EV-mediated delivery of toxic RNAs in ALS came from a work of Le Gall and colleagues (Le Gall et al. 2022). Human patients iPSC-derived muscle cells secrete EVs (Muv) that are responsible for phenotypic alteration in

human MNs, eventually causing cell death. MuV proteome features an abundance of RBPs, interacting partners of TDP-43 or FUS and gene ontologies related to RNA metabolism and immune response. Notably, upon EV-treatment healthy MNs show intracellular accumulation of RNA in nuclear foci in a FUS-dependent fashion (Le Gall et al. 2022).

Hence, RNA could play a pivotal role in the progression of ALS when is packaged in secreted vesicles. Specifically, miRNAs are proposed as informative, abundant and powerful RNA species to be employed as biomarkers.

1.5.2 MicroRNA as source of ALS biomarkers: an opportunity for EV-RNA

The identification of circulating miRNA in biofluids has allowed the growth of a number of studies of so-called non-invasive “liquid biopsies”. Especially in cancer diagnosis, miRNA profiles turned out to have diagnostic, prognostic and predictive properties (Jarry et al. 2014). Many studies in the field of amyotrophic lateral sclerosis and frontotemporal dementia are showing signatures of microRNAs that could be informative for both familial and sporadic forms of the disease (Kmetzsch et al. 2022). A meta-analysis on current studies carried on circulating miRNA profiles concluded that C9ORF72 familiarity shares more than half of the dysregulated miRNAs with sporadic cases of ALS-FTD (Kmetzsch et al. 2022). Noteworthy, large scale isolation and RNA-Seq of plasma miRNAs in C9 patients compared to pre-symptomatic individuals in the same genetic predisposition revealed a promising miRNA signature (ROC AUC 0.80) (Kmetzsch et al. 2021). This fact suggested that circulating miRNA could also monitor the onset of the disease. The four differentially expressed miRNAs (miR-34a-5p, miR-345-5p, miR-200c-3p and miR-10a- 3p) in the signature coming out of the study control genes involved in pathways like sphingolipid biosynthesis, neurotrophin and Hippo signaling (Kmetzsch et al. 2021).

Among circulating miRNAs, there are EV-encapsulated miRNAs. Different studies point out at the presence of miRNAs in vesicles from ALS biofluids (Katsu et al. 2019) (Banack, Dunlop, and Cox 2020).

Expression profile was performed on a microarray of plasma EVs from neural origin where Katsu et al described 30 miRNAs dysregulated in ALS vs control: miRNAs in this case resulted in a gene set enrichment analysis concentrated on synaptic pathways. The authors validated on fixed tissues a signature of 4 miRNAs (miR-24-3p, miR-1268a, miR-3911, miR-4646-5) that have common target genes involved in synapsis and exocytosis (Katsu et al. 2019).

Exploiting L1 cell adhesion molecule (L1CAM), a highly expressed EV marker in the neural tissue, Banack et al managed to enrich plasma derived EVs with neural EVs and highlight a neural miRNA signature in ALS patients (Banack, Dunlop, and Cox 2020). This consisted of eight miRNA sequences (miR-146a-5p, miR-199a-3p, miR-199a-5p, miR-4454, miR-10b-5p, miR-29b-3p, miR-151a-3p, miR-151a-5p) differentially expressed in EV-RNA from this sub-population of EVs in ALS/MND compared to healthy donors (Banack, Dunlop, and Cox 2020).

Also, interestingly, long non-coding RNA (lncRNAs), due to their cell-specific expression profiles and their presence in EVs are attracting researchers in the field of biomarker discovery. Regarding ALS, when compared to miRNAs, only few studies have explored the possibility to use circulating lncRNA as predictive transcripts (Laneve et al. 2021). Of notice, 293 lncRNAs were found dysregulated in sALS peripheral blood cells, showing antisense complementarity to coding transcripts, possibly underlying a sequence-directed mechanism of action (Gagliardi et al. 2018).

Altogether, this data encourages efforts in utilizing EV-RNA as predictive biomarker in the context of ALS.

1.6 RNA binding proteins as EV-RNA sorting factors

EV-RNA is the result of a coordinated packaging process by which cells tune the type and dosage of specific RNA subtypes that must be protected and secreted in the extracellular milieu. The efficiency of secretion of different RNA species varies significantly and we discussed their relative abundance in the paragraph 1.3. Relative intracellular concentration affects the passive RNA cargo sorting in EVs, as it is true for many other biological transport mechanisms. It cannot be excluded that the recognition of RNA folding motifs or differential affinity for lipid domains result in a semi-active selection of the RNA cargo (O'Brien et al. 2020). In contrast, proteins are widely recognized as trans-acting factors actively regulating the packaging of vesicular RNA in a stimulus-specific way (Fabbiano et al. 2020). Up to >1500 candidates RBPs are defined in the human proteome since they meet one of these criteria: 1) they possess RNA-binding or RNA-enzymatic domains, 2) they are shown in precipitation or functional experiments to be part of RNP complexes or 3) they are evolutionary related to other protein-encoding genes involved in post-transcriptional regulation (Gerstberger et al. 2014). Indeed, RBPs often cooperate in RNPs to shuttle RNAs across the cell body (Gerstberger, Hafner, and Tuschl 2014). Recently, we reviewed the proteins associated to the mechanism of EV-RNA sorting: the hnRNP family members (hnRNPA2B1, hnRNPC1, hnRNPG, hnRNPH1, hnRNPK, and hnRNPQ/SYNCRIP) emerged among YBX1, HuR, AGO2, IGF2BP1, MEX3C, ANXA2, ALIX, NCL, FUS, MVP, LIN28, SRP9/14, QKI, and TERT RNA-binding proteins (Fabbiano et al. 2020). Target RNAs bound by these RBPs as well as the proteins themselves are secreted in EVs. There is also evidence that specific consensus sequences recognized by RBPs determine the vesicular RNA packaging (Ahadi et al. 2016).

Extracellular RNA (exRNA) can be packed in EVs upon the presence of RNA motifs (identified in vitro or in silico) e.g. the EXOmotifs or due to particular sequences assigning transcripts to cell retention (Garcia-Martin et al. 2022). Many studies validated with functional experiments some RBP-specific EV-RNA consensuses like the A/G-rich sequences by hnRNPA2B1, hnRNPH1, hnRNPQ, AGO2, and ANXA2, AU-rich stretches by HuR or hnRNPC1; C-rich transcripts by hnRNPG, hnRNPK, YBX1, and NCL

(Fabbiano et al. 2020). This means that a possible depletion or dosage alteration in the cell of these RBPs could generate a dramatic change in the species secreted in EVs. It is especially the case of hnRNP family RBPs that are known to form ribonucleoparticles and greatly interact among each other. They are also involved in stress granules formation that would sequester them from the EV-RNA sorting machinery.

Besides *cis*-acting sequences directly bound to proteins, also RNA secondary structures and PTMs occurring at the level of the RBP (e.g. phosphorylation, SUMOylation, ubiquitylation, and uridylation) have been demonstrated to regulate the encapsulation of transcripts (O'Brien et al. 2020).

It cannot be ruled out that some of these RBPs might need to interact with proteins involved in the EVs biogenesis. Interestingly, for example hnRNPs, YBX1 and MEX3C present STRING-reviewed protein-protein interactions with members of complexes involved in EVs formation (Fabbiano et al. 2020).

In this work, we study an RNA-binding protein that was never associated with EV cargo loading until now. Interestingly, this RBP, DDX58 was also recently linked to ALS.

1.7 DDX58 in ALS: a novel RBP involved in the disease?

In the presented work, an interest for this protein in the ALS context arises from recent publications proposing DEAD/H box RNA Helicase 58 (DDX58) as an RBP upregulated in the disease and functionally linked to ALS pathophysiology.

Also known as, retinoic acid inducible gene I (RIG-I), DDX58 is a member of RIG-I-like receptors (RLRs) involved in innate immunity against RNA viruses. We will review the known functionalities of this protein later in dedicated paragraphs, to highlight the versatility of DDX proteins and of recently described non-canonical DDX58 functions.

Interestingly, DDX58 was associated with ALS in both TDP-43 and SOD1 models.

In a translational profiling study, MacNair et al identified DDX58 mRNA in the translatome of TDP-43^{A315T} mouse primary motor neurons (Macnair et al. 2016). Using a translating ribosome affinity purification (TRAP)—microarray approach, the authors

isolated genes exhibiting a >2-fold expression in symptomatic mice compared to non-transgenic littermates. DDX58 was observed as upregulated in the mutant mice and its abundance was validated in immunostaining of the cytoplasm of spinal cord mouse motor neurons and in tissue sections of human sALS and fALS, both in neural and glial cells. Interestingly, *Ddx58* mRNA was described in vitro to be a functional target of TDP-43, suggesting that dysfunctions in the RNA metabolism in ALS could enhance the translation of DDX58 protein (Macnair et al. 2016).

DDX58 upregulation had already been noted in pre-symptomatic SOD1 G93A mice (Kudo et al. 2010). In a whole transcriptome analysis of SOD1 and TAU models' spinal cord, Ddx58 overexpression was confirmed by semi-quantitative RT-PCR and immunohistochemistry. Of note, a huge downregulation of the protein amount was retrieved from post-mortem sALS tissue microarrays (Kudo et al. 2010).

In a recent study carried out on neuroblastoma SH-SY5Y cells, researchers showed how TDP-43 depletion is responsible for accumulation of endogenous RNAPIII-transcribed ncRNAs accumulation in the cytosol with consequent activation of DDX58-mediated interferon response (Dunker et al. 2021). The authors speculated that loss of TDP-43 unshields *Alu*, 7SL or 7SK retroelements transcripts that are bound by RIG-I. The system is reverted from exogenous expression of full length TDP-43, but not when its RNA recognition motif is mutated, supporting the fact that TDP-43 RNA binding is necessary to mask ncRNA recognition by DDX58 (Dunker et al. 2021).

In spinocerebellar ataxia type 2 (SCA2) mice, recapitulating many of the phenotypes in common with ALS, DDX58 gene was found overexpressed in the spinal cord along with several other genes associated to human ALS (Scoles et al. 2020).

DDX58 was functionally correlated to other fALS genes like TBK1, OPTN, p62 (Xian et al. 2020), VCP (Hao et al. 2015) or CYLD (Friedman et al. 2008).

Interestingly, in a very recent whole genome sequencing study carried out on more than 6000 ALS-genomes a rare variant in the 3'UTR region of interleukin-18 receptor accessory protein (IL18RAP) was identified causative of sALS (Eitan et al. 2022). The mutation renders the post-transcriptional control of the gene by RBPs altered in comparison with the wt variant, that results to be neuroprotective in human iPSC-derived cultures. Among the RBPs differentially enriched, DDX58 was found to bind the

mutant 3'UTR of IL18RAP with a lower efficiency probably due to changes in the secondary structure of the transcript (Eitan et al. 2022).

1.7.1 DExD-Box (DDX) proteins as versatile RNA helicases

ATP-dependent RNA helicases are an interesting group of RNA-binding proteins initially described as RNA-substrate enzymes involved in the unwinding of RNA secondary structures. In recent years, their RNA-related multifaceted activity is expanding beyond this function.

Eukaryotic RNA helicases are distinct in two major superfamilies (SF1 and SF2). In the human genome, SF1 (or Upf1-like) proteins are in net minority. Conversely, in SF2 superfamily is divided in the DEAD box (DDX) family, DEAH box (DHX) family, and the

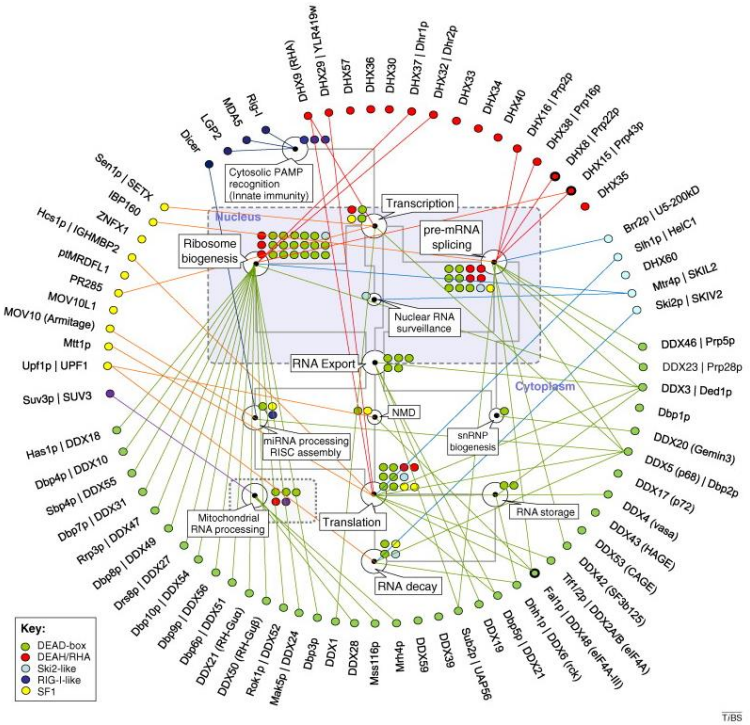

***Figure 1.4 Roles of eukaryotic RNA helicases**. RNA helicases are involved in different cellular functions. Of notice, DDX helicases representativity is high as well as the interconnection of the protein family members. Adapted from Jankowsky 2011*

Ski2-like family. Additionally, 5 members belong to the RIG-I-like family, evolutionary linked to DDX proteins (Bourgeois, Mortreux, and Auboeuf 2016) (Jankowsky 2011).

SF2 superfamily RNA helicase contain two RecA domains that take contact with RNAs and hydrolyze ATP to activate the enzymatic RNA conformation unwinding reaction as a sort of flexible clamp working in a sequence-independent way (Ozgur et al. 2015). Both superfamilies contain a minimum of 12 conserved primary sequence motifs: motif Q, I, IIa, IIb, III, IIIa in the RecA1 domain; motif IV, IVa, V, Va, Vb, VI in RecA2 domain (Jankowsky 2011). DEAD/H box helicase families are characterized by the conserved Asp-Glu-Ala-Asp/His motif in the core domains, regulating substrate binding. C- and N-terminal domains generally flank the helicase core and are often responsible for additional activities of the proteins.

DDX proteins are able to translocate along short dsRNA strands (as short as 10 nt in length) and partially destabilize local structures, giving DDX helicases very low RNA processivity (Bourgeois, Mortreux, and Auboeuf 2016). Also, DDX RNA helicase are able to anneal to RNA. This could explain the several processes in which they are involved besides RNA chaperoning (Bourgeois, Mortreux, and Auboeuf 2016). Some examples are: remodeling of RNP complexes, ribosome biogenesis, spliceosome assembly, circRNA biogenesis. mRNA translation, RNA export (Jarmoskaite and Russell 2014)(Leitão, Costa, and Enguita 2015). Interestingly, DDX helicases interact with other members of the non-coding transcriptome such as lncRNAs, lincRNAs, miRNAs (Leitão, Costa, and Enguita 2015).

1.7.2 Focus on DDX58: canonical role in viral RNA sensing

Also known as retinoic acid inducible gene I (RIG-I), DDX58 is a member of the RLRs along with melanoma differentiation-associated protein 5 (MDA5) and laboratory of genetics and physiology 2 (LGP2). Both RIG-I and MDA5 are able to interact with mitochondria antiviral sensor (MAVS) proteins by means of their N-terminal CARD2 domains, two tandem caspase activation and recruitment domains (G. Q. Liu and Gack 2020).

Conversely, LGP2 mainly acts as a signaling regulator, due to the lack of N-terminal immune signal competent domains. In particular, RNA binding occurs upon the structural interaction with the zinc binding C-terminal domain tail (CTD) and the release of the autoinhibitory motif Hel2i of the helicase domain from the CARD domains that become free to bind the MAVS (Chow, Gale, and Loo 2018)(Dickey, Song, and Pyle 2019). The adaptor MAVS proteins oligomerize in a prion-like manner and recruit TRAF2, TRAF3 and TRAF6 to the "signalosome" which ensures the phosphorylation cascade that promotes the nuclear translocation of IRF3/IRF7 and NF-κB. This results in the transcription of interferon type I and type III and interferon stimulated genes to combat the viral infection (Chow, Gale, and Loo 2018).

Post-translational modifications (PTMs) tightly regulate the activation status of DDX58 as well as MDA5, a process of paramount importance that is deficient in autoimmune diseases such as interferonopathies. RIG-I interacts with E3 ubiquitin ligases like Riplet or TRIM25 that catalyze the K63 polyubiquitylation both in the CARD and in the CTD domains (G. Q. Liu and Gack 2020). Also, dephosphorylation by PP1α/γ phosphatase and HDAC6-dependent deacetylation are required to stabilize RIG-I into the open conformation after agonist RNA binding (Chow, Gale, and Loo 2018).

DDX58 preferentially recognize short (10-19 bp) blunt-ended dsRNA stretches in the form of 5' di- or tri-phosphorylated viral replication intermediate (Liu and Gack 2020). Besides these two requirements, recently several motifs in the RNA agonists have been proposed to facilitate the detection of foreign RNAs. This is the case of negative-strand RNA viruses carrying panhandle structures (G. Liu et al. 2015), UC-rich sequences in hepatitis C virus (Schnell et al. 2012), poly(AU) from measles viral mRNA (Runge et al. 2014) but also deriving from RNA pol III transcripts in DNA viruses (Ablasser et al. 2009).

Interestingly, a process, which was thought to be sequence independent, is increasingly attracting the attention of the community as DDX58 has shown a certain degree of self-RNA recognition and involvement in a series of non-canonical functions. The latter will be the topic of the following paragraph.

1.7.3 Non-canonical functions of DDX58

Since DDX58 shows a certain plasticity in the recognition of the RNA ligand, an increasing literature is providing evidence for unconventional RNA-binding properties which confer non-canonical functions to the RNA sensor. Such promiscuity might determine diverse RIG-I antiviral responses, but also novel functions to be associated to DDX58.

DDX58 was shown to recognize both viral and host cell derived fragments of RNA generated by RNase L (Malathi et al. 2007). Specifically, exogenous (or derived from antiviral OAS protein) 2'-5' poly(A) activates RNase L that digests host RNA in small fragments activating the IFN response mediated by RIG-I (Malathi et al. 2007). Endogenous host retroelements were also shown to boost antiviral response upon DDX58 binding, in particular endogenous retroviruses (ERVs) and RNA polymerase III-transcribed short interspersed elements (SINEs) (Xu et al. 2018).

Regarding repetitive elements, recent clues reported that stromal cells in the context of breast cancer release exosomes carrying transposable non-coding RNAs that activate the IFN response through RIG-I recognition, thus facilitating chemoresistance and tumor growth (Nabet et al. 2017) (Boelens et al. 2014). DDX58 can also bind snRNA, aberrantly present in the cytoplasm upon ionizing radiation in HCT116 cells (Xu et al. 2018) and RNase digestion generated rRNA fragments. Ribosomal RNA from a 5S pseudogene was also shown to potentiate the immunogenicity of viruses exploiting host endogenous transcripts (Chiang et al. 2018). In addition, DDX58 was shown to bind viral but also host circular RNAs at the intron junction where the discrimination of the self is aided by the presence of host RBPs binding sites (Y. G. Chen et al. 2017).

Strikingly, DDX58 was demonstrated to bind microRNAs (L. Zhao et al. 2015) (Karlsen and Brinchmann 2013). In detail, miR-136 precipitates with RIG-I in RNA immunoprecipitation experiments on infected lung cancer cell line (Zhao et al. 2015) and exogenous miR-145 interacts with RIG-I upon electroporation to activate the IFN response (Karlsen and Brinchmann 2013).

A post-transcriptional control effect of DDX58 was initially identified in the context of granulocytes differentiation where levels of the protein are correlated to reduced IFN consensus sequence binding protein (ICSBP), a transcription repressor of myeloid development. Such a role that was confirmed also in leukemia proliferation (Xu et al. 2018). There is evidence that DDX58 could bind to multiple mRNA transcripts in the cell and in particular the recognition of the 3'UTR of NFκB/p105 encoding RNA appears fundamental for the translation of the protein (Zhang et al. 2013).

Taken together, these studies point out that newly discovered RNA binding functions could be associated to an expanded palette of DDX58 functions. This renders RNA helicase DDX58 an ideal protein to be investigated beyond innate immunity.

2. AIM OF THE THESIS

The aim of the research was to investigate a possible role of DDX58 as a novel RBP, emerging in ALS, in EV biology. To address this aim, we studied 1) the subcellular distribution of a DDX58-GFP recombinant protein along with protein hallmarks of ALS, such as SOD1 and TDP-43; 2) the connection of DDX58 with EV secretion and content, 3) the miRNA-based potential links between DDX58 and SOD1 in vesicular RNA.

1. For the first aim, we used a recombinant tGFP-tagged DDX58. We exploited confocal microscopy and an optimized subcellular fractionation procedure to describe the intracellular distribution of the protein. We used high-content imaging and immunoprecipitation approaches to evaluate a possible association of DDX58 to SOD1 and TDP-43.

2. To address the second aim, we used state of art orthogonal EV isolation techniques (NBI, dUC, OptiPrep™ density gradient) and characterized the vesicular profile (NTA) and EV content (Western blotting and EV-RNA profiling).

3. Finally, we performed Next Generation Sequencing on NSC34 cells (FACS-Seq) and primary SOD1 astrocytes. We analysed the EV-associated miRNA content using ddPCR assays on representative targets, using HEK293T cells and iPS-derived motor neurons progenitors. We explored EV-RNA pull down approaches to understand the connection between DDX58, SOD1 (and TDP-43) in EV-RNA trafficking. We assessed the possible functional connection of DDX58-associated RNAs via NF-κB activation experiments, senescence phenotype analysis, and cell viability assay.

3. RESULTS

The RNA helicase DDX58 is increasingly emerging in the ALS field as a novel RBP involved in disease. A translational activation of the protein was found in TDP-43^{A315T} mouse motor neurons (Macnair et al. 2016). DDX58 overexpression has been associated to pre-symptomatic SOD1 G93A mouse model (Kudo et al. 2010). Recently, the recognition of endogenous pro-inflammatory RNAs by DDX58 was described in TDP-43 depleted cells (Dunker et al. 2021). Also, it emerged among the RBPs able to bind the 3'UTR of interleukin-18 receptor accessory protein (IL18RAP), a newly discovered sALS gene variant (Eitan et al. 2022).

These indications, together with the role of RBPs in EV-RNA sorting (Fabbiano et al. 2020), provided the rationale to elucidate the potential role of DDX58 in the regulation of vesicular RNA in ALS models.

To do so, we had the possibility to use mouse motor neuron-like cell line NSC34 together with SOD1 G93A mouse primary astrocytes provided by our collaborators at the University of Genova. Additionally, we had the chance to cross-validate our hypothesis on iPS-differentiated motor neuron progenitors and mature human motor neurons, obtained from the research period spent abroad in IRBLleida (Lleida, Spain).

3.1 The subcellular localization of recombinant DDX58-tGFP partially mirrors the endogenous protein

Using NSC34, we transiently overexpressed a human recombinant DDX58 protein fused to TurboGFP (tGFP) at the C-terminus. As shown in Figure 3.1A, the recombinant protein was detectable by western blotting at the expected molecular weight. After 48 hours of transfection about 54.5% of the cells resulted transfected by flow-cytometry (Figure 3.1B). Since DDX58 is known to interact with the outer mitochondria membrane upon antiviral signal activation and to be negatively regulated by lysosome-dependent degradation (Rehwinkel and Gack 2020), we checked its intracellular localization with mitochondria and lysosome staining dyes. As expected, DDX58-tGFP intracellular

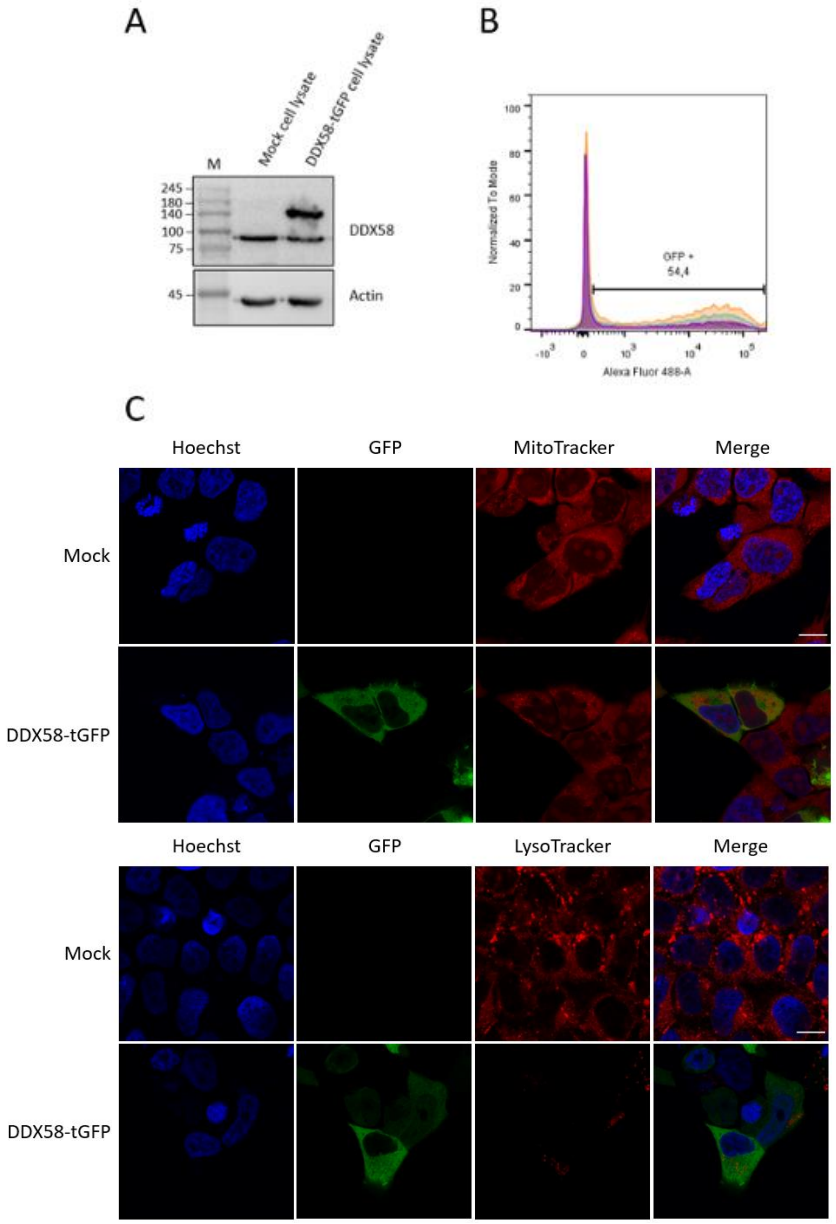

Figure 3.1 DDX58-tGFP overexpression and intracellular localization in NSC34. *A) Western blot showing recombinant DDX58 overexpression in NSC34 cells; M=molecular weight marker. B) Histogram from FACS analysis on cells expressing DDX58-tGFP showing the percentage of gated live cells, positive to GFP compared to mock; the result reports the average of seven technical replicates. C) Representative confocal images of DDX58-tGFP in green, and MitoTracker (upper panel)/LysoTracker (lower panel) in red, nuclei in blue; 63X magnification, Scale bar: 10 µm*

distribution was mainly cytosolic with no apparent co-localization with mitochondria or lysosomes (Figure 3.1C) . A similar distribution was observed staining the endogenous murine Ddx58 using two different commercially available antibodies (Figure 3.2A). Interestingly, one of the two antibodies generated a punctuated distribution of the signal, still not localizing with the LysoTracker™ dye (Figure 3.2B). Given this distribution and since DDX proteins are recognized master regulators of membraneless organelles

formation (Hondele et al. 2019), we decided to explore the localization of Ddx58 with a P-bodies marker, Dcp1A, and a stress granule marker, Tia1. We observed that the overexpression conditions we used did not induce spontaneous stress granules assembly and the punctuated distribution of Ddx58 did not merge the Dcp1A signal (Figure 3.3).

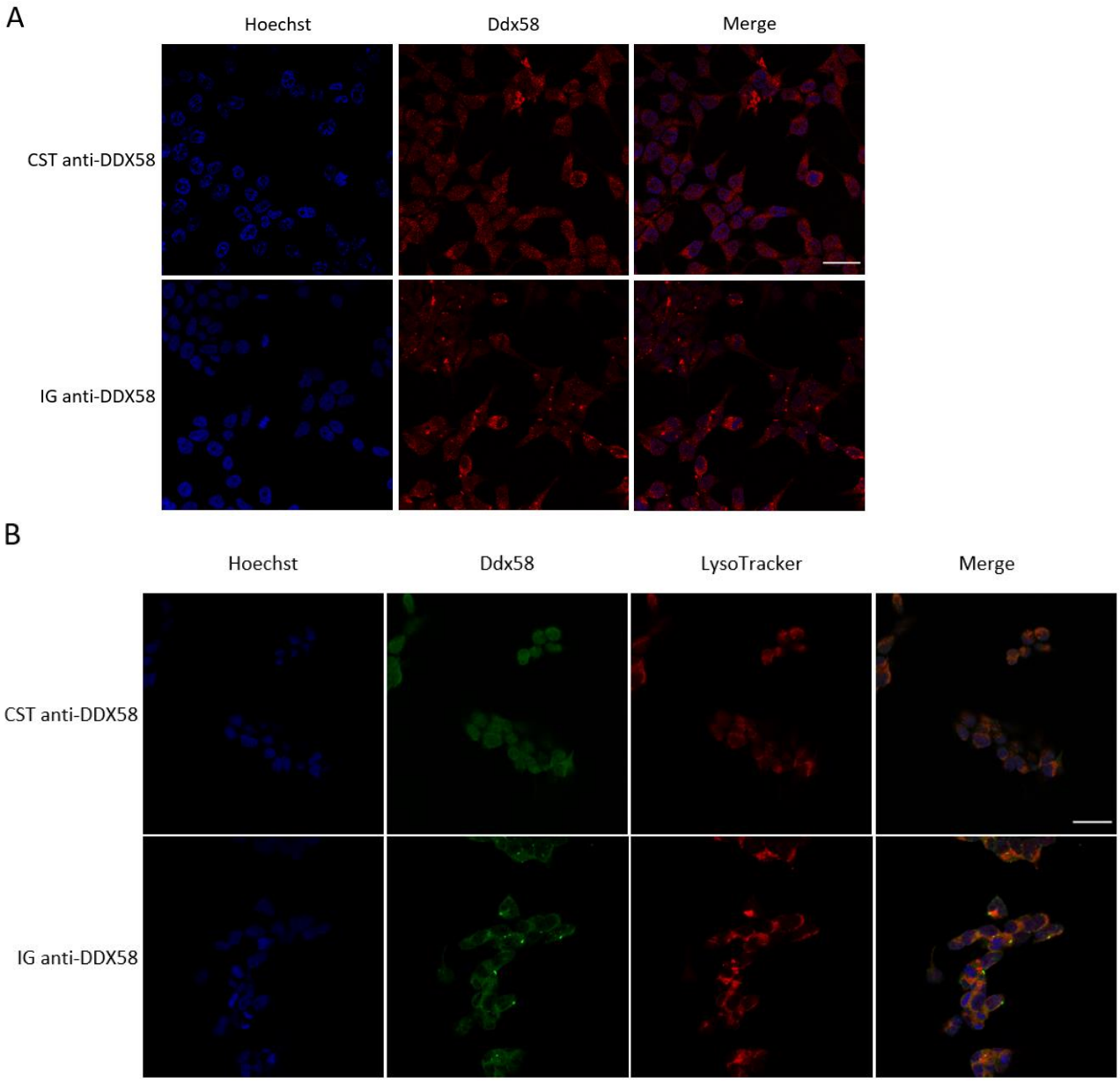

Figure 3.2 Different commercial antibodies stain the endogenous Ddx58 protein. *A) Representative confocal images of non-transfected NSC34 cells. IG anti-DDX58 antibody shows a punctuated signal. Ddx58 in red, nuclei in blue. B) Representative confocal images of non-transfected cells stained with LysoTracker dye. Ddx58 in green, LysoTracker in red, nuclei in blue. CST = Cell Signaling Technology IG = Invitrogen; 63X magnification, Scale bar: 30 µm*

We concluded that the recombinant DDX58 protein shows a similar intracellular distribution as the endogenous Ddx58.

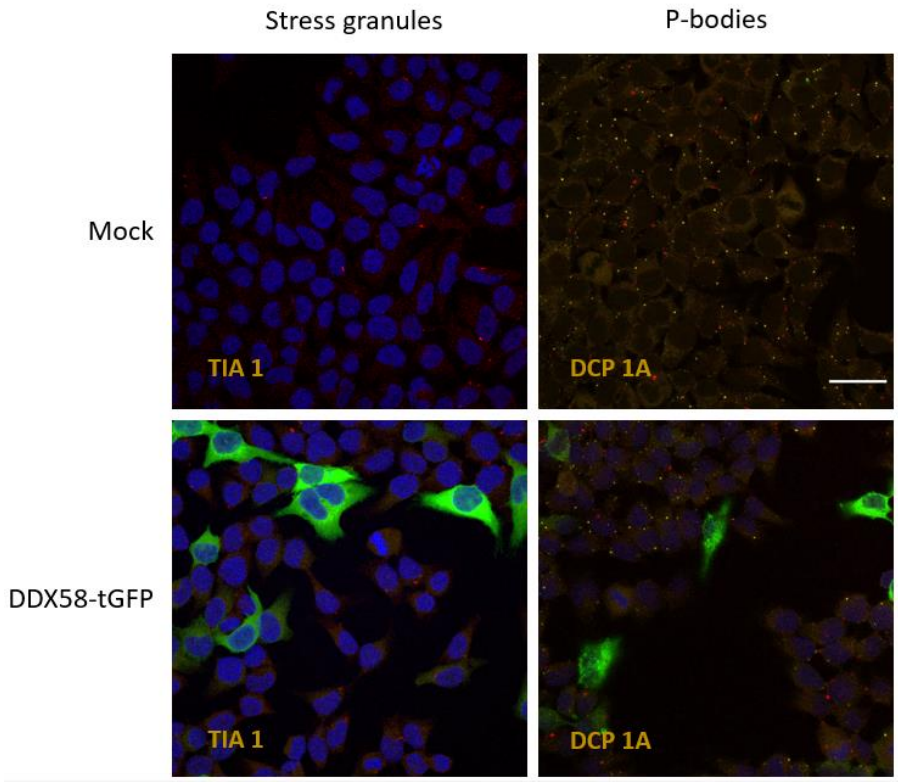

Figure 3.3 Endogenous and recombinant DDX58 do not associate with stress granules and P-bodies. *Representative merged confocal images of mock and DDX58-tGFP-transfected NSC34 stained in red with Invitrogen anti-DDX58 and with the antibody marked in yellow on bottom left. GFP in green, nuclei in blue. 63X magnification, Scale bar: 30 µm*

Using a cell fractionation procedure previously optimized on HEK293T cells lysates (modified from Baghirova et al. 2015), we observed that the endogenous DDX58 protein is predominantly co-sedimenting with organelle particles. In fact, an average of 77% of total DDX58 input protein was recovered. Out of it, a 62% co-sedimented in the organelle fraction (Figure 3.4A) along with ER markers such as VAP-B. The remaining 12% was isolated in the nuclear proteins fraction and 3% associated to soluble cytosolic fraction. Interestingly, we detected a small portion of the protein in the nuclear fraction, confirming the presence of nuclear-resident DDX58, already described (G. Liu et al. 2018). Interestingly a shift in molecular weight was observed for the nuclear counterpart, possibly implying a mechanism of post translational modification. In the case of lysates derived from DDX58-tGFP overexpressing cells, 66% of the endogenous DDX58 protein was recovered over the input. Out of it, we recovered 49% in the organelles, 8% in the cytosol, 7% in the nucleus, demonstrating that the tGFP did not significantly alter the distribution of the endogenous protein in the cell. Regarding the

tGFP-tagged DDX58, 58% of the input was recovered downstream the fractionation, out of which more than a half was detected in the cytosolic fraction, in accordance with the confocal microscopy. Interestingly, we show a very preliminary indication that upon extension of the expression time to additional 48 hours the 85% of the endogenous protein is retrieved in the organelles (Figure 3.4B) whilst the detected ectopic DDX58 passes from a 62% cytosolic 34% organelles to a 52% cytosolic 38% organelle-bound.

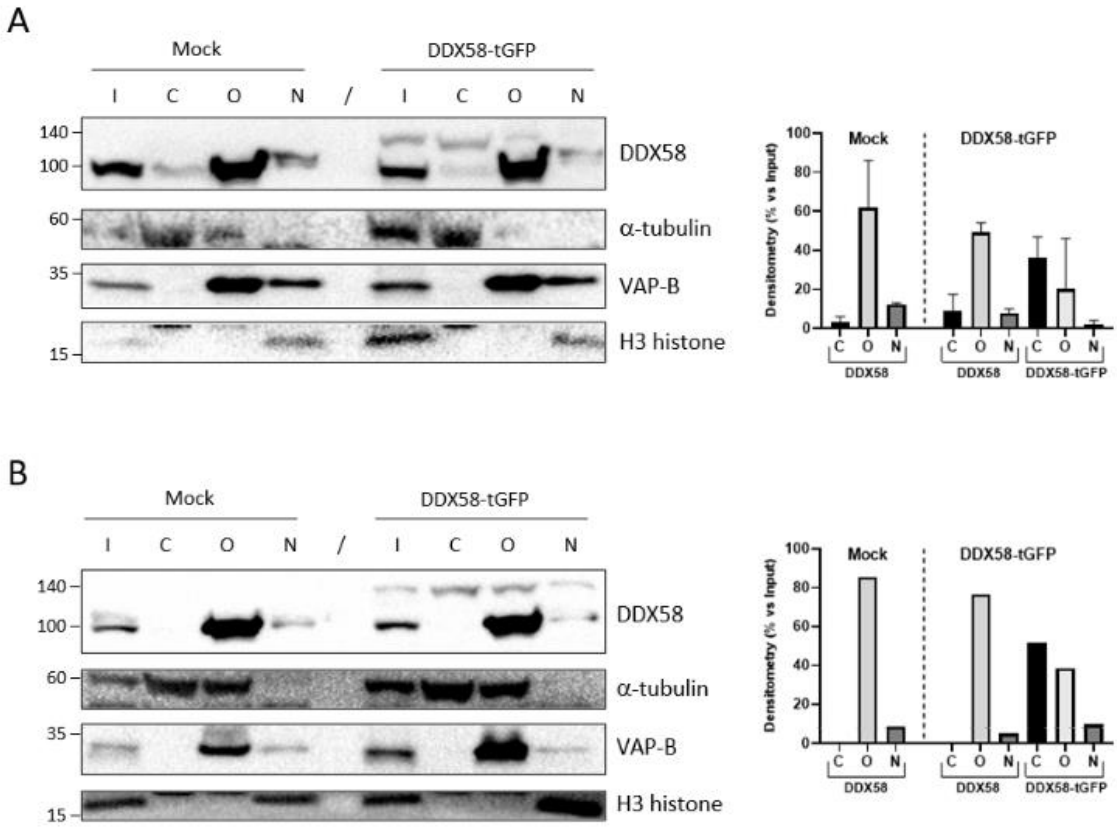

Figure 3.4 DDX58-tGFP subcellular distribution 48 h and 96 h after transfection *: A) Representative WB showing DDX58 subcellular distribution 48 h after transfection. Densitometry represents the quantification of the protein in the fractions calculated over the recovered input. Standard deviations are relative to two independent biological replicates. mean ± SD. B) WB showing DDX58 subcellular distribution 96 h after transfection. Densitometry representing the quantification of the protein in the fractions calculated over the recovered input. I = 1% input; C = cytosol, O = organelles, N = nucleus*

This gave us an indication of the specific subcellular localization of recombinant and endogenous DDX58 protein. We concluded that, albeit its abundance in the cytosol, the recombinant DDX58 mirrors the distribution of the endogenous protein.

3.2 DDX58 and SOD1 can interact at the intracellular level

Since we showed the cytosol and organelle-associated distribution of Ddx58 and given the reported cytosolic and mitochondria distribution of SOD1 (Rotunno and Bosco 2013), we explored the intracellular distribution of transfected SOD1 along with the endogenous Ddx58.

We transfected NSC34 with a plasmid encoding for either the human wt or G93A mutant SOD1 harboring a hemagglutinin (HA) tag at the N-terminus, kindly provided us from the Laboratory of Transcriptional Neurobiology led by Prof. Manuela Basso (CIBIO, Trento). After 48 h of transfection, we looked at the intracellular distribution of endogenous Ddx58 and HA-SOD1 protein through confocal microscopy. Qualitatively, we revealed a partial cytosolic overlap of the signals in both HA-SOD1 wt and G93A transfected cells, with no apparent difference in the Ddx58 subcellular distribution (Figure 3.5A).

We also analyzed the distribution between HA-SOD1 and DDX58-tGFP in co-transfected cells, exploiting a high-content imaging approach. In representative pictures (Figure 3.5B), we appreciated an expected increased SOD1 signal upon overexpression and an overlapped SOD1 and DDX58-tGFP signal in co-expressing cells. Downstream, we did not see any significant difference in SOD1 immunostaining in the cytosol nor in the nucleus. The double positive cells in the co-transfected condition showed a significantly lower cytosolic DDX58-tGFP signal in presence of HA-SOD1 G93A mutant rather than wt (Figure 3.5B). This difference could be due to the propensity of SOD1 G93A protein to form insoluble aggregates (Gomes, Escrevente, and Costa 2010) and the diminished detection by the anti-SOD1 primary antibody.

Taken together, these results point out at a possible local association of DDX58 and SOD1 at the intracellular level. Interestingly, the subcellular localization investigated with the hallmark ALS-protein, TDP-43 did not result in appreciable overlap with DDX58 intracellular distribution. This part will be discussed in paragraph 3.8.

A

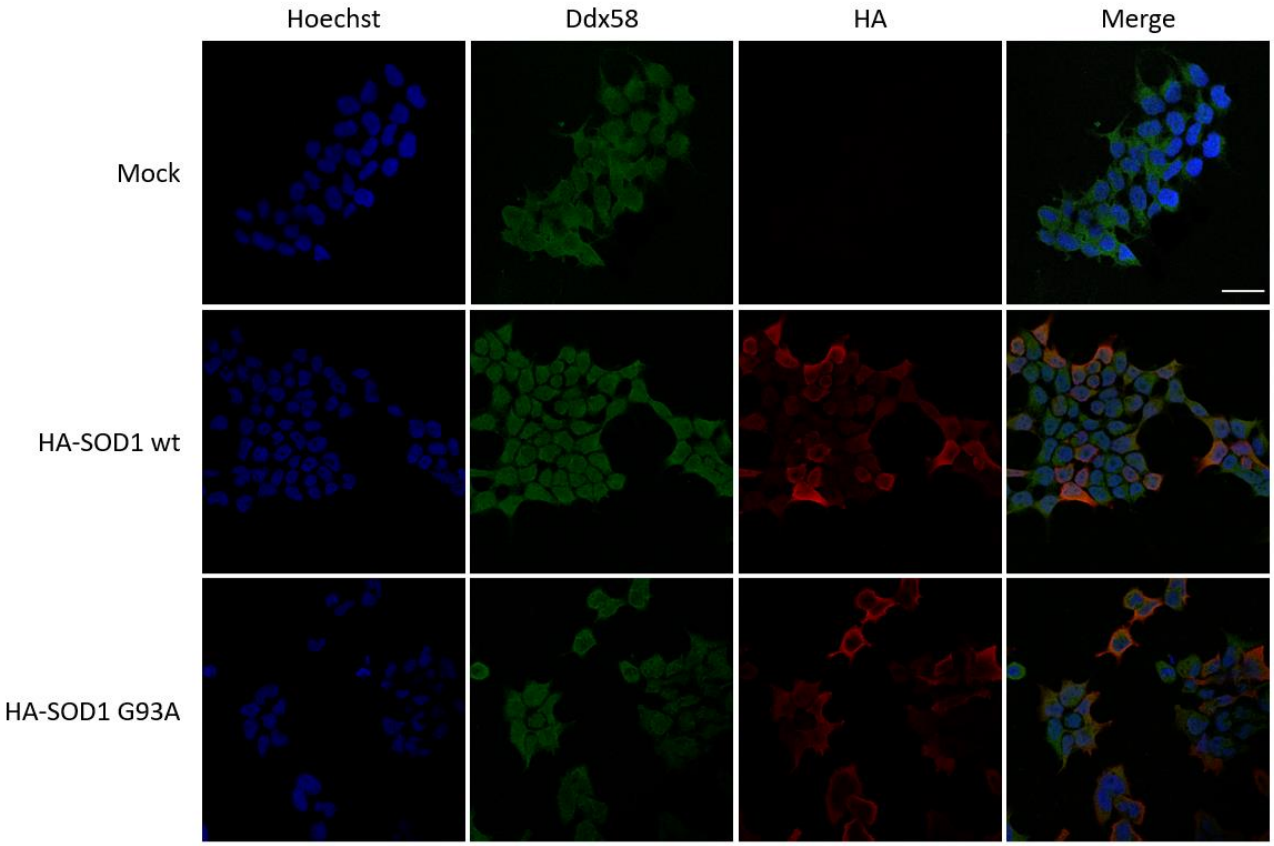
Hoechst
Ddx58
HA
Merge
Mock
HA-SOD1 wt
HA-SOD1 G93A

B

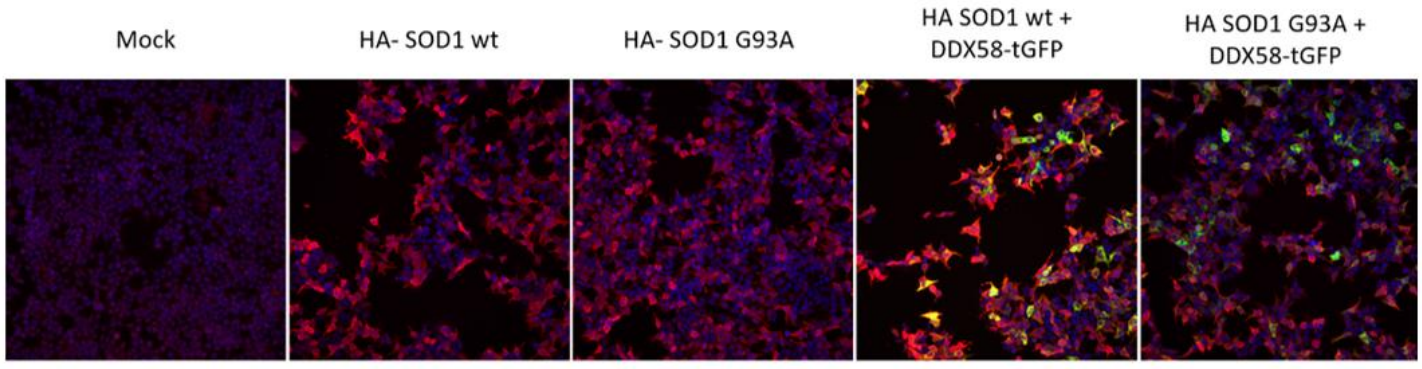
Mock
HA- SOD1 wt
HA- SOD1 G93A
HA SOD1 wt + DDX58-tGFP
HA SOD1 G93A + DDX58-tGFP
Hoechst
SOD1
DDX58-tGFP

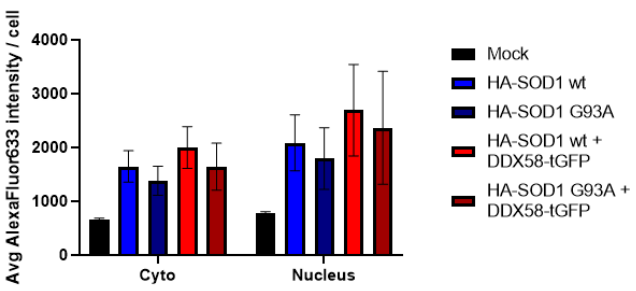
Avg AlexaFluor633 intensity / cell
4000
3000
2000
1000
0
Cyto
Nucleus
Mock
HA-SOD1 wt
HA-SOD1 G93A
HA-SOD1 wt + DDX58-tGFP
HA-SOD1 G93A + DDX58-tGFP

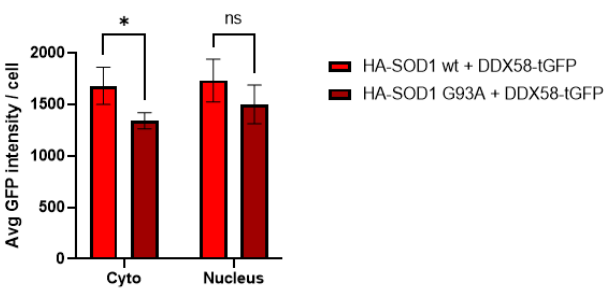
*
ns
Avg GFP intensity / cell
2000
1500
1000
500
0
Cyto
Nucleus
HA-SOD1 wt + DDX58-tGFP
HA-SOD1 G93A + DDX58-tGFP

Figure 3.5 Intracellular distribution of endogenous and recombinant DDX58 in SOD1-overexpressing NSC34. *A) Representative confocal images of NSC34 overexpressing HA-SOD1 wt and HA-SOD1 G93A, stained in red and Ddx58 stained in green; nuclei in blue. 63X magnification, Scale bar: 30 µm. B) Representative merged channels images of high-content confocal analysis and corresponding quantification. Legend below the images. 20X magnification. Bottom left: quantification of the red channel intensity normalized for the cell count. The graph plots Mean ± SD representative of five technical replicates. Bottom right: quantification of the green channel intensity normalized for the cell count. The graph plots Mean ± SD representative of five technical replicates. ANOVA *P-value <0.05; ns non-significant*

We corroborated the result by investigating DDX58-SOD1 biochemical interaction *in vitro* through anti-DDX58 and anti-SOD1 immunoprecipitation. As shown in Figure 3.6A, the antibody against SOD1 is able to co-precipitate a considerable amount of Ddx58 over the IgG in Mock cells. In the anti-SOD1 IP, we observed a shift in the electrophoretic mobility, possibly implying the recognition of a specific isoform of Ddx58. In a second experiment though, doubling input lysate volumes, in IP samples we were able to detect more clearly Ddx58 from DDX58-tGFP overexpressing cells and HA-SOD1 overexpressing cells with both antibodies. Ddx58 immunoprecipitation resulted to be efficient in DDX58-overexpressing cells with both antibodies. Interestingly, in SOD1-overexpressing cells, Ddx58 immunoprecipitation resulted 4 times higher using anti-SOD1 antibody compared to anti-DDX58 antibody (Figure 3.6B). Conversely, the anti-DDX58 antibody

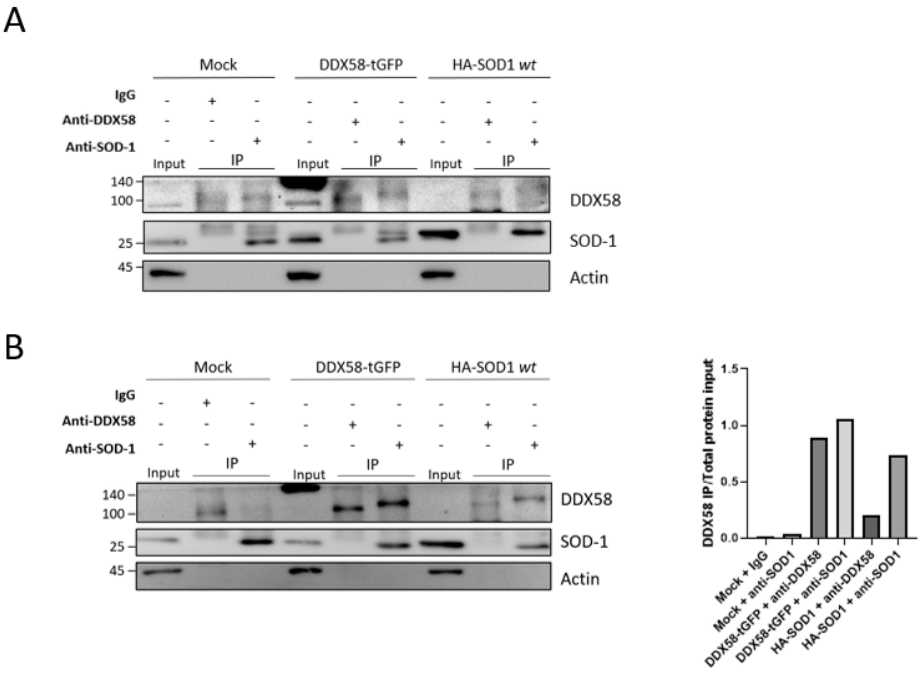

Figure 3.6 Ddx58 immunoprecipitation upon recombinant DDX58 and SOD1 overexpression in NSC34. *A) Western blot of the first trial IP experiment using anti-DDX58 and anti-SOD1 antibodies as baits. Anti-DDX58, anti-SOD1 and anti-actin blots are reported. Input is 1/10 of lysate volume. Type of lysate is reported on top of the figure. B) Western blot of the second trial IP experiment using double volume of lysates and anti-DDX58 and anti-SOD1 antibodies as baits. Anti-DDX58, anti-SOD1 and anti-actin blots are reported. Input is 1/10 of lysate volume. Type of lysate is reported on top of the figure. Densitometric analysis represented on bottom right: IP quantified over total protein loaded (actin densitometry), n=1.*

was not able to co-precipitate Sod1 nor the exogenous HA-SOD1 wt. We tried to clarify the absence of Sod1 in anti-DDX58 IP exploiting the use of a different commercially available antibody and an anti-tGFP antibody without successful results (data not known).

To understand whether G93A mutation could affect the IP of Ddx58, we performed a pilot experiment on HA-SOD1 G93A overexpressing cells.

From the anti-HA blot, we saw a reduced signal in the anti-SOD1 IP in the presence of the mutation, possibly in line with the increased proneness of G93A mutant to form insoluble aggregates. Using anti-DDX58 antibody, we observed a decreased Ddx58 immunoprecipitation in HA-SOD1 G93A lysates, while an enrichment was visible using anti-SOD1 antibody (Figure 3.7). This could be informative of a possible reduction of Ddx58 availability in the soluble fraction to be accessed by anti-DDX58 antibody. Even though we did not investigate further the aggregation properties of the two proteins in our experimental settings, the result was in line with the reduced cytosolic signal that we observed for the recombinant DDX58 upon mutant SOD1 co-expression.

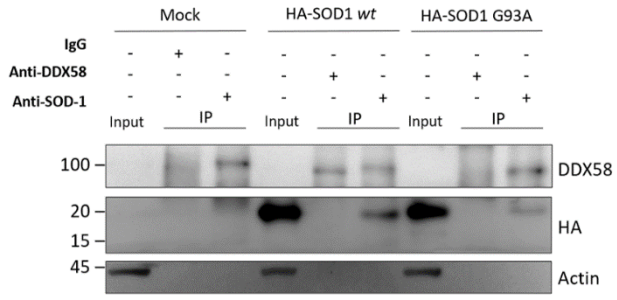

Figure 3.7 Ddx58 immunoprecipitation diminishes in HA-SOD1 G93A-overexpressing cells derived lysates. *Western blot of the IP experiment using anti-DDX58 and anti-SOD1 antibodies as baits. Anti-DDX58, anti-HA-tag and anti-actin blots are reported. Input is 1/10 of lysate volume. Type of lysate is reported on top of the figure.*

To understand the subcellular distribution of the SOD1-interacting Ddx58 in NSC34, we performed an explorative IP experiment coupled to cytosol/nucleus fractionation (Figure 3.8). We separated the native lysates in cytosolic and nuclear fractions, confirmed by GAPDH and Lamin A/C separation in the blot. In addition, we subjected the fractions to RNase A digestion, to assess the role of RNA in mediating the interaction,

and proceeded with anti-SOD1 IP. Interestingly, we noticed an increased Ddx58 co-sedimentation in the RNase-treated nuclear lysates, indicating that, in the absence of RNA substrate, the nuclear Ddx58 could be more available to bind SOD1. RNA digestion also improved the IP of Sod1 in the cytosol of HA-SOD1 lysate. Upon SOD1 overexpression we observed an increased abundance of nuclear Ddx58 in IPs. Albeit these indications, this experiment presents some critical aspects. One is the unspecific co-immunoprecipitation of GAPDH in the cytosolic fractions and Lamin A/C in the nuclear fraction. Another one is the signal of nuclear Ddx58 that appears to detect non-solubilized proteins, probably containing chromatin contaminants. These limitations hamper to draw conclusive remarks from this approach.

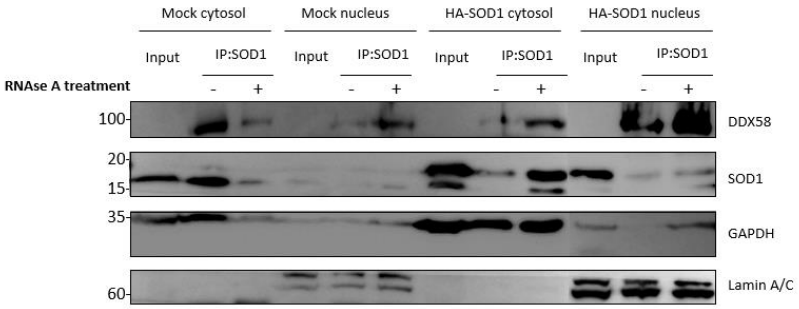

***Figure 3.8 Fractionation-IP approach trial**. Western blot of fractionation IP experiment using anti-SOD1 antibody as bait. DDX58, anti-SOD1 and anti-GAPDH and anti-Lamin A/C blots are reported. Input is 1/5 of lysate volume. Type of lysate and subcellular fraction is reported on top of the figure. RNase A digestion was performed prior to IP protocol.*

However, with these results we could speculate that a fraction of Ddx58 protein might interact with SOD1 depending on the protein dosage.

3.3 DDX58 is secreted and increases the secretion of extracellular RNA

We challenged our NSC34 cell model to investigate the possible secretion of DDX58 protein through extracellular vesicles (EVs).

We used differential ultracentrifugation (dUC) method to isolate EVs based on sedimentation coefficient, and we detected DDX58-tGFP protein in 10,000g fraction,

thus likely associated to larger particles, typically with a sub-micrometric diameter (Figure 3.9A). To overcome the limitation of ultracentrifugation, known to co-sediment protein aggregates in the pellet, we exploited an OptiPrep™ density gradient ultracentrifugation approach (adapted from Van Deun et al. 2014). By this approach, we managed to isolate also the endogenous protein specifically associated to EVs. The detection of DDX58 in correlation with the vesicular marker syntenin allowed us to estimate a 56% of the protein secreted in vesicular particles (Figure 3.9B). Regarding the ectopic counterpart, we retrieved most of the recombinant protein in the low-density fractions, meaning that DDX58-tGFP could be secreted as soluble free protein.

Furthermore, we tested if the secreted DDX58 protein is able to bind total RNA from a cell extract. To address this question, we incubated the lysate of dUC-EVs with total RNA

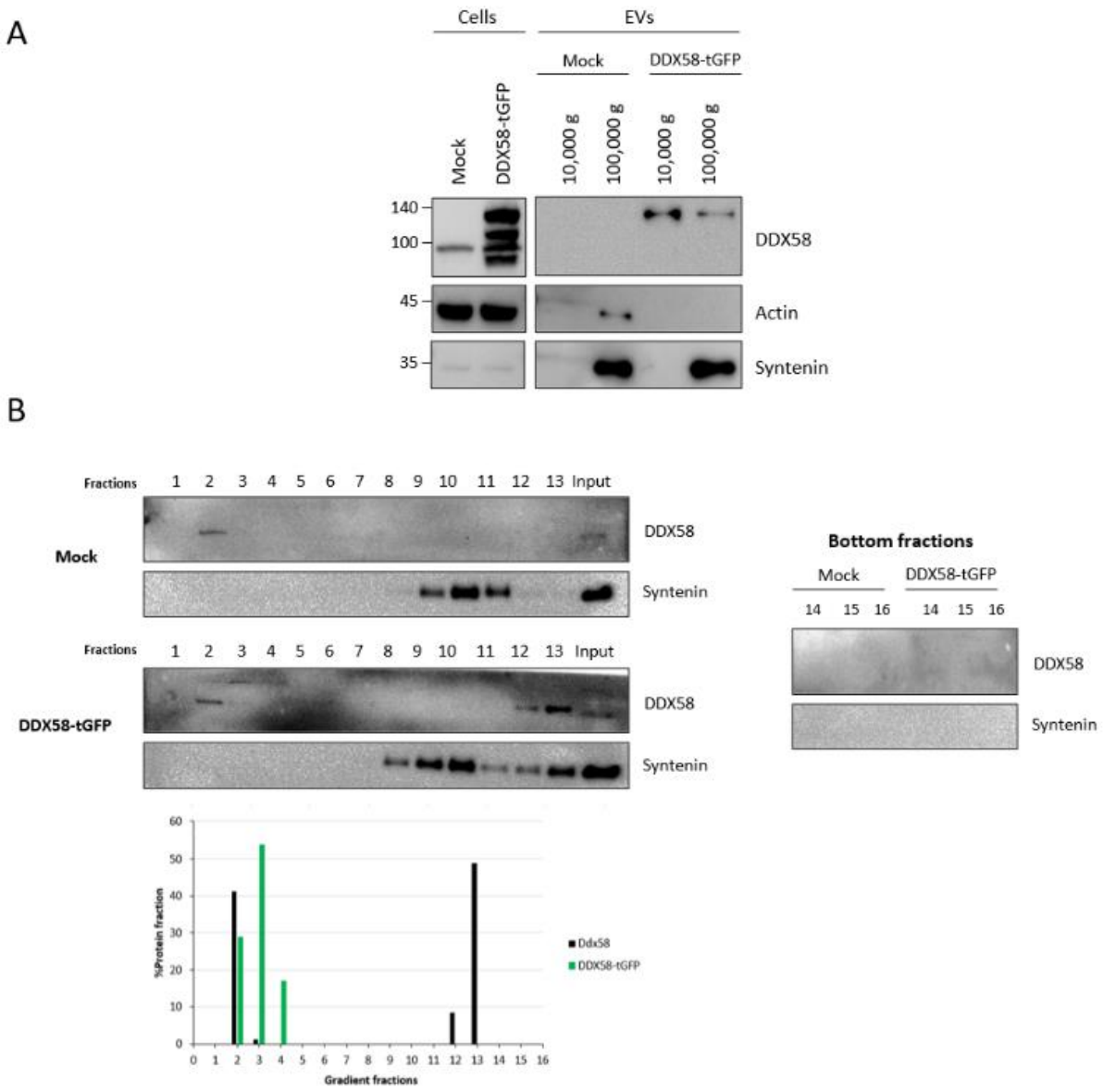

Figure 3.9 DDX58 protein is secreted in extracellular vesicles (EVs). *A) Western blot from NSC34 differential ultracentrifugation-derived EVs and corresponding input cells upon DDX58-tGFP overexpression. B) top left: OptiPrep™ density gradient ultracentrifugation. The number of fractions is directly proportional to the density of the fraction (from 1.02 to 1.25 g/mL). Input lane contains 1/10 of concentrated medium run in the gradient. Bottom left: densitometric analysis representing the fraction of endogenous and recombinant proteins retrieved over the total in DDX58-tGFP gradient (n=1). Top right: fractions from the bottom of the tubes.*

purified from steady-state NSC34. The anti-DDX58 immunoprecipitation revealed a 5-fold increase in isolated RNA compared to non-specific IgG (Figure 3.10). Moreover, RNase A treatment was performed on immunoprecipitates to check for a possible protection from RNA digestion due to RBP binding. Interestingly, we isolated a 1.5-fold higher amount of residual RNA in anti-DDX58 IP compared to IgG (Figure 3.10). These results indicate a possible role of EV-associated DDX58 in binding RNA.

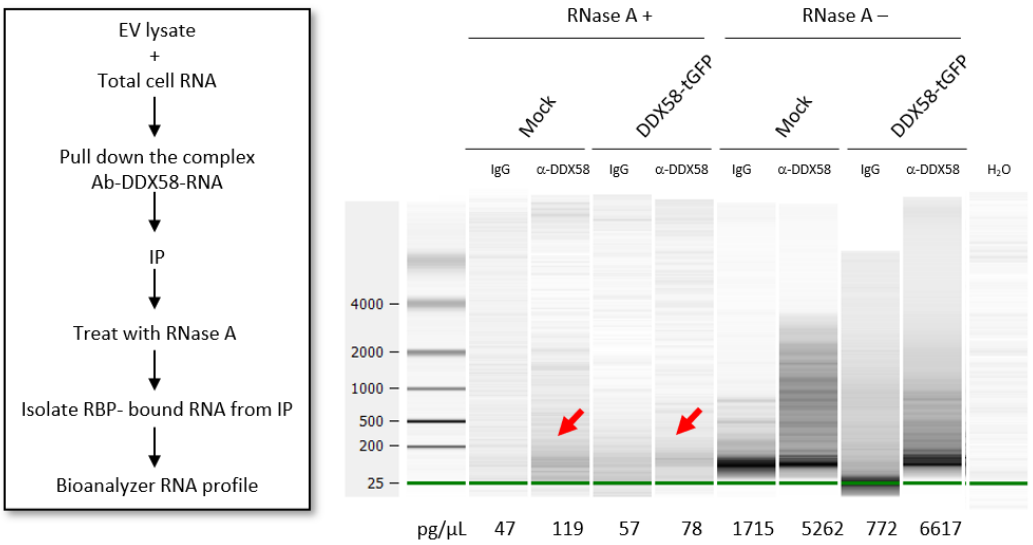

Figure 3.10 EV-associated DDX58 is able to bind total cellular RNA. *Left: workflow of the RIP approach used. Right: RNA capillary gel electrophoresis at Bioanalyzer. The red arrows indicate the residual RNA amount immunoprecipitated after RNase digestion. On the bottom of the gel, the reported RNA quantification from the corresponding lane as calculated by the smear analysis.*

In order to assess the quantity of RNA released in EVs from DDX58-tGFP overexpressing cells, we exploited Nickel-based isolation (NBI). In fact, NBI technology allows the purification of heterogenous, polydisperse and pure EVs depending on the particle negative charge. It is based on the use of positively charged nickel beads to capture EVs and an elution buffer that minimizes the co-isolation of extracellular free proteins (Notarangelo et al. 2019, 2020).

We overexpressed the protein for 48 h or 72 h and observed a time-dependent shift in the size distribution profile retrieved from Nanoparticle Tracking Analysis (Figure 3.11A). After particle quantification, the eluted EVs were subjected to RNA purification as described in section 6.6. The EV-RNA was profiled at Bioanalyzer via capillary gel electrophoresis and the profile shown in Figure 3.11C represents a defined peak corresponding to transcripts below 200 nt in length, as expected (Enderle et al. 2015). The relative quantification of the total EV-RNA per vesicle demonstrated a significant 2-fold increase of EV-associated amount of upon DDX58-tGFP expression in EVs recovered 48h post-transfection; the effect is lost at 72h (Figure 3.11B).

Taken together, these data indicated a possible acute response upon DDX58 upregulation associated with an increased release of RNA, which is compensated after 72 hours of transfection. This suggested the presence of post-transcriptional dynamics influencing the EV-RNA and probably its quality.

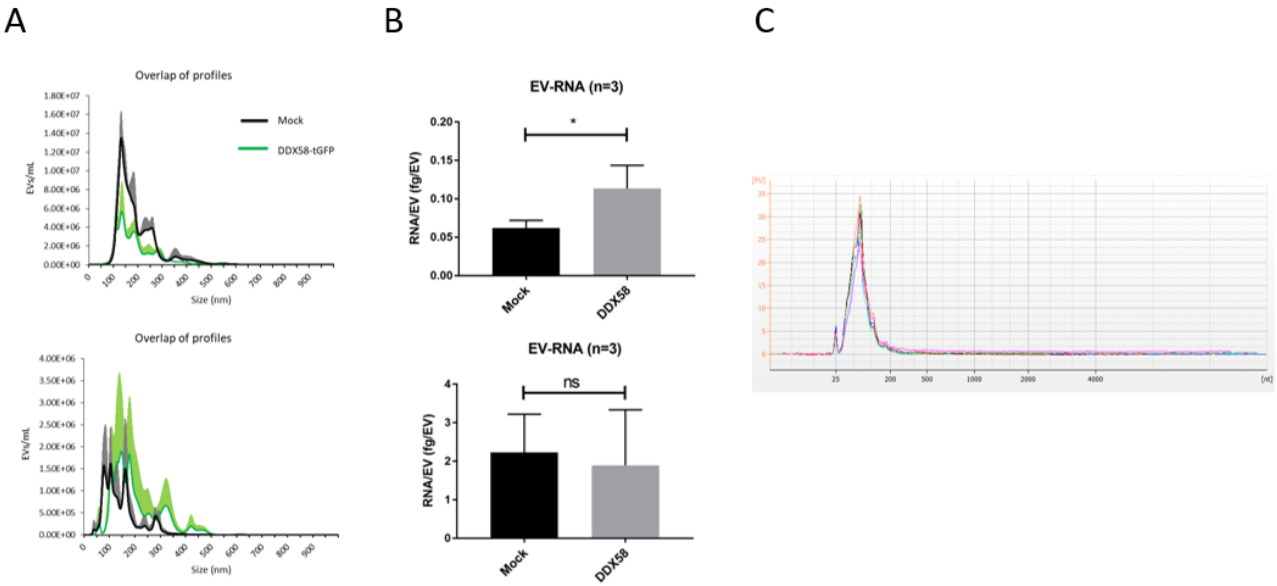

Figure 3.11 EV-RNA profiling upon DDX58-tGFP overexpression. *A) Nanoparticle Tracking Analysis on EVs derived from mock or DDX58-overexpressing NSC34. On top is the result from EVs recovered 48 h after transfection, on bottom 72 h after transfection. The overlapped profiles result from an average of n=3 independent biological replicates. Mean ± SD is plotted. B) EV-RNA amount calculated from Bioanalyzer and normalized for the EV count for mock and DDX58-tGFP transfected NSC34. On top is the result from EVs recovered 48 h after transfection, on bottom 72 h after transfection. Quantification reports Mean ± SD of n=3 independent biological replicates. C) Representative overlap of EV-RNA profiles from all the experimental conditions described. T-test *P-value <0.05; ns non-significant.*

3.5 DDX58 and SOD1 are co-secreted in EVs and affect EV-RNA secretion

As previously reported, SOD1 protein is secreted in the spinal cord (W. Zhao et al. 2010) and associates to small EVs protein cargo from SOD1 overexpressing NSC34 cells (Silverman et al. 2019). Considering the observed secretion of DDX58 protein and the data on the intracellular interaction between DDX58 and SOD1, we decided to investigate their relative abundance in extracellularly secreted particles. For this purpose, we transfected NSC34 for 48 h with DDX58 and SOD1-encoding plasmids and performed EV isolation by differential ultracentrifugation. We confirmed the

enrichment of DDX58 (both the endogenous and tGFP-tagged proteins) in the 10,000g pellet, co-sedimenting with larger vesicles (Figure 3.12A). We did not detect HA-SOD1 G93A protein in the vesicles, in accordance with the reported release of misfolded aggregates (Silverman et al. 2019), non-detectable by our antibody, that might have sequestered also the endogenous protein in insoluble fraction. Nevertheless, as we expected, we detected HA-SOD1 wt protein associated to 100,000g pellet, co-sedimenting with smaller EVs. The same distribution was observed also for the endogenous Sod1. Of notice, the overexpression of DDX58 resulted in a 10-fold increased Sod1 distribution in larger EVs with respect to smaller EVs (Figure 3.12B). Moreover, when we co-expressed SOD1 wt with DDX58-tGFP we observed a more diffused distribution of SOD1 that presented a 3-fold increased abundance in larger particles compared to smaller particles due to DDX58 co-expression (Figure 3.12B). Accordingly, also DDX58 in the conditions of co-expressions showed a more homogenous distribution between large and small EVs when compared to the single DDX58-tGFP transfection.

We hereby showed a first hint that the two proteins could influence their mutual extracellular secretion, perhaps linked to a local intracellular interaction, providing a first indication of the possible interplay of DDX58 and SOD1 proteins in paracrine intercellular communication.

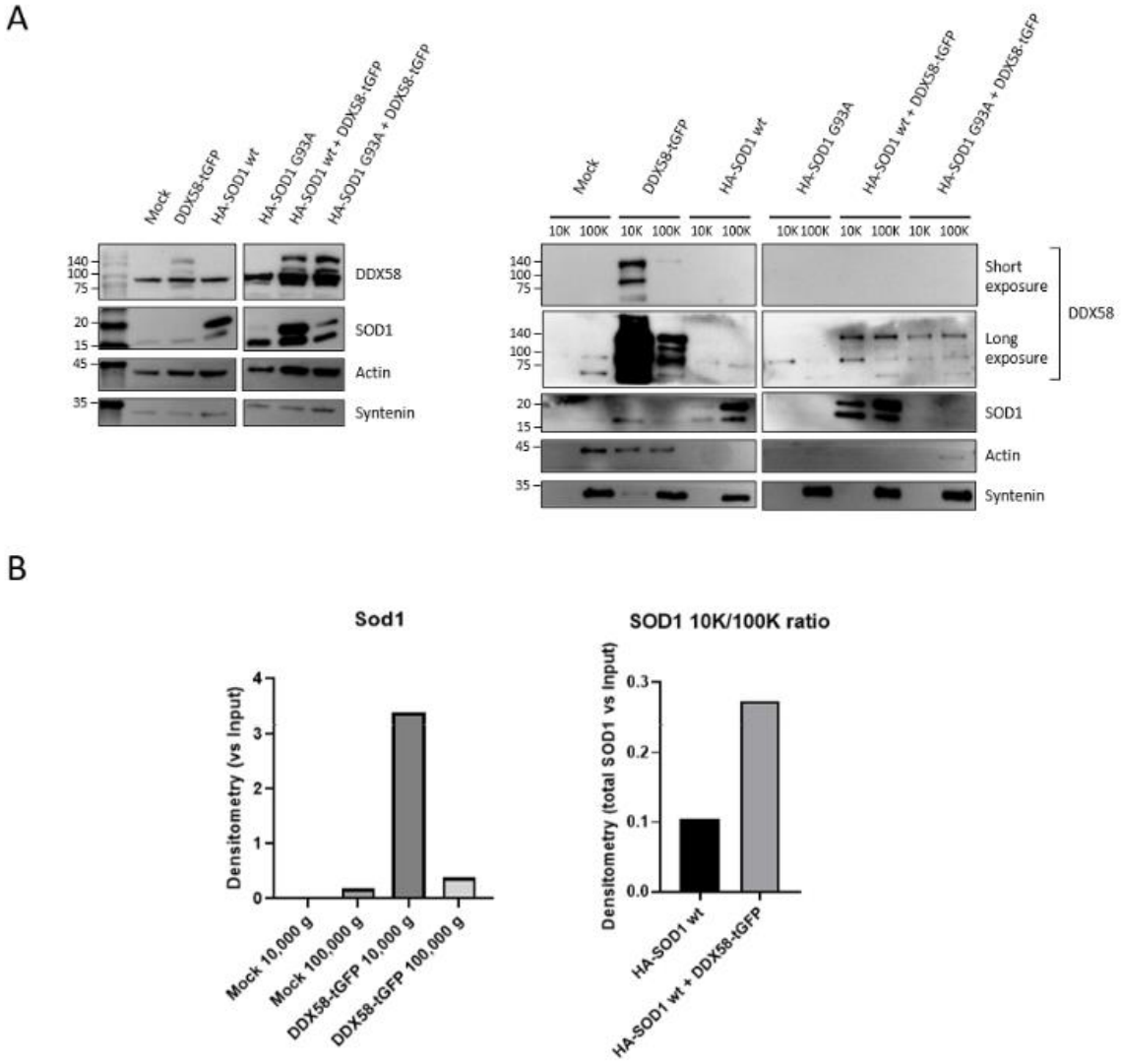

Figure 3.12 DDX58 and SOD1 are co-secreted in EVs. *A) Western blotting showing the distribution of endogenous and recombinant DDX58 and endogenous and recombinant SOD1 wt/G93A proteins in larger (10K=10,000g pellet) and smaller (100K=100,000g pellet) EVs. On the left, the input transfected cells of origin. On the right, the respective dUC-isolated EV-samples. B) Left: densitometric quantification of Sod1 normalized over the input. Right: densitometric quantification of SOD1 wt 10K/100K ratio over the corresponding total SOD1 input. Quantification relative to n=1 biological replicate shown in A.*

Given the DDX58-dependent EV-RNA amount alterations observed in paragraph 3.3, we decided to analyze the releasing of EV-associated RNA upon the overexpression of DDX58 and SOD1. Indeed, SOD1 ALS-mutations has been associated to differential secreted RNA signatures found in patients biofluids (Katsu et al. 2019) (Banack, Dunlop,

and Cox 2020). In confirmation, recently miRNA biogenesis was shown to be affected by SOD1 mutant protein (X. Chen et al. 2022). Therefore, we expect a contribution to the deregulation of EV-RNA upon overexpression of a recombinant SOD1 protein.

Similarly, exploiting Nickel-based isolation we isolated EVs from NSC34 expressing HA-SOD1 wt and G93A or in co-expression with DDX58-tGFP-encoding plasmid. We isolated EVs 48 h post-transfection and, as shown in Figure 3.13A, we did not observe significant differences in the size distribution and particle concentrations from the NTA. After total EV-RNA quantification by Bioanalyzer, we reported a significant increase in the secretion of EV-RNA upon co-transfection of DDX58-tGFP and HA-SOD1 G93A (Figure 3.13B).

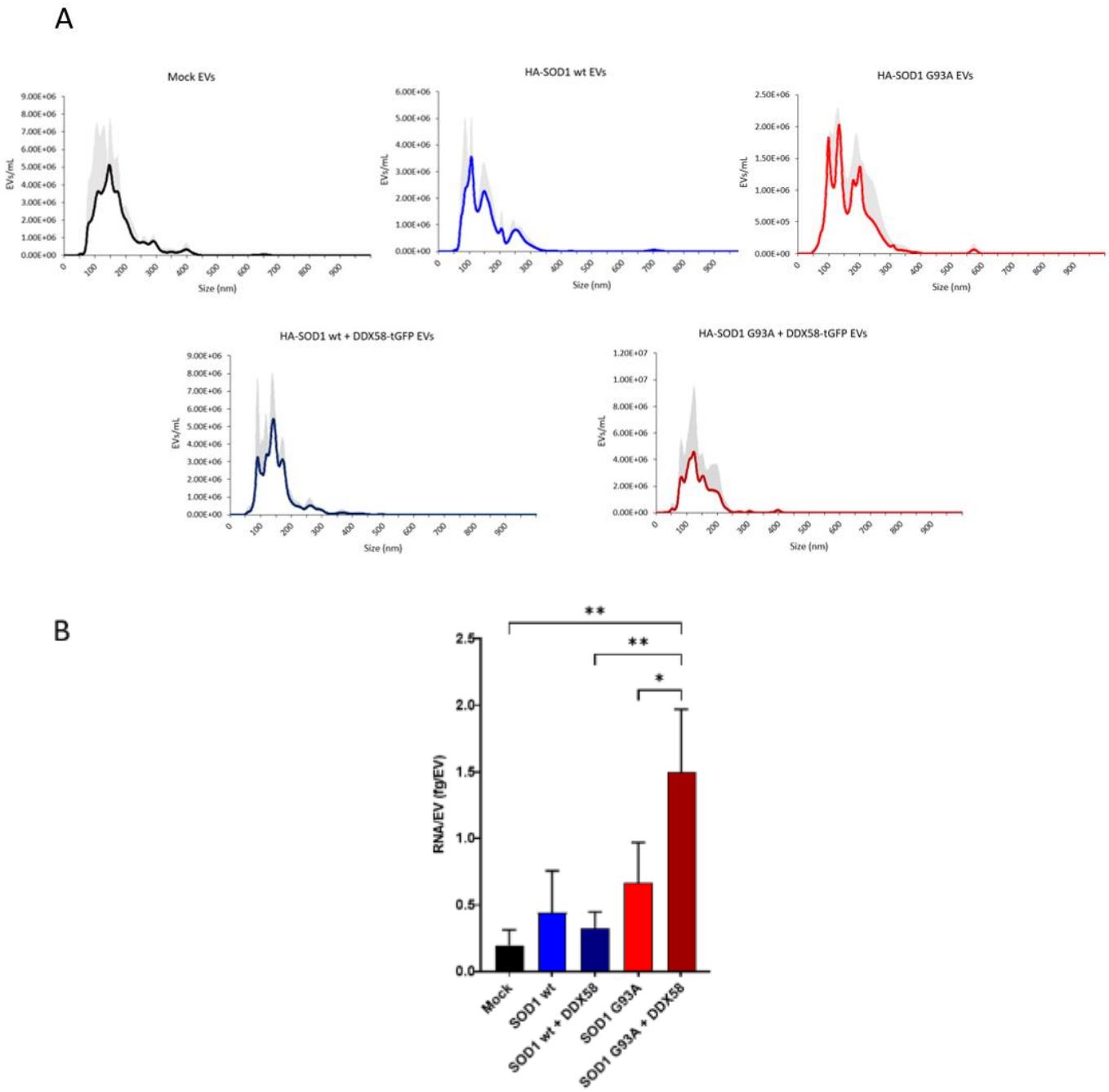

Figure 3.13 EV-RNA profiling from DDX58 and SOD1 co-expressing cells. *A) Nanoparticle Tracking Analysis on EVs derived from 48 h transfected NSC34. Shown overlapped profiles result from an average of n=3 independent biological replicates. Mean ± SD is plotted: mean in colors, SD in light grey. B) EV-RNA amount calculated from Bioanalyzer and normalized on the EV count for mock and DDX58-tGFP transfected NSC34. On top is the result from EVs recovered 48 h after transfection, on bottom 72 h after transfection. Quantification reports Mean ± SD of n=3 independent biological replicates. ANOVA *P-value <0.05; **P-value <0.01.*

Given the possible local interaction and EV co-secretion of the two proteins, we hypothesized that DDX58 and SOD1 co-operate to regulate the EV-RNA cargo. Notwithstanding, SOD1 protein is not annotated for RNA-binding activity and it is found

in stress granules as a non-RNA-binding component (Gal et al. 2016) (Da Ros et al. 2021). Therefore, we wondered whether DDX58 is involved in the direct binding of co-regulated EV-RNA. To answer this question, we exploited a pipeline, set up in our lab, to biotinylate a heterogenous population of EV-RNA and use it as a bait in a pull down experiment. In particular, the biotinylation strategy is summarized in Figure 3.14A: briefly, we exploited a commercial 3'-poly(A) polymerase and hybridized the RNA poly(A) tail with an oligo-dT carrying a biotin-TEG moiety. In Figure 3.14B, we observed that, in this setting, Ddx58 is pulled down in a nonspecific manner, whilst the pull down of the recombinant DDX58 show a 3-fold increase when we used an EV-RNA bait deriving from co-transfected cells rather than control. As for SOD1, we barely detected the endogenous protein in the pull down conditions, meaning that the signal could be due to technical carry over. Consistently, regarding HA-SOD1 we do not report an enrichment of the protein upon the usage of different EV-RNA baits, reflecting an interaction not dependent on the RNA quality. We point out that the input RNA amount used to generate the two biotinylated EV-RNA pools (mock and co-transfected) is the same, then we could ascribe the enrichment in pull down to the simple differences in RNA quality secreted, and exclude an artifact of the transfection. This data suggested that, differently from HA-SOD1 protein, DDX58-tGFP might preferentially bind RNA sequences released in EVs upon the DDX58-SOD1 co-expression.

Moreover, it motivated the identification of a mechanism of DDX58-mediated exacerbation of EV-RNA loading upon mutant SOD1 protein expression.

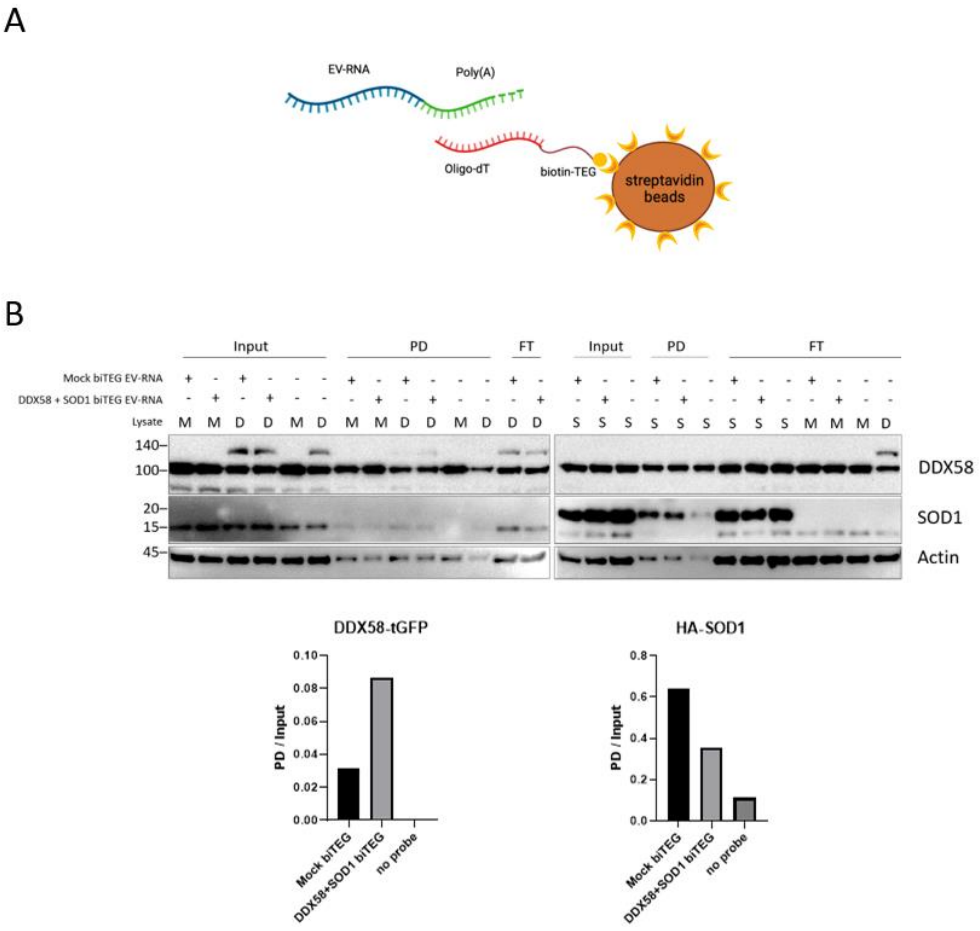

Figure 3.14 Biotinylated EV-RNA pulldown assay on recombinant DDX58 and SOD1 overexpressing lysates. *A) EV-RNA biotinylation strategy. In the cartoon, EV-RNA (in blue) is polyadenylated (green) upon commercial poly(A)polymerase reaction; biTEG-ligated oligo dT Is hybridized and streptavidin-coated beads are used for the capture. B) Western blotting on mock (M), DDX58-tGFP (D) and HA-SOD1 wt (S) lysates. PD=pull down; FT=flow-through. Densitometry is shown on the bottom, relative to n=1 biological replicate.*

In the context of the PhD project consortium (MIUR PRIN 2017), we had the opportunity to utilize SOD1 G93A mouse primary astrocytes, an ALS model that better recapitulates the phenotypic alterations occurring in the disease. Therefore, we decided to verify if, on primary astrocytes, EV-RNA secretion is altered in the presence of SOD1 G93A mutation.

3.6 SOD1 G93A mutation in primary astrocytes enhances EV-RNA secretion

To study the role of secretion of EV-RNA from SOD1 G93A mouse model astrocytes, we collaborated with Prof. Giambattista Bonanno's group at the Department of Pharmacy in the University of Genova. Astrocytes primary cultures were set up in Genova as described before (Provenzano et al. 2022). As already reported in the PhD thesis of Dr. Roberta Zerbo (entitled "Characterization of the extracellular vesicles released by astrocytes cultured from the spinal cord of the late symptomatic SOD1G93A mice, a model of amyotrophic lateral sclerosis"), in the frame of a collaborative project, we received the cell-conditioned media to perform EVs isolation and biophysical characterization and EV-RNA extraction and profiling.

In order to recover a heterogeneous population of EVs, the isolation was performed using NBI method. EVs were characterized in terms of EV number, size and zeta potential as follows. Figure 3.15A shows the profile of size and particle count at qNano instrument using tunable resistive pulse sensing (tRPS) technique. Differently from NTA that is based on particles light scattering properties, tRPS allows the detection of the physical passage of single nanoparticles through a nanosized pore, measuring a blockade of current in electrolyte solution. We analyzed size and concentration profiles of EV-samples from both neonatal and adult astrocytes deriving from spinal cord and from neonatal cortex astrocytes. We did not observe significant variations on the size of the particles, characterized by an average mean diameter of 319.3 ± 42 nm and a mode diameter of 213.1 ± 17.6 nm, a result in line with prior analyses on astrocytes-EVs (D'Arrigo et al. 2021). The concentration of particles did not change significantly although we observed a trend of increased abundance in the adult SOD1 G93A mice-derived EVs (Figure 3.15A). Also, increased particle concentrations were obtained from the neonatal cortex, although the number of samples received in this case was limited to draw conclusions. Adult astrocytes, in comparison with neonatal ones, were selected in the study because of their pertinence with the neurotoxic phenotype in ALS (Díaz-Amarilla et al. 2011). Hence, adult astrocytes-derived EVs were further characterized in terms of bulk nanoparticle concentrations via NTA and no difference in particle concentrations was

noted between wt and mutant-derived EVs (Figure 3.15B). Since the surface charge of intact and pure EVs is expected to be negative (Gelibter et al. 2022), we characterized the zeta potential of wt and SOD1 G93A mouse model derived EVs. Accordingly, we found a zeta potential of -10.3 ± 1.7 mV for wt EVs and -12.0 ± 3 mV for G93A EVs (Figure 3.15B). Subsequently, we profiled the EV-RNA and quantified it via capillary gel electrophoresis (Figure 3.15C). The reported normalization takes into consideration the total amount of particles as calculated by the NTA experiment on part of the eluted

vesicles after NBI purification. Interestingly, we found that G93A-derived EVs contained up to 3-fold the amount of total RNA per vesicle (Figure 3.15C).

The increased EV-RNA release from SOD1 mutant primary astrocytes supported our data relative to DDX58-SOD1 co-regulated EV-RNA secretion from NSC34. Therefore, we decided to assess the quality of DDX58- and SOD1-dependent secreted RNA performing a global transcriptomic analysis of the two cell types.

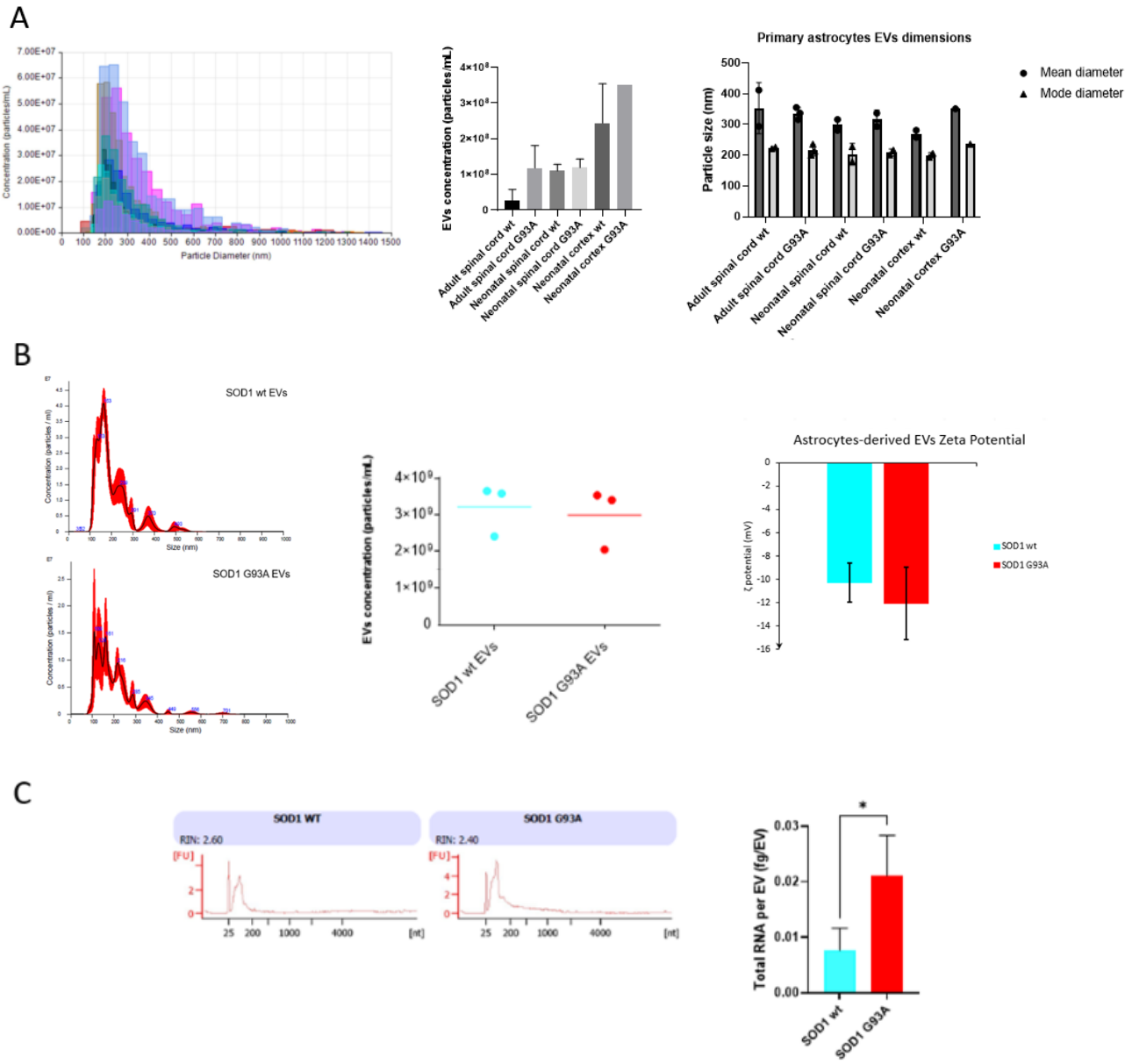

Figure 3.15 SOD1 G93A mouse model primary astrocytes-derived EVs characterization. *A) TRPS analysis of adult and neonatal astrocytes. Respectively: overlapped profiles from qNano, particle concentrations, particle size. Mean ± SD is reported. SD is representative of n=3 biological replicates. B) NTA analysis on adult spinal cord astrocytes EVs. Representative NTA profiles, EVs concentrations, particle zeta potential assessments. Mean ± SD is reported. SD is representative of n=3 biological replicates. C) EV-RNA profiling from adult spinal cord astrocytes. Representative RNA profiles, EV-RNA quantification normalized on EV count. Mean ± SD; t-Test *P-value <0.05.*

3.7 RNA-Seq supports the indirect role of DDX58 in EV-RNA secretion

3.7.1 DDX58 and SOD1 impact EV-associated microRNA secretion

In a comprehensive RNA-Seq experiment, we decided to sequence on the same flow cell RNA samples deriving from both NSC34 and primary astrocytes.

Using NSC34, we set up a first experimental condition using DDX58-overexpressing cells and corresponding EVs. We included a fluorescent associated cell sorting (FACS)-Seq approach to separate transfected from non-green cells and the corresponding EVs. We transfected DDX58-tGFP for 24h and sorted the cells to separate tGFP-negative from tGFP-positive populations according to the GFP signal. We cultured the cells for 48h and subjected them to EV isolation and EV-RNA extraction, as described above, and proceeded to cDNA library preparation.

Since EVs are enriched with short-sequence RNA fragments below 40 nt (Pérez-Boza, Lion, and Struman 2018), we applied a pipeline, optimized in our lab, to sequence miRNA-enriched cDNA libraries for Illumina-based Next Generation Sequencing, using QIAseq miRNA library kit (Qiagen).

To describe differentially expressed genes (DEGs), a first analysis was performed by our collaborators in University of Genova, group led by Dr. Margherita Squillario. The analysis was performed via DESeq2 and edgeR algorithms. Considering the EV-associated transcriptomes deriving from tGFP-positive and tGFP-negative cells, we found 9 DEGs out of which 3 were identified by both algorithms: 1 upregulated miRNA (mmu-miR-709) and 2 downregulated miRNAs (mmu-miR-130b-5p and mmu-miR-181a-2-3p) in EVs derived from tGFP-positive cells (Figure 3.16). This observation is in line with the number of miRNAs identified by comparing the EVs to the corresponding cell of origin: in fact, 75 upregulated miRNAs in EVs and 6 in the cell were found for the tGFP-

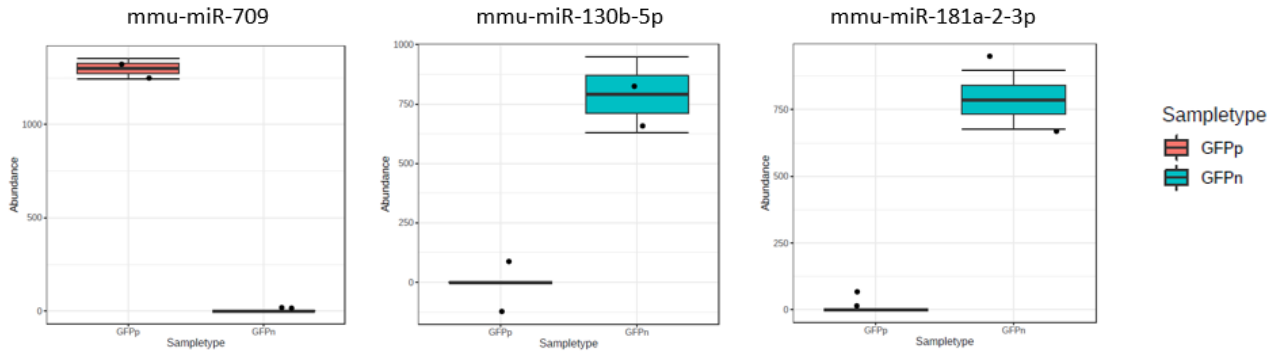

Figure 3.16 Differentially abundant miRNAs in EVs upon DDX58-tGFP expression. *Box plots relative to the significant differentially expressed miRNAs reported in relative filtered reads count. GFPp=tGFP-positive cells-derived EVs; GFPn=tGFP-positive cells-derived EVs*

negative condition, 85 upregulated miRNAs in EVs and 9 in the cell were found for tGFP-positive condition.

These data, despite the observed high miRNA secretion and low cell retention in NSC34, suggested that DDX58 alone might only slightly impact the secretion of miRNA in EVs. In addition, we ran on the same NGS experiment EV-RNA samples deriving from NSC34 co-expressing DDX58-tGFP along with HA-SOD1 wt or G93A mutant. This approach aimed to identify co-regulated transcripts that are differently secreted upon either the interaction of the two proteins or to the presence of the ALS mutation. Surprisingly, we found only one significantly downregulated target (mmu-miR-542-5p) in EVs deriving from DDX58-tGFP+HA-SOD1 G93A condition (Figure 3.17). This comparison supported the fact that the differently released EV-RNA amount observed quantifying the global RNA at Bioanalyzer might be due to a dosage unbalancing or not dependent on the considered small ncRNA species.

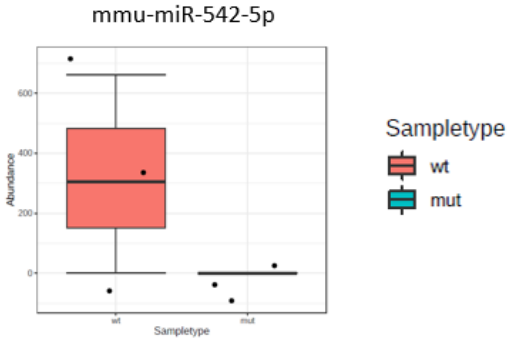

Figure 3.17 Differentially abundant miRNA in EVs from DDX58-SOD1 co-expressing NSC34 *Box plot relative to the significant differentially expressed miRNA reported in relative filtered reads count. wt=DDX58-tGFP+HA-SOD1 wt-derived EVs; mut=DDX58-tGFP+HA-SOD1 G93A-derived EVs*

Regarding the samples from astrocytes, we analyzed both vesicular and corresponding cellular transcriptomes of wt and SOD1 G93A astrocytes.

Interestingly, from the comparison of the two EV transcriptomes we identified 8 DEGs: 5 up- and 3 down-regulated miRNAs in the mutant condition (mmu-miR-6999-3p, mmu-miR-3101-3p, mmu-miR-93-5p, mmu-miR-9-5p, mmu-miR-221-3p resulted upregulated; mmu-miR-760-5p, mmu-miR-6974-3p, mmu-miR-10b-5p resulted downregulated). The number of DEGs confirmed that EVs deriving from G93A astrocytes are enriched with upregulated miRNAs when we compared the transcriptome with the corresponding cell of origin: we identified 106 upregulated miRNAs and 26 downregulated miRNAs in the G93A EVs; while only 16 miRNAs resulted significantly upregulated in wt astrocytes-derived EVs and 102 downregulated compared to the cellular counterpart (Figure 3.18).

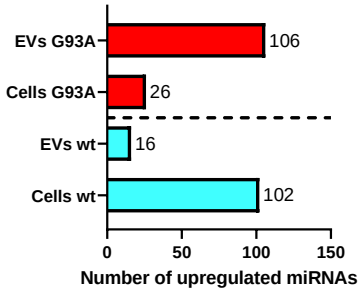

Figure 3.18 Number of DEGs in EV vs cell comparison from SOD1 astrocytes. *Number of significant up-and downregulated DEGs in EVs vs cell of origin. In red, SOD1 mutant astrocytes, in cyan SOD1 wt astrocytes*

A functional annotation of the mRNA targets is shown in Figure 3.19A. In accordance, the gene ontology (GO-BP) of the targets revealed a heterogeneous panel of biological processes regulated by the miRNAs differentially packaged in the mutant-derived EVs. Remarkably, using target prediction via miRWalk software, we identified 430 genes globally affected by mutant SOD1 EV-released miRNAs. These genes were annotated into 34 KEGG (Kyoto Encyclopedia of Genes and Genome) pathways. Among these, we reported the “Axon guidance pathway” (mmu_04360) and the ”Neurotrophin signaling pathway” (mmu_04722) for which respectively 13 and 9 target mRNAs were described to be controlled post-transcriptionally by the mutant astrocytes secreted miRNAs. The

only mRNA target that had more than 2 nodes in a STRING analysis resulting from a comparison of the upregulated miRNA was Atxn1 (Figure 3.19B).

This gene encodes for ataxin-1 and it was associated with familial ALS, besides spinocerebellar ataxia type 1 (Tazelaar et al. 2020). Also ATXN1 ablation was associated with a dysfunctional pro-inflammatory B cell compartment in multiple sclerosis

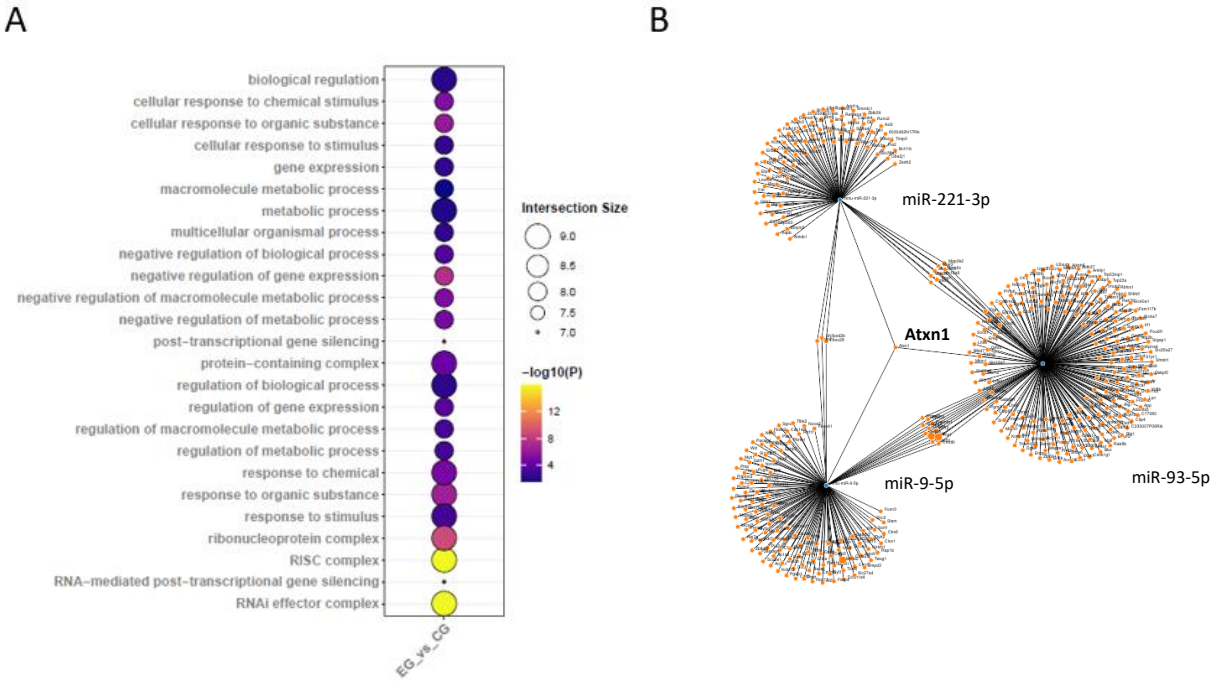

Figure 3.19 Gene ontology (GO-BP) of SOD1 G93A EV-modulated targets. *A) Balloon plot visualizes significant enriched terms from mRNA targets predicted from the dataset in the comparison SOD1 G93A EV vs cell. The dimension of the balloon reports the number of miRNAs intersected to the biological pathway, the color is -log10 of the adj. P value C) STRING interaction network of co-regulated mRNA targets from shown upregulated miRNAs in mutant EVs. Atxn1 is the common target in the middle of the three nodes of the network.*

(Didonna et al. 2020). Among other functions, the differential EV cargo deriving from mutant astrocytes might decrease the expression of ataxin-1 in the CNS and then increase neuroinflammation.

Altogether, the analyses revealed an unbalance of secreted miRNAs strictly associated with the presence of SOD1 mutation in primary astrocytes. The annotation of the identified miRNAs supports the speculation of the paracrine EV-mediated post-transcriptional regulation exerted by ALS mutant astrocytes.

3.7.2 Comprehensive analysis supports the DDX58-associated SOD1-induced EV-RNA loading

In order to deepen the computational analysis following pipelines already developed for vesicular small ncRNAs, we collaborated with Prof. Silvano Piazza's group (ICGEB, Trieste).

The principal component analysis carried out on astrocytes-related data (Figure 3.20) indicates a higher difference in the x axis (89% variance in PC1) rather than the y axis (4% in PC2), indicating how the transcriptomes originated from EV samples were considerably differing from the cell-derived samples (PC1 contribution). Additionally, the mapped transcriptomes were virtually undistinguishable considering just the mutational state (PC2 contribution).

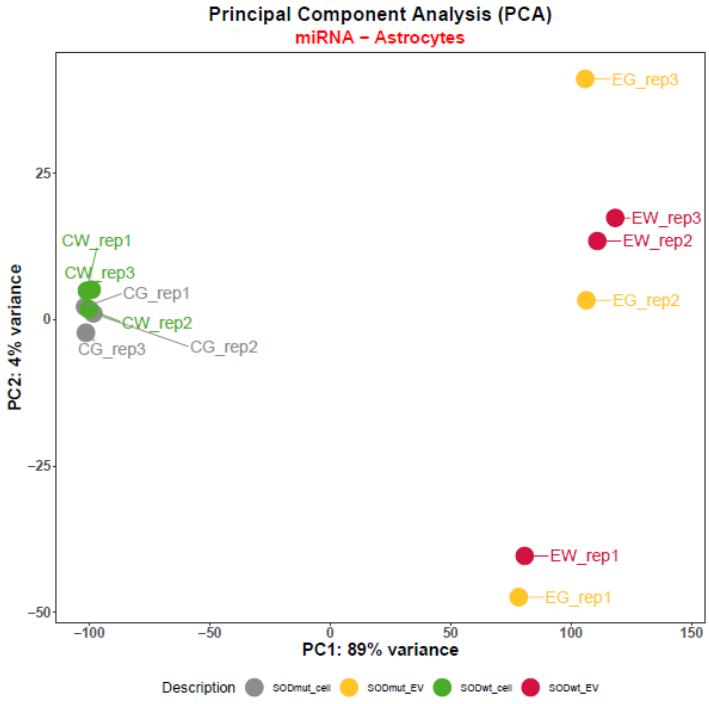

Figure 3.20 Principal component analysis from astrocytes datasets. *Computational dimensional reduction analysis well-separating the two types of datasets: CW, CG (cells); EW, EG (EVs). Rep stands for biological replicate.*

This analysis provides a quality check on the differential abundance analysis already shown as the astrocytes EV transcriptomes appeared significantly different from cellular

ones. It also supported the fact that, in this model, the mutant SOD1-dependent alteration of secreted RNA quality could interest the already described differentially abundant transcripts rather than being a generalized effect.

Regarding the samples deriving from NSC34 cells, we could screen an additional miRNA target from the same dataset: in Figure 3.21A, we report the upregulation of mmu-miR-203-3p in EVs from tGFP-positive cells compared to the control EV transcriptome.

Additionally, using a heatmap we could clusterize differently expressed miRNAs in the sorted cells into two separate groups (Figure 3.21B). This result emphasizes the fact that an unbalanced expression of DDX58 could generate a differential pattern of miRNAs at the intracellular level. This observation is in line with the altered RNA secretion through EVs upon DDX58 overexpression.

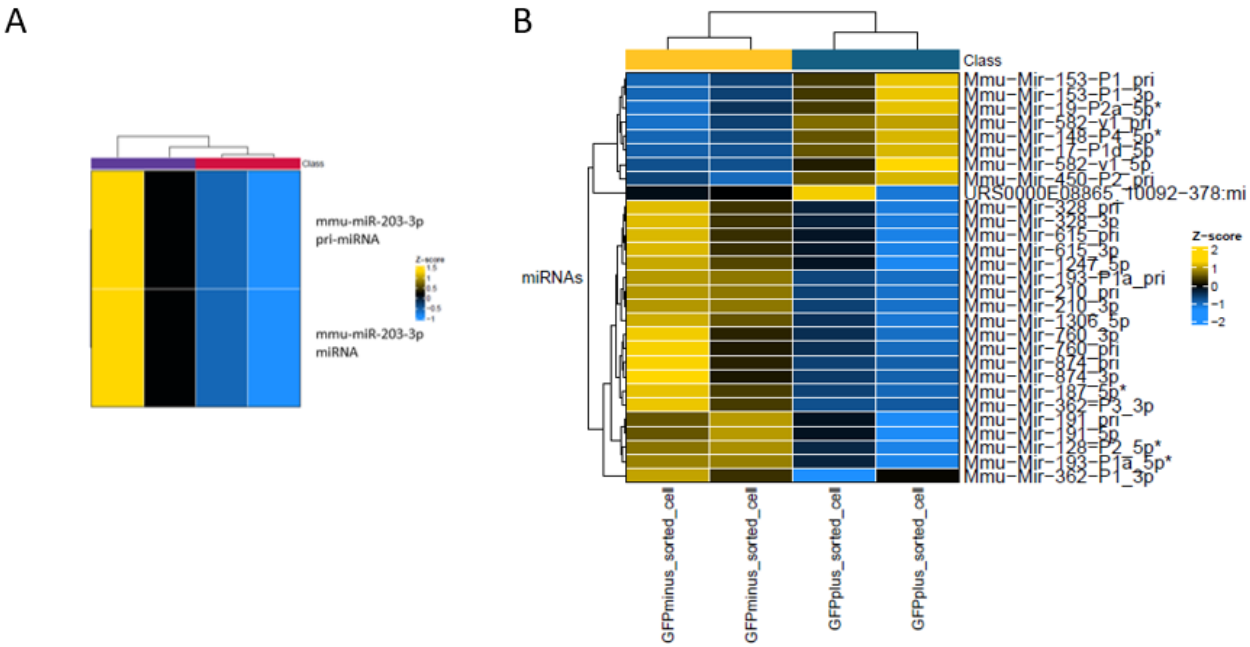

Figure 3.21 Heatmaps from DDX58-tGFP sorted cells datasets. *A) Heatmap showing the differentially abundant miRNA sequences comparing EVs from tGFP-positive cells (Class in violet) and EVs from tGFP-negative cells (Class in red). Coloring represents Z-score of the normalized expression levels (yellow upregulated, cyan downregulated). B) Heatmap showing the differentially abundant miRNA sequences comparing tGFP-positive cells (Class in gold) and tGFP-negative cells (Class in blue). Coloring represents Z-score of the normalized expression levels (yellow upregulated, cyan downregulated).*

Importantly, by comparing the dataset of EVs from DDX58-SOD1 co-expressing cells with the dataset of EVs from DDX58-tGFP sorted cells, we observed that, only in the presence of HA-SOD1 G93A, 19 transcripts were enriched in the vesicles (Figure 3.22). This is interesting, considering that the other possible comparisons in this context resulted with 0 differentials. The majority of the annotations referred to primary-miRNA (pri-miRNA) sequences except for mmu-miR-296-3p and mmu-miR-423-3p. The abundance of pri-miRNA transcripts might be ascribable to an asymmetric DROSHA cleavage mechanism already described for human cells (Nguyen et al. 2020), in concordance to presence of fragmented RNA in EVs. Although interesting, this finding necessitates future investigation and remains an open question.

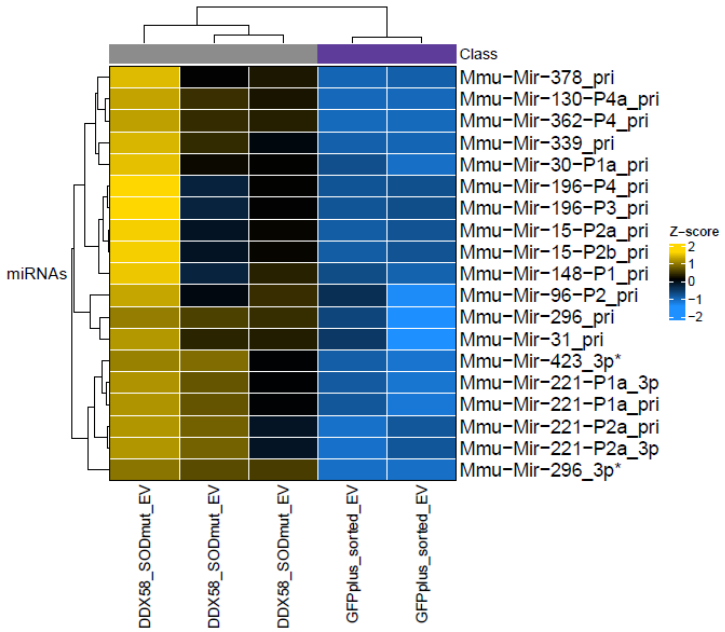

Figure 3.22 Heatmap from SOD1 G93A co-expression vs DDX58-tGFP sorted cells datasets. *Heatmap showing the differentially abundant miRNA sequences comparing EVs from DDX58+SOD1 G93A NSC34 cells (Class in grey). and EVs from tGFP-positive cells (Class in violet) Coloring represents Z-score of the normalized expression levels (yellow upregulated, cyan downregulated).*

However, the ongoing analysis point out that there might be specific transcripts differentially secreted upon modulation of DDX58 in co-overexpression of the ALS-mutant SOD1 protein.

3.8 Validation & functional connections

3.8.1 Preliminary validation using Droplet Digital PCR (ddPCR)

We initiated a miRNA validation phase to assess how the EV-RNA content is affected upon the expression of the DDX58 and SOD1. To generalize the mechanism and to gain preliminary insights on samples of human origin, we decided to test HEK293T cells and human motor neuron progenitors (details in Section 6.1 and 6.2) transfected with DDX58-tGFP and HA-SOD1. In particular, we set up Droplet Digital PCR (ddPCR) experiments on selected targets from the bioinformatic analysis. We selected hsa-miR-1910-3p (human homologous of mmu-miR-709, upregulated miRNA in EVs from tGFP-positive cells) and hsa-miR-130b-5p (downregulated miRNA in EVs from tGFP-positive cells). We extracted RNA from EVs and performed miRNA-enriched retrotranscription with the Advanced miRNA cDNA Synthesis kit (ThermoFisher). In EVs from HEK293T cells, we did not consistently observe an upregulation of the miR-1910-3p upon DDX58 modulation, also considering the suboptimal amplification detected via ddPCR assay (Figure 3.23A), suggesting that the secretion of this miRNA could be variable or not strongly influenced by the expression of DDX58-tGFP alone. In the same cell line, a decreasing hsa-miR-1910-3p detection trend was observed upon expression of HA-SOD1 wt. Similarly, hsa-miR-130b-5p secretion did not appear to be downregulated by the overexpression of DDX58 and SOD1 and upon co-expression of the two proteins. Nevertheless, in the input cells, we observed a stable miR-130b amplification rather than

in the EVs (Figure 3.23B), supporting the possibility of a rearranged packaging and secretion of the target, rather than a transcriptional event.

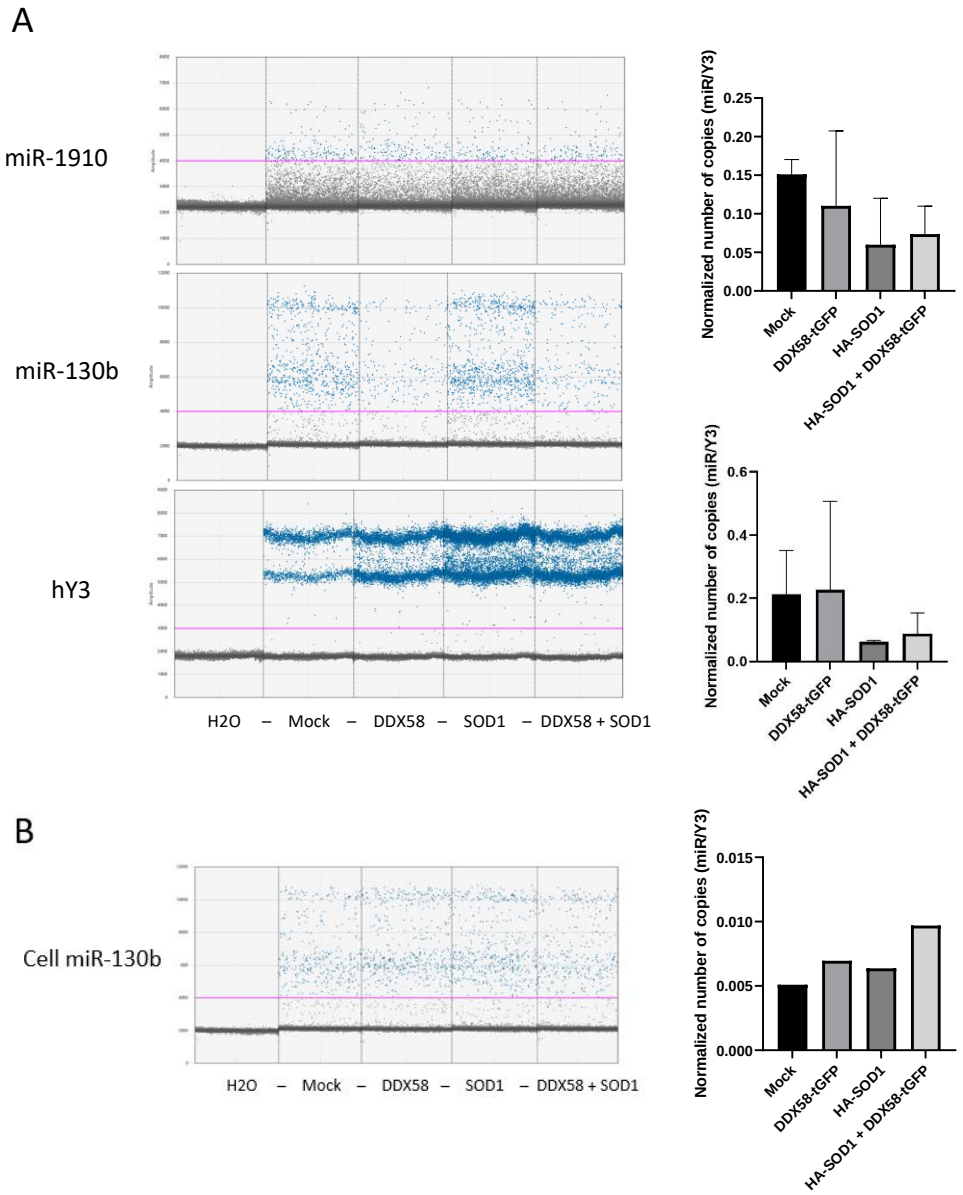

Figure 3.23 Digital droplet PCR miRNA assays in HEK293T cells. *A) miR-1910-3p and miR-130b-5p ddPCR on DDX58-tGFP, HA-SOD1 wt or co-expressing transfected HEK293T-derived EVs. On the left representative droplets containing the amplified PCR product. Threshold is set comparing with no template control (H2O). On the right normalized copies per well. Standard deviations are relative to two independent biological replicates B) miR-130b-5p ddPCR on DDX58-tGFP, HA-SOD1 wt or co-expressing transfected HEK293T-cells. On the left representative droplets containing the amplified PCR product. Threshold is set comparing with no template control (H2O). On the right normalized copies per well; n=1.*

Using iPS-derived motor neuron progenitor (MNP) cells we provided further evidence that the two miRNA targets could be modulated according to the expression of DDX58 and SOD1. Differently from post-mitotic mature motor neurons, for MNPs we managed reach appreciable transfection efficiency. In Figure 3.24A, it is shown a representative

Western blot performed on input cells from which we extracted EV-RNA and performed cDNA synthesis. The EV-RNA analysis revealed a higher relative abundance of miR-1910-3p compared to miR-130b-5p upon normalization with Y3 Y-RNA as internal reference (Figure 3.24B). In addition, the co-expression of DDX58-tGFP and HA-SOD1 wt significantly decreased the secretion of miR-1910 compared to the single HA-SOD1 wt expressing cells. The variability in the case of miR-130b does not allow us to draw conclusions in this model. This notwithstanding, the use of MNPs gave us indications on

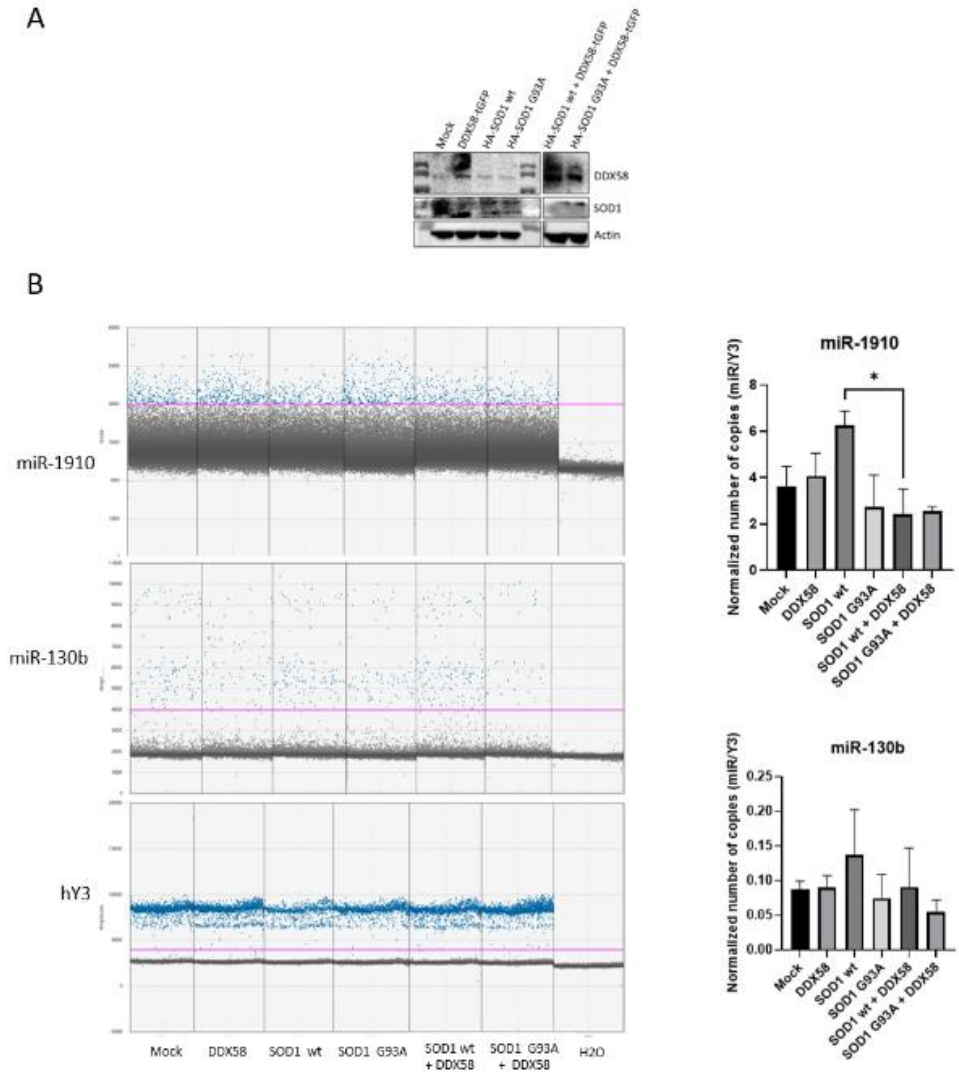

Figure 3.24 Digital droplet PCR miRNA assays in MNPs cells. *A) Western blotting showing DDX58-tGFP, HA-SOD1 wt/G93A or co-expressing transfection in motor neuron progenitors cells. B) miR-1910-3p and miR-130b-5p ddPCR on DDX58-tGFP, HA-SOD1 wt/G93A or co-expressing transfected motor neuron progenitors-derived EVs. On the left representative droplets containing the amplified PCR product. Threshold is set comparing with no template control (H2O). On the right normalized copies per well. Standard deviations are relative to two independent biological replicates. T-test *P-value <0.05*

how different cell models could cope differently with the overexpression of DDX58 and SOD1 in terms of secreted RNA.

In conclusion, we observed variability in the detection of DDX58-depending miRNAs although we report a promising trend for miR-130b-5p target. Differences from the expected outcome could be ascribable to the variable transfection, especially when compared to the sorted condition from the FACS-related RNA-Seq. Thereby, future testing and in silico analysis is required to understand the feasibility to use the tested miRNAs as DDX58/SOD1-associated sorting activity readout.

3.8.2 Functional tests explored as readouts of DDX58 upregulation

The hereby described DDX58 upregulation could play a role in the EV-RNA mediated activation of cell response, supporting in this context the ALS non-cell mediated autonomous hypothesis. For these reasons, we explored a series of functional assays and phenotypical associations to look for a possible function of EVs associated to DDX58 overexpression.

3.8.2.1 NF-κB activation

Since the activation of NF-κB is one of the downstream transcriptional cascades mediated by the activity of DDX58 during viral infection (Rehwinkel and Gack 2020), we set up an experiment to measure the activation of the pathway in response to EV-treatment exploiting a NF-κB luciferase reporter.

Briefly, we isolated EVs from HEK293T cells overexpressing DDX58-tGFP through ultracentrifugation and we used them to treat HEK293T expressing Firefly Luciferase under control of NF-κB responsive element. An acute treatment with the maximum amount obtained from the purification (40,000 EVs/cell) derived from DDX58-tGFP overexpressing cells, led to a 30% NF-κB activation increase compared to control (Figure 3.25A). Additionally, we tried to mimic a chronic exposure on receiving cells to the tested conditioned media using transwell co-colture assays. In brief, transwell cell culture

vessels equipped with a PET membrane with a cutoff of 0.4 μm that allows the passage of soluble material preventing cell migration. We transfected donor cells in the bottom with DDX58-tGFP and after medium change, we incubated them with receiving cells seeded in the upper part of the transwell. After 24h incubation, we retrieved the luciferase reporter from the cells in the upper part registering no significant variation on NF-κB activation in this set-up (Figure 3.25B).

Results indicate that an acute treatment with concentrated EV-containing preparations deriving from DDX58 overexpressing cells is necessary to boost the NF-κB dependent inflammatory response. We speculated that the different readout in the acute and "chronic" settings might be ascribable to a time-dependent rescued homeostasis. Otherwise, it is possible that the difference is due to a higher dosage of pro-inflammatory EVs in the acute treatment.

Although we provided only an indirect indication of a possible RNA-mediated post-transcriptional regulation on EV-receiving cells, we confirmed that the secretome from DDX58 overexpressing cells is able to influence the activation of NF-κB.

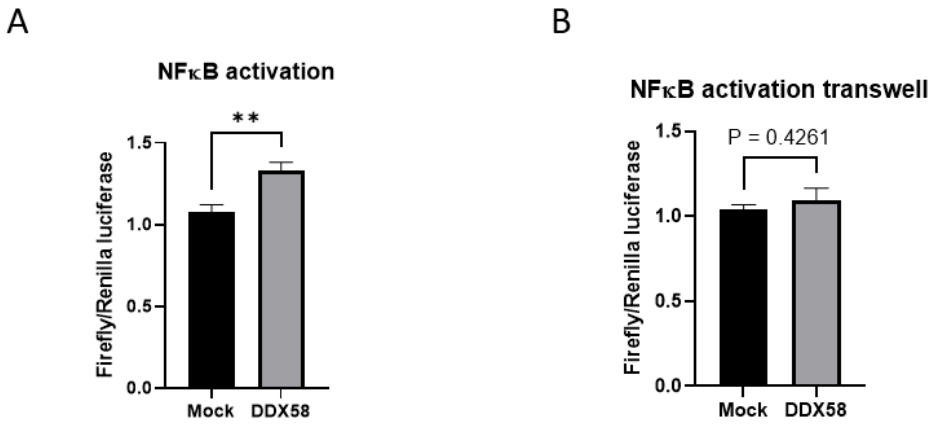

Figure 3.25 NF-κB activation upon DDX58-associated EV treatment. *A) NF-κB activation assay on HEK293T upon acute dUC-derived EVs treatment. Treatments were performed with EVs from Mock cells (Mock) or DDX58-tGFP (DDX58) overexpressing cells. Standard deviation is relative to three biological replicates. Mean ± SD; **P-value <0.01. B) NF-κB activation assay in HEK293T transwell co-colture to mimic "chronic" treatment for 24 h. Reporter cells were exposed to secretome of mock cells or DDX58-tGFP overexpressing cells (DDX58). Standard deviation is relative to two biological replicates. Mean ± SD. P value on graph.*

3.8.2.2 Senescence modeling in G93A fibroblasts unravels a new role of DDX58

During my secondment at Istitut de Recerca Biomedica de Lleida (IRBLleida), I had the opportunity to work with different ALS models. Of notice, since the group was studying senescence-associated secretory phenotype in ALS models, we decided to investigate a possible connection between the upregulation of Ddx58 and the occurrence of the senescent phenotype. We used mouse primary fibroblast isolated from SOD1 G93A ALS mouse model. Fibroblasts from symptomatic mice were isolated from the ear cartilage explants were cultured for 10 days (10DIV) to have non-senescent control cells. Meanwhile, the other experimental conditions were kept in culture with either DMSO or senolytic drugs in order to counteract cell senescence occurring in primary cells upon continuous cell passaging (details in material and methods section). The positivity of the model to β-galactosidase assay had previously been validated by our collaborators (data not known). Figure 3.26A shows the expression of p16, a well-known senescence marker, clearly increasing 10-fold upon cell passaging compared to 10DIV controls. In particular, we observed an enhanced susceptibility of G93A mouse-derived fibroblasts towards the treatment with quercetin and with the combination of Navitoclax and Dasatinib.

We tested the gene expression of Ddx58 in this setting and, strikingly, we noticed a similar increase in the expression in correlation with p16 fold change (Figure 3.26A). Conversely from p16 marker, we found senolytic treatments to efficiently diminish the expression of Ddx58 with no significant difference in susceptibility between the two groups of fibroblasts (CTL and G93A). Instead, there was significant increase in Ddx58 expression in senescent G93A compared to senescent control fibroblast. This data encouraged to dissect the role of Ddx58 mRNA expression in promoting cell senescence in vitro.

The previous experiment had the limitation of using 0.5% DMSO as control condition. Low doses of DMSO in cell culture were shown to interfere with many biological processes (Tunçer et al. 2018) and especially long-term presence could widely affect RNA transcription (Verheijen et al. 2019). For these reasons, we decided to repeat the experiment without senolytics treatment and so without adding DMSO to the medium. We also used mY3 Y-RNA as normalizer, due to its stable cytosolic localization and relative abundance (Driedonks et al. 2020), instead of Actb, whose expression is affected during senescence for the phenotypic cytoskeleton rearrangement (Guan, Crasta, and

Maier 2022). The result is shown in Figure 3.26B: the upregulation of p16 was confirmed, though a fold change of 6-7.5 was obtained against the non-senescent controls compared to 10-12-fold of the previous experiment. We observed a 20% increase of Ddx58 expression in the control senescent fibroblasts and 45% increase in the G93A senescent fibroblasts, supporting the fact that DDX58 might be transcriptionally activated in a context of cell senescence.

A future perspective in this sense would foresee the isolation of EVs from the senescent model with the aim to identify a functional RNA target associated to vesicles in response to the senescence phenotype. In general, we report that Ddx58 could play a role in the process of cellular senescence as suggested by the upregulation of Ddx58-encoding mRNA.

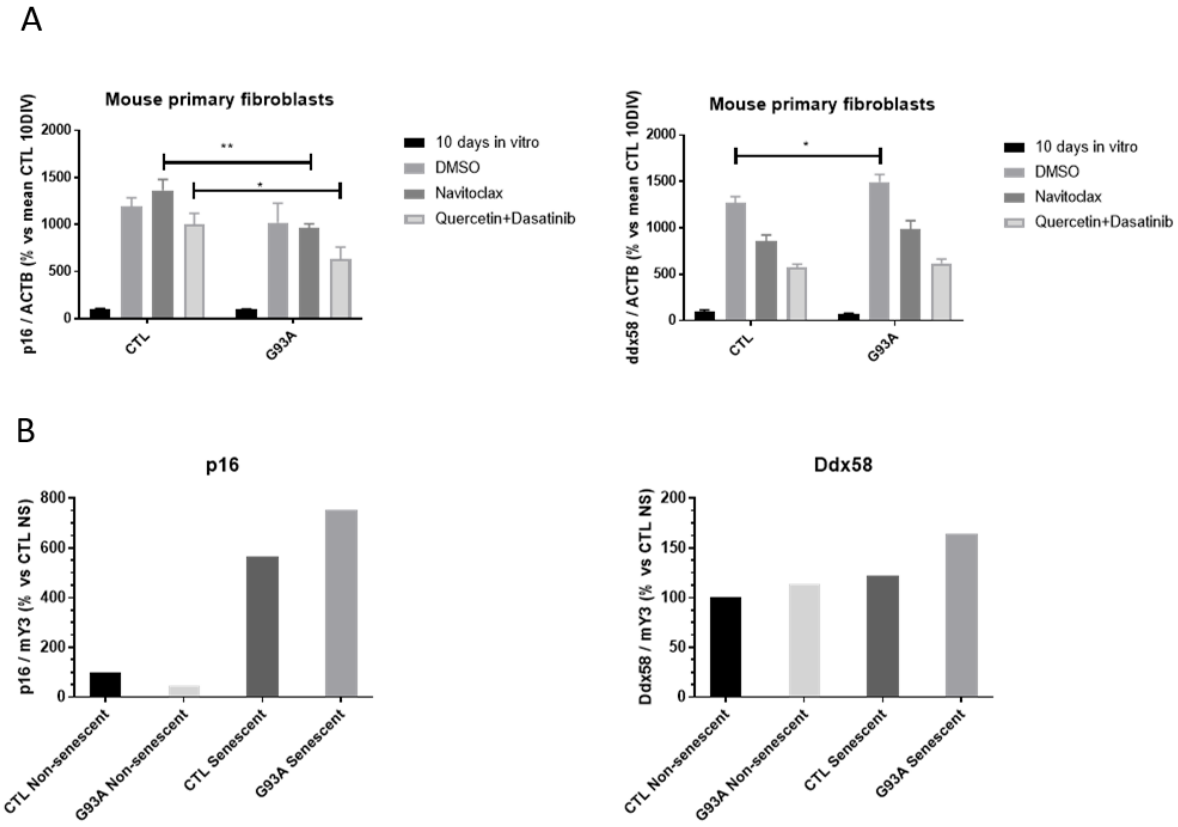

Figure 3.26 Ddx58 is involved in cell senescence. *A) qRT-PCR on senolytics treated fibroblasts shows mRNA expression normalized by ΔΔCt method over Actb expression respectively of: p16 on the left; Ddx58 on the right. Standard deviation represents three independent biological replicates. Mean ± SD; two-way ANOVA * P-value <0.05; **P-value <0.01 B) qRT-PCR on untreated fibroblasts shows mRNA expression normalized by ΔΔCt method over mY3 expression respectively of: p16 on the left; Ddx58 on the right. Graphs are representative of a single experiment.*

3.8.2.3 ATP levels upon astrocytes-NSC34 cell-to-cell communication

From the transcriptomic analysis, we proposed that EVs secreted from astrocytes in the presence of SOD1 G93A mutation could have role on metabolic process related targets. We then set up an experiment testing the communication between astrocytes harboring the mutation and DDX58-tGFP transfected NSC34 cells. For this purpose, neonatal astrocytes were plated in the lower chamber of a transwell-containing cell culture vessel and transfected NSC34 were placed on the top. After incubation with astrocytes' secretome, we exploited CellTiter-Glo® reagent to measure ATP content in NSC34. In this assay, a luciferase signal is generated upon specific recognition of the tri-phosphorylated form of the nucleotide substrate. As we expected, the feeder layer of astrocytes was able to increase the viability of NSC34 compared to non-incubated transwell controls independently from the mutation (Figure 3.27A). Interestingly, the overexpression of DDX58 decreased the ATP boost upon exposure to astrocyte media and the effect was significantly exacerbated in the presence of mutant astrocytes. We can only speculate that the DDX58-overexpressing NSC34 might be more susceptible than mock to the pro-inflammatory environment dependent on the SOD1 mutation. This is in line with described cell specific vulnerability to ALS astrocytes toxicity, demonstrated for human motor neurons (Song et al. 2016), that could parallel the intracellular miRNAs rearranged upon DDX58 overexpression.

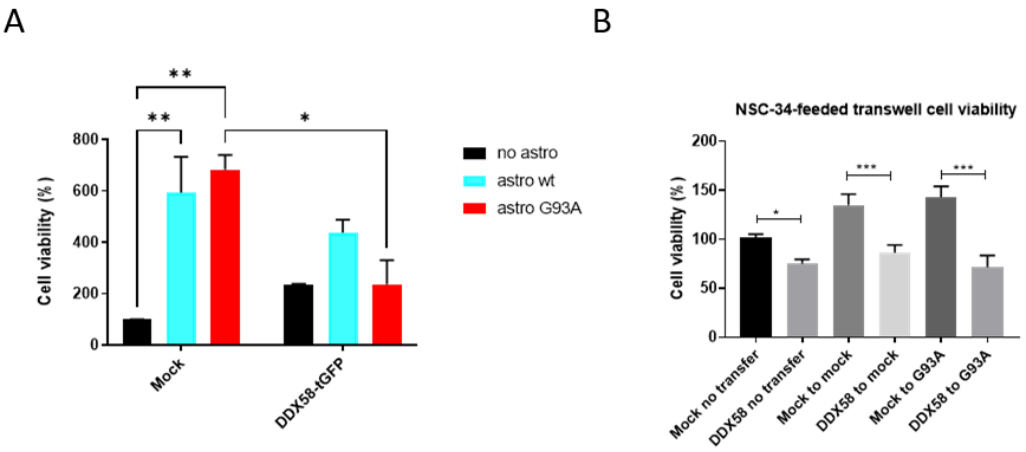

Figure 3.27 Transwell co-colture of astrocytes and DDX58-overexpressing NSC34. *A) % of viability of mock or DDX58 overexpressing NSC34 cells exposed to the secretome of WT or SOD1 G93A astrocytes. Standard deviations are relative to two biological replicates. Mean ± SD; two-way ANOVA * P-value <0.05; **P-value <0.01 B) % of viability of mock or DDX58 overexpressing NSC34 cells exposed to the secretome of NSC34 mock or overexpressing HA-SOD1 G93A. Standard deviations are relative to two biological replicates. Mean ± SD t-test * P-value <0.05; **P-value <0.01; ***P-value <0.001*

Nevertheless, it is to be considered that DDX58 is an ATP consuming enzyme that upon ATP hydrolysis is able to translocate along dsRNA and increase the turnover of the substrate (Lässig et al. 2015). Therefore, we do not exclude a possible interference with the signal mediated by the ATPase activity of the protein.

In parallel, we performed a negative control experiment plating NSC34 instead of astrocytes and we saw no effect on proliferation driven by the homologous exchange of secretome (Figure 3.27B). This supported the fact that indeed NSC34 mouse motor neuron-like cell line react to astrocytes in a cell line dependent manner.

To have an indication of a possible DDX58-dependent transfer of RNA towards receiving astrocytes, we challenged the detection of intracellular miRNA targets in the astrocytes from the same experimental settings. After ATP testing, we isolated RNA from astrocytes previously incubated with NSC34 and performed ddPCR. In a single explorative experiment, we reported a variable intracellular abundance of tGFP positive EV-upregulated mmu-miR-709 in the mutant astrocytes exposed to NSC34 cells (Figure 3.28A). Another target, mmu-miR-130b-3p, resulted from the sequencing to be downregulated in the same EV-samples, was found downregulated in wt astrocytes exposed to DDX58 expressing cells rather than to the mock control (Figure 3.28B).

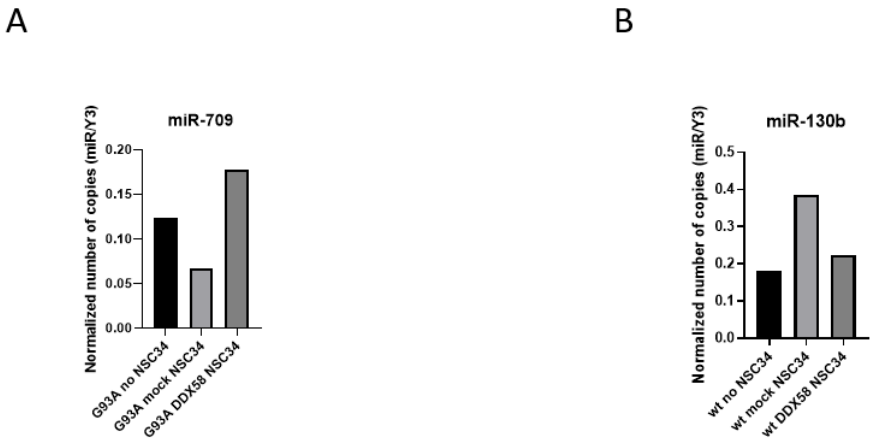

Figure 3.28 Astrocytes intracellular miRNAs expression. *A) ddPCR of mmu-miR-709 on SOD1 G93A astrocytes co-coltured with DDX58-transfected NSC34. B) ddPCR of mmu-miR-130b-5p on SOD1 wt astrocytes co-coltured with DDX58-transfected NSC34. n=1*

Indirectly, this single experiment only indicates the alteration of miRNA expression in astrocytes cells exposed to NSC34 secretome, thereby inferring a crosstalk between the two. Additional approaches would be necessary to assess whether the miRNA

fluctuations are due to an EV-mediated transfer or to a cell-autonomous transcriptional response.

To strengthen and generalize the mechanism, thanks to the mouse model kindly provided by Prof. Manuela Basso (CIBIO), we exploited the same transwell co-culture procedure with neonatal astrocytes that harbor TDP-43 Q331K mutation. We exposed NSC34 cells to the secretome of both wt and mutant astrocytes and we retrieved the same result observed with SOD1 G93A model, hence a reduced viability of DDX58-tGFP overexpressing cells in the presence of mutant astrocytes secretome compared to wt (Figure 3.29).

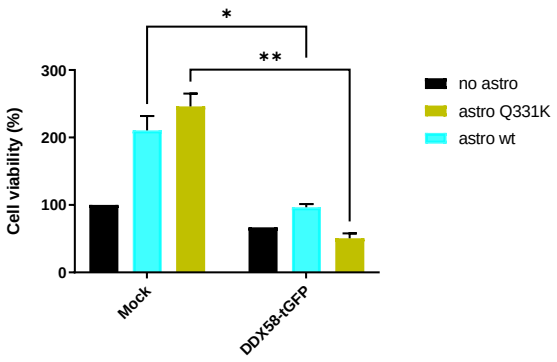

Figure 3.29 Transwell co-colture of TDP-43 astrocytes and DDX58-overexpressing NSC34. *% of viability of mock or DDX58 overexpressing NSC34 cells exposed to the secretome of WT or SOD1 G93A astrocytes. Standard deviations are relative to two biological replicates. Mean ± SD; two-way ANOVA *P-value <0.05; **P-value <0.01*

In summary, the ATP levels in DDX58 overexpressing NSC34 are significantly decreased upon exposure to mutant SOD1 and TDP-43 astrocytes and this could potentially be correlated to an active crosstalk between the two cell lines.

3.9 Exploring DDX58 as a functional target of TDP-43

In parallel to the investigation on DDX58 linkage to SOD1 ALS model, we explored a possible link between DDX58 and TDP-43. Indeed, the two proteins have already been reported in the literature to be functionally related (Dunker et al. 2021; Macnair et al. 2016). Specifically, Ddx58 was found upregulated in TDP-43 mutant mouse motor neurons and the corresponding Ddx58-encoding mRNA was described as a target RNA

bound to Tdp-43 (Macnair et al. 2016). Also, a depletion of TDP-43 was demonstrated to activate DDX58 via the recognition of aberrant species of ncRNA (Dunker et al. 2021). To address DDX58 and TDP-43 mutual intracellular localization, we overexpressed the two proteins in NSC34. After ectopic expression of GFP-tagged TDP-43 (full length and aggregation-prone fragment) and Ddx58 staining we did not find any overlap in signal. A similar distribution was obtained by co-transfecting DDX58-tGFP with the wt or Q331K mutant TDP-43 (Figure 3.30). This confirmed the reported indirect association of the two proteins (Macnair et al. 2016).

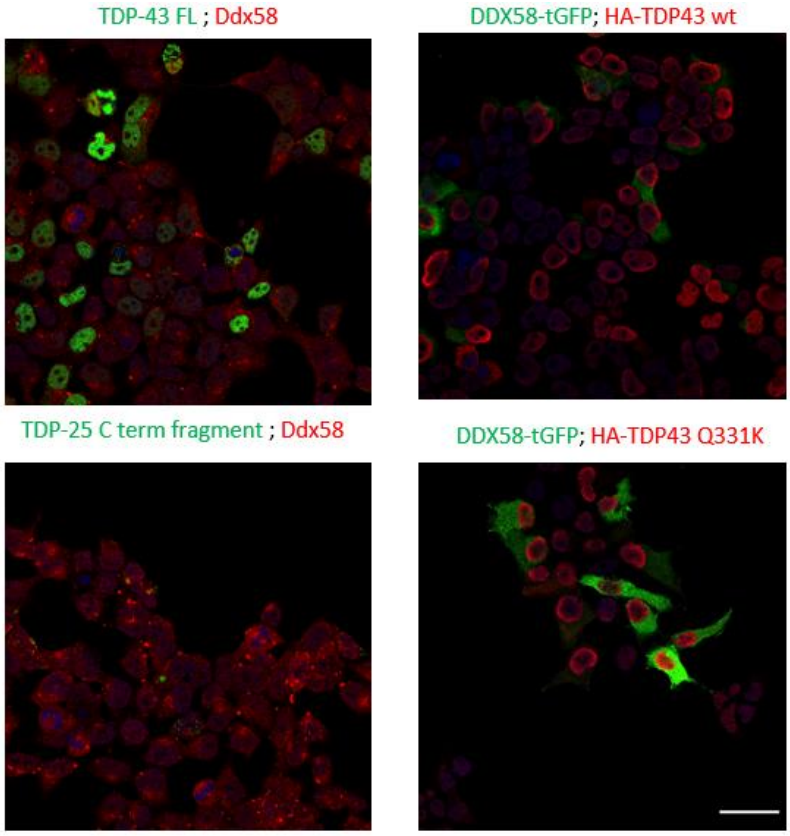

Figure 3.30 DDX58 and TDP-43 intracellular distribution in NSC34. *Representative confocal images. Top left: GFP-TDP-43 full length (in green), Ddx58 (in red) stained using Invitrogen primary antibody, nuclei (in blue); Bottom left: GFP-TDP-25 C-terminus fragment (in green), Ddx58 (in red) stained using Invitrogen primary antibody, nuclei (in blue); Top right: DDX58-tGFP (in green), HA-TDP-43 wt (in red), nuclei (in blue); Bottom right: DDX58-tGFP (in green), HA-TDP-43 Q331K (in red), nuclei (in blue). 63X magnification, Scale bar: 30 µm.*

To address a possible indirect association of DDX58-dependent RNA with TDP-43, we exploited the pulldown approach described in 3.5. Briefly, we subjected HEK293T endogenous TDP-43 to EV-RNA-mediated pulldown both in steady-state and in DDX58-

tGFP lysates. We observed a trend of enriched pulldown of TDP-43 upon incubation of both lysates with the EV-RNA bait derived from DDX58 and SOD1 co-expressing cells (Figure 3.31). The densitometry highlighted a slight increase in lysates overexpressing DDX58 rather than control, although not significant (P=0.0773).

This data supported the fact that vesicular RNA, indirectly affected by DDX58-SOD1 co-expression, could be preferentially recognized by endogenous TDP-43 that, in this approach acts as a positive control.

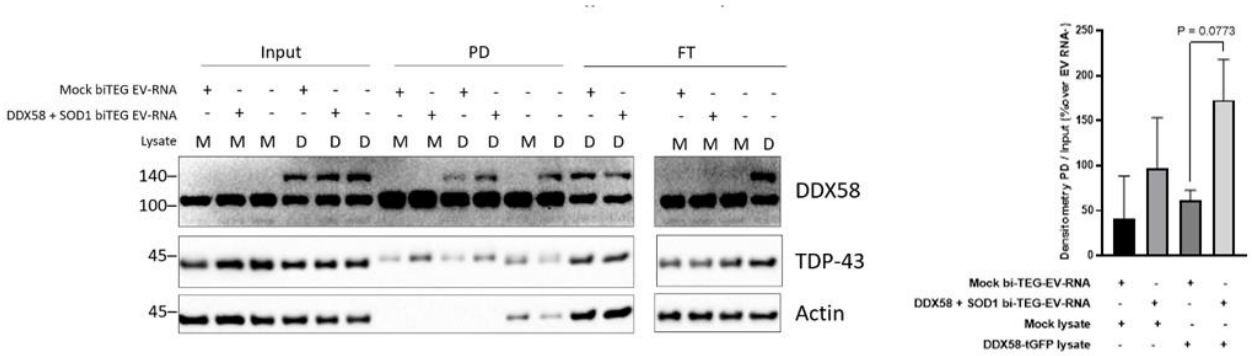

Figure 3.31 Biotinylated EV-RNA endogenous TDP-43 pull down. *On the left: Western blotting on mock (M), DDX58-tGFP (D) and HA-SOD1 wt (S) lysates. PD=pull down; FT=flow-through. On the right: densitometric analysis relative to two independent biological replicates. T-test P-value on graph*

For further validation of this connection, we tried to mimic the reported TDP-43-depletion and correlated DDX58 upregulation. We exploited a HeLa cell model kindly provided by Prof. Manuel Portero (IRBLleida). These cells were stably expressing a TARBP-directed shRNA under a TET-ON inducible cassette (HeLa iTDP43). By transfecting HeLa iTDP43 with DDX58-tGFP, we noticed a stabilized ectopic DDX58 expression upon a doxycycline treatment able to knock-down 80% of TDP-43 protein (Figure 3.32A). We isolated total cellular (and in a single experiment also vesicular) RNA from the cell line in the same experimental setting and performed a quantification of DDX58-encoding transcript via qRT-PCR. Data is shown in Figure 3.32B normalized against hY3 Y-RNA, an abundant EV-associated transcript (Driedonks et al. 2020). Interestingly, we reported a concordant increase in the fold change of DDX58 mRNA upon TDP-43 silencing. Besides, we reported an opposite trend for the ectopic mRNA in the vesicles, supporting a reduction in the secretion of this transcript in the lack of TDP-43 expression (Figure 3.32C).

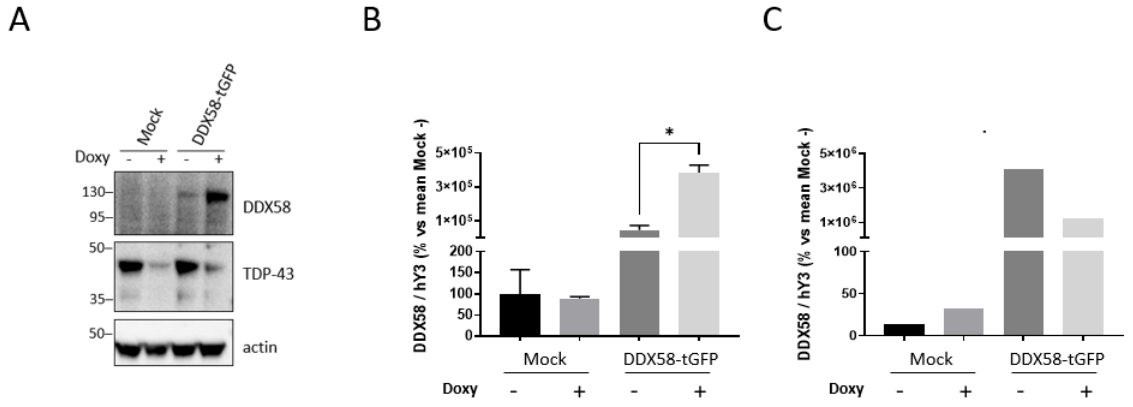

Figure 3.32 HeLa iTDP-43 cell line: inducible TDP-43 silencing increases DDX58. *A) Representative Western blotting of DDX58-transfected HeLa iTDP-43 cells upon 200 µg/µL doxycycline (Doxy) addition for 72 h. B) DDX58 mRNA expression at the intracellular level normalized by ΔΔCt method over hY3 Y-RNA expression. Standard deviation represents two independent biological replicates. Mean ± SD; t-test * P-value <0.05. C) DDX58 mRNA expression at the EVs level normalized by ΔΔCt method over hY3 Y-RNA expression. This experiment was performed on EVs deriving from only one of the two replicates shown in B.*

Similarly, we used iPS-differentiated human motor neurons as one of the most relevant human cellular models. In particular, during the period abroad, we were able to differentiate one population of iPSCs deriving from a healthy control (CTL) and another one deriving from a fALS SOD1 H44R mutation. We transfected transiently the mature motor neurons with siRNA to knock down TDP-43 expression. Notably, we obtained a 60% TDP-43 knock-down level for CTL motor neurons and 85% TDP-43 knock-down level for SOD1 H44R motor neurons. In this context, we measured the levels of DDX58-encoding mRNA and retrieved a 4-fold increase in case of TDP-43 silenced CTL motor neurons (Figure 3.33A). Despite the higher knock-down level, DDX58 expression was not upregulated in silenced mutant SOD1 motor neurons (Figure 3.33B). This was indicative of either a dose-dependent effect or a mutant specific differential phenotype which we could not exclude with our data.

From these two preparations of mature motor neurons, we extracted EVs via NBI and assayed via ddPCR the relative content of hsa-miR-1910-5p and hsa-miR-130b, targets resulted from the NGS associated to tGFP positive cell-derived EVs and respectively up- and down-regulated upon DDX58 overexpression. For miR-1910-3p we did not observe differential secretion in motor neurons derived from healthy controls in the presence of

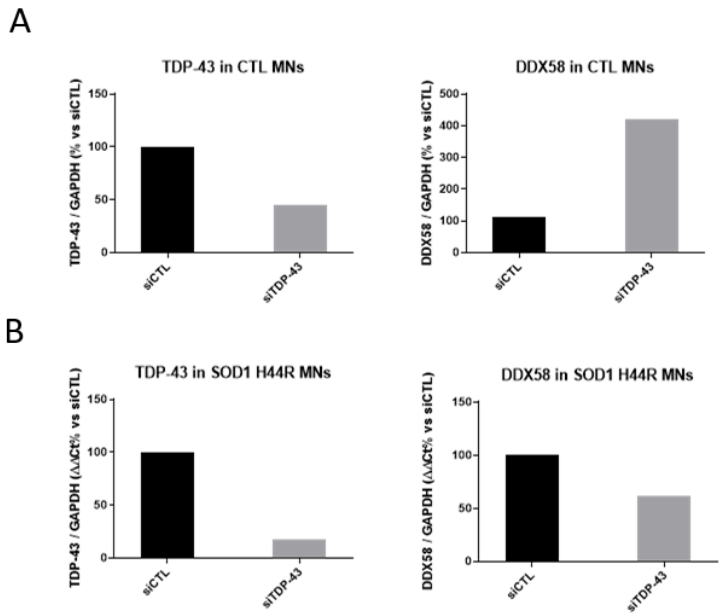

Figure 3.33 Mature iPS-differentiated motor neurons silenced by siTDP-43 transfection. *A) Healthy control (CTL)-derived motor neurons. Intracellular mRNA expression normalized by ΔΔCt method over GAPDH expression respectively of: TDP-43 on the left; DDX58 on the right. Data show n=1 biological replicate B) SOD1 H44R-derived motor neurons. Intracellular mRNA expression normalized by ΔΔCt method over GAPDH expression respectively of: TDP-43 on the left; DDX58 on the right. Data show n=1 biological replicate.*

TDP-43 silencing nor for mutant SOD1 motor neurons-derived EVs (Figure 3.34). This was in line with the variability already observed in the validation of this target in HEK293T and MNP cells. Conversely, for the miRNA downregulated upon DDX58 expression, we found a correlation between the levels of miR-130b-5p and the silencing of TDP-43 and consequent DDX58 upregulation in donor cells (Figure 3.34). The trend was consistent in both control and SOD1 H44R EVs, with a reduction upon silencing directly correlated to the knock-down levels of the protein.

These data provide a stand-alone basis for future analyses to be performed on TDP-43-mediated upregulation of DDX58, especially in experimental settings recapitulating the ALS-associated TDP-43 loss of function.

Nevertheless, we proposed a confirmation that the silencing of TDP-43 could generate an upregulation or a parallel alteration in the quality of EV-RNA.

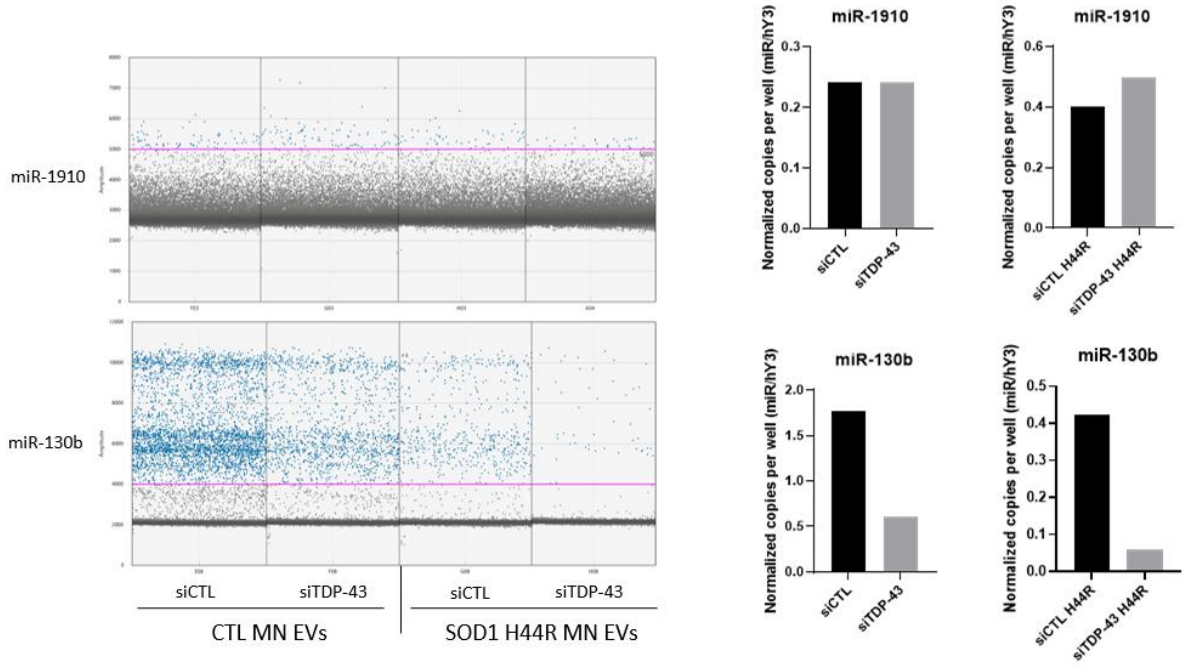

Figure 3.34 Digital Droplet PCR on EVs from iPS-derived mature motor neurons. *On the top miR-1910 assay: droplets containing the amplified PCR product. On the right normalized copies per well (hY3 Y-RNA not shown). On the bottom miR-130b assay: droplets containing the amplified PCR product. On the right normalized copies per well (hY3 Y-RNA not shown). CTL=healthy control-derived motor neurons; H44R=SOD1 H44R-derived motor neurons. Graphs are relative to n=1 biological replicate.*

4. DISCUSSION

Biomarker discovery is needed in ALS to systematically address the disease progression mechanisms. RNA-binding proteins have been demonstrated to play a pivotal role in the active selection of RNA species for extracellular secretion (Fabbiano et al. 2020). The present work aimed at studying the extracellular vesicles microRNA content upon the ectopic expression of an ALS emerging RBP, i.e. DDX58.

Mostly referred to as RIG-I, DDX58 is a member of the pattern recognition receptors (PRRs) in the field of innate immunity against RNA viruses. Nevertheless, very recently, it has been associated with ALS in both SOD1 and TDP-43 models (Kudo et al. 2010; Macnair et al. 2016). Interestingly, non-canonical functions described in the literature associated DDX58 to novel biological processes, besides inflammation (Xu et al. 2018). With these premises, the aberrant metabolism of RNA occurring in ALS allowed us to envision the involvement of such conserved RNA sensor as a hub activated in damaged cells. Indeed, Dunker et al demonstrated an activation of DDX58 upon TDP-43 depletion and aberrant non-coding RNA recognition (Dunker et al. 2021).

As an explorative approach, we exploited NSC34 motor-neuron like cells transiently expressing a recombinant human DDX58 with a tGFP reporter. We point out that we attempted to knock-down Ddx58 expression, with unsuccessful results, exploring different strategies. We used commercially available siRNAs and shRNAs with insufficient silencing yields. We tried also lentiviral particles packaged with shRNA-encoding plasmid and the transduction did not work either. We thought of the need to optimize the procedure while dealing with a transcript with low basal levels. To our knowledge, similar approaches employed on NSC34 cells as well resulted in neglectable silencing in the absence of a virus-mediated Ddx58 upregulation (Bhaskar, Mukherjee, and Basu 2021). An intervention through CRISPR-Cas9 was tried, but in our hands it required further optimization, hence we decided to focus on the description DDX58 overexpressing condition.

Additionally, we decided to transiently express the DDX58-tGFP instead of establishing a stable clone. The choice was entirely data-driven: in fact, we demonstrated a time-

dependent relocation of the intracellular distribution of the protein and, especially, a differential time-dependent vesicular RNA secretion. Regarding the subcellular distribution, we confirmed the cytosolic localization of the ectopic protein. Indeed, an active translation of DDX58 upon viral infection is associated with similar distribution, as it engages cytosolic complexes with adaptor proteins of the innate immune response (Sánchez-Aparicio et al. 2017). In its inactive conformational state, the protein's helicase intermediate domain is in contact with the effectors CARD domains and, as such, localizes in the cytosol and in microsomes, ER derived vesicular fractions in communication with other organelles (Esser-Nobis, Hatfield, and Gale 2020). This is in line with what we found looking at the endogenous DDX58 distribution in HEK293T cells and with organelles in the confocal imaging.

We described the secretion of DDX58 protein as cargo of extracellular vesicles. From the literature, we knew that DDX58 had previously been linked to SQSTM1-mediated selective autophagy (Xian et al. 2020). Also, DDX58 activation upon RNA recognition was shown to trigger autophagy and promote the cleavage of LC3 (Lee et al. 2018), an autophagosome marker strictly involved in RNA-binding protein secretion through EVs (Leidal et al. 2020).

Here, the identification of DDX58 in EVs and in low density fractions suggested an involvement of RLRs as damage associated molecular patterns (DAMP) factors secreted in the extracellular milieu in vitro, in agreement with the OptiPrep^{TM} density gradient isolation and the Nanoparticle Tracking Analysis.

We observed that DDX58-affected EV-RNA secretion appeared to be associated with acute overexpression of the protein.

Exploiting a FACS-Seq approach, we described that few transcripts are differentially secreted from sorted cells. This was extremely surprising considering the diversity of the conditions in terms of DDX58 expression levels. Among DDX58-associated DEGs we highlight miR-203. This miRNA was already described to target 14-3-3θ, a regulatory protein that controls NF-κB activation, generating neuroinflammation, microglia activation, neuronal death and cognitive functions impairment (Li et al. 2022). Also, the degradation of 14-3-3θ mRNA induced upon unfolded protein response and regulated

IRE1α-dependent decay (RIDD) results in neuronal death, further remarking the neuroprotective role of 14-3-3θ protein (Gómora-García et al. 2021). Similarly another miRNA, miR-130b-5p, a downregulated miRNA in EVs from tGFP-positive cells, was found to be anti-inflammatory against microglia activation in spinal cord injury (D. Wang et al. 2021).

Despite the low variability in the secreted miRNA content, for intracellular miRNAs we report a clustered list of transcripts differentially expressed in the cells in the presence of DDX58-tGFP. This is a further proof of the role of the protein in controlling gene expression based on cell abundance: nevertheless, we did not check whether this effect is mediated by a direct post-transcriptional control of DDX58 rather than an indirect alteration due to the transfection itself or to the transcriptional activation DDX58-induced phenotypes.

There is no evidence reporting DDX58 and SOD1 as interacting partners, as far as we know. Notwithstanding, the proteins were functionally connected to neurodegeneration as Ddx58 was found as early marker of neuronal death in Sod1 motor neuron dysfunction and tauopathy mouse models (Kudo et al. 2010). Also, very recently, a proteomic analysis identified RIG-I-like receptors among the abundant proteins expressed in the spinal cord of symptomatic SOD1 G93A mice (L. Chen et al. 2023)

We described a mutual redistribution of DDX58 and SOD1 between larger or smaller secreted particles. We do not provide an exclusion study supporting the presence of a DDX58-SOD1 protein complex in the lumen nor on the surface of EVs. Although, we show that intracellularly the proteins share a common distribution and might physically interact as reported in the immunoprecipitation experiments in paragraph 3.4. Specifically, we retrieve Ddx58 protein using anti-SOD1 antibody: we report an interesting shift in molecular weight that is compatible with what observed in the nuclear fraction of HEK293T cell fractionation. It is possible that SOD1 protein preferentially interact with a post-translationally modified DDX58 or an isoform of the protein. The fact that we never observed SOD1 protein in the anti-DDX58 immunoprecipitated samples prevents us to propose a biochemical interaction model. Sod1 absence in anti-DDX58 IP could be due to many reasons: e.g., epitope at the

interaction surface, specificity of different antibodies for the complexes, SOD1 supramolecular structures.

We found not only that the overexpression of human SOD1 G93A increases the trend of EV-RNA secretion, but the co-transfection with DDX58-tGFP further exacerbates this phenomenon. The experiments of pull down of the biotinylated EV-RNA population gave us an indication that the functional DDX58-tGFP protein is also able to recognize preferentially sequences deriving from co-expressing cells. Although encouraging, the presence of the endogenous protein in the negative controls does not allow us to generalize the specificity of the method. We can only speculate that the increasing EV-RNA loading could be aided by the recognition of RNA by DDX58.

To expand our model, we had the opportunity to use SOD1 G93A mutant mice-derived specimens, harvested by our collaborators in Genova. SOD1 mice are one of the most characterized ALS model and they harbor mutations in the first identified fALS gene Interestingly, they also recapitulate most of the motor and cognitive dysfunctions present in the human disease (Alrafiah 2018). We extensively characterized at the biophysical level EVs released by SOD1 primary astrocytes. Assessing the EV-RNA content, we noticed that mutant astrocytes were able to secrete an increase amount of total RNA compared to wt littermates. The reported G93A upregulated miRNAs secretion is in concordance with a recent work describing the role of mutant SOD1 in modulating miRNA biogenesis, from the nuclear export to the maturation of the transcript, upon interaction with exportin-5 (X. Chen et al. 2022).

With our NGS pipeline, we reported a putative role of the modelled glial cells in controlling gene expression in CNS through the secretion of EVs. The contribution of the ALS-mutation was remarkable as highlighted by the abundance of upregulated miRNAs in SOD1 G93A EVs. Furthermore, we could predict upon gene set enrichment analysis that the regulated targets are involved in biological processes important for the disease such as axonal growth, neurotrophin signaling and biological processes related to metabolism, macromolecule biogenesis and response to chemical stimuli. With these indications, we support the description of a non-cell autonomous, EV-RNA-mediated phenotype in SOD1 ALS.

Beyond that, by comparing common targets from mutant astrocytes-derived EV-transcriptomes, we retrieved Atxn1 a well-known transcriptional regulator involved in neurodegeneration, controlling Notch signaling and bioenergetics in spinocerebellar ataxia and other neurodegenerative diseases (Sánchez, Balagué, and Matilla-Dueñas 2016). Remarkably, a transcriptomic analysis carried out on a SCA2 mice harboring an intermediate polyQ expansion mutation on Atxn2 (paralogue of Atxn1) correlated SCA to ALS in terms of mRNA expression profiles in spinal cords. Interestingly for us, the authors reported and validated also the upregulation of Ddx58 gene in the ataxin loss-of-function mice (Scoles et al. 2020). This supports the connection between the SOD1 induced RNA changes in astrocytes and the response mediated by DDX58.

The analysis of DEGs present in EVs from DDX58/mutant SOD1 co-transfected NSC34 cells and tGFP-positive sorted cells revealed a higher abundance of differential transcripts rather than the other possible comparisons among the datasets. Interestingly, we highlight miR-423-3p upregulated in EVs in the presence of the mutation compared to EVs from DDX58-only expressing cells. The same miRNA was identified significantly downregulated in sera of ALS patients in the earliest stage compared to healthy control and to more severe stages (Dobrowolny et al. 2021). This supports a possible role in the early activation of DDX58-SOD1 axis in the progression of the disease. Additionally, we reported mmu-miR-542-3p as significatively differential miRNA between the EV-transcriptomes deriving from co-transfected cells. This miRNA was found downregulated in the vesicles upon G93A mutation. This miRNA presents two experimentally validated targets on miRTarBase: the E3 ubiquitin ligase TrimL1, belonging to the same family of Trim25 (known RIG-I activator) (Ozato et al. 2008) and Trpm2, a cation channel abundant in the CNS and involve in oxidative-stress induced neuronal death (Belrose and Jackson 2018).

A final comparison of the cellular transcriptomes of G93A astrocytes and DDX58-positive NSC34 revealed, among the common mRNAs target, a gene associated to ALS by Phenopedia database (Yu et al. 2010), i.e. Serpine1 . This gene encodes for Plasminogen activator inhibitor type 1 (PAI-I) an extracellular inhibitor of tissue type plasminogen activator. PAI-I is secreted by glial cells and affects microglia migration (Jeon et al. 2012).

Thereby, a downregulation (shared between G93A astrocytes and DDX58 overexpressing cells) of Serpine1 could possibly hint at neuroinflammation.

We started to test some targets via miRNA-enriched TaqMan ddPCR assays and we found out that the simple overexpression of DDX58-tGFP in HEK293T cells is not sufficient to increase the secretion of miR-1910-3p. On the contrary, the trend of downregulated miR-130b resulted to be promising in TDP-43-silenced motor neurons.

Indeed, regarding this point, we provided further indications that DDX58-encoding mRNA is a target of TDP-43 RNA-binding activity. In particular, we exploited doxycycline-inducible TARDBP silenced HeLa cells and noticed an increased in DDX58-tGFP protein and mRNA abundance upon TDP-43 depletion. Moreover, we reported a similar trend in intracellular mRNA levels in control human differentiated motor neurons. The same trend was not observed using differentiated SOD1 H44R mutant motor neurons.

In the attempt to identify a DDX58-dependent paracrine effect on receiving cells, many possibilities were explored. The activation of NF-κB upon acute treatment of reporter cells with UC-derived EVs was assessed: as we expected, we retrieve an activation of NF-κB after treating with DDX58-tGFP EVs. The limitation of this approach relies on the presence, as we showed, of mixed subpopulation of vesicular and non-vesicular particles in UC pellets, thus it is not possible to speculate about post-transcriptional events upon treatment.

Given the importance of secretory pathway in the cellular process of senescence, we made use of a model of proliferation-induced senescence in primary fibroblasts from SOD1 mice to address a possible DDX58-associated phenotype. Upon qRT-PCR setting, we retrieved not only the abundance of Ddx58 transcript in senescent cells but also an unprecedented modulation of the protein expression via senolytic drugs. The involvement in senescence of inflammation, innate immunity and interferon stimulated gene activation is not surprising (F. Liu et al. 2011) and DDX58 specifically associates to the recognition of accumulating dsRNAs in aging cells (Mullani et al. 2021). From these experiments we could envision a possible involvement of DDX58-associated EV-RNA modulation to senescence-associate secretory phenotype, a horizon to be explored in future investigations.

In addition, we developed an approach exploiting transwell co-cultures to assess the intercellular communication between astrocytes and NSC34 cells. Non-transfected NSC34 significantly enhanced their proliferative status when compared to controls not exposed to astrocytes secretome. The reduced signal observed when DDX58-expressing cells were exposed to G93A mutant astrocytes (as well as to TDP-43 Q331K cells) could be due to a technical matter, being DDX58 an ATP-hydrolyzing enzyme. We speculate that DDX58 upregulation could cause a post-transcriptional gene regulation in receiving glial cells that in turn might respond generating a pro-inflammatory environment affecting NSC34 cells. This model, although stimulating, can only be postulated from the data, as the main indication remains the interconnection of these two cell lines through their secretome.

Summarizing, in this work, we explored the involvement of DDX58 in the co-regulation of ALS EV-associated transcripts. The investigational nature of the present work put the basis for the study of novel functions of DDX58 associated to EV biology and stresses the relevance of RNA-dependent inflammatory response in SOD1 and TDP-43 ALS models.

5. FUTURE PERSPECTIVES

In this thesis, we explored a novel role for DDX58, associated with EVs and EV-RNA. The novelty is not relying on the simple identification of a vesicular route of secretion of the protein, indeed, the overexpression of such antiviral RNA sensor resulted in increased packaging of EV-RNA. Although, a limitation is that the data reported in the present thesis manuscript that are lacking proper number of biological replicates should be further repeated in order to validate the results and obtain appropriate significance. Additionally, extensive study is required to elucidate the extent and the implications of these findings at many levels.

Short-term perspectives

Up to now, we only have few indications in the literature associated DDX58 with miRNA direct binding. A validation of a DDX58-dependent target (confirmed upon endogenous protein depletion) would allow the usage of an RNA sequence in a directed pull down or RIP approach. As reported in the introduction indeed DDX proteins have been associated with low RNA processivity compared to other RNA helicases (Bourgeois, Mortreux, and Auboeuf 2016), supporting a direct miRNA binding.

Besides miRNA, we have recent evidence that DDX58 could endogenously interact with messenger RNAs and particularly regulating the 3'UTR regions of inflammation-related mRNAs such as interleukin receptors or NF-κB-associated transcripts (Eitan et al. 2022)(Zhang et al. 2013). We are currently working to optimize RNA immunoprecipitation of endogenous and ectopic DDX58 in order to confirm a possible dosage-dependent association with miRNA and mRNA transcripts.

If confirmed, together with the shown results of the study, this would imply that DDX58 might co-regulate inflammation at various levels, supporting our model of a paracrine involvement of the protein in ALS progression.

Mid-term perspectives

We showed an upregulated EV-RNA secretion and analysed with a transcriptome-wide approach just the miRNA content, with the aim to describe RNA species that could have a post-transcriptional control on receiving cells and biomarker potential. Although we still do not know the significance nor the specificity of such upregulation upon DDX58 modulation. It would be of utmost importance to understand the effective presence of miRNA (and perhaps pri-miRNA fragments?) in secreted vesicles upon DDX58 knock-out. The selection of a stable CRISPR-Cas9 DDX58-depleted clone in NSC34 (or in HEK293T) could allow us to challenge the specificity of identified miRNAs. We might consider assessing other targets resulted to be significant from the comprehensive NGS analysis. A full characterization of the RNA species sequenced (including other ncRNA species as well as sense coding mRNAs) is still ongoing upon deepened analysis.

Also, given the little impact of DDX58 presence alone in the massive secretion of miRNA in EVs, we might argue that different NGS cDNA library preparation pipeline could be employed to study the contribution of other ncRNAs as well as longer mRNA transcripts differentially abundant in the vesicles.

Regarding the ALS-link, we hereby reported a first indication of a co-dependent secretion of DDX58 and SOD1. The two proteins might associate locally in the cell and future approaches of super resolution imaging could be applied in this case, to elucidate possible similarities in co-localization along with Rab proteins member to effectively evaluate their vesicular biogenesis. We would consider deepening the functional correlation between TDP-43 silencing and DDX58-associated changes in RNA expression. In this context, outside of the framework of the present thesis, we emphasize a proteomic analysis performed in our lab from TDP-43 overexpressing NSC34. Here, EV-RNA was used as probe for pulldown-MS and almost 1% of the differently abundant proteins were DDX proteins: strikingly, DDX58 was not among them. This provided for us a further exclusion test, supporting the fact that DDX58 protein might not be affected by the overexpression of TDP-43, as much as by TDP-43 depletion.

Long-term perspectives

With our collaborators, using primary SOD1 astrocytes we intend to test the presence of DEGs miRNAs in secreted vesicles. The possibility to use RNA as biomarker source, at least for SOD1 fALS patient, could depend on the feasibility to detect G93A-specific circulating miRNAs.

In parallel, we might provide insights on the possible SASP-related RNA sequences released in EVs from senescent cells from SOD1 mouse model (and possibly correlating in aging conditions). Whether DDX58 upregulation could mediate this phenotype remains an open question.

Speculating on the involvement of neuroinflammation in the progression of ALS (Vahsen et al. 2021), we suggest the possibility in the future to challenge liquid biopsy in the attempt to find coding or non-coding RNA species circulating in the bloodstream upon DDX58 upregulation and non-conventional (non-viral) RNA recognition. The untangle of pro-inflammatory signals vehiculated from DDX58 is emerging as a field of investigation, given its role in the control of translation and, possibly, stability of mRNA targets involved in inflammation. The evolutionary conservation of DDX58 and its ubiquity in the cells where it acts as a sentinel of exogenous, toxic RNA, might encourage further characterization of RNA biomarkers partially reached by the protein and potentially secreted in response to the non-viral pro-inflammatory DDX58 upregulation.

In conclusion, we provide the scientific community with a novel characterization of DDX58 role associated with EVs. We hint at the need to elucidate in the future the significance of ALS-associated upregulation of this protein and to reconcile it with our description of DDX58 indirect role in regulating miRNA secretion in SOD1 models.

6. MATERIALS AND METHODS

6.1 Cell lines and growth conditions

Mouse motor neuron-like (NSC-34) and Human Embryo kidney HEK293T (ATCC) cell lines were grown in standard conditions in Dulbecco's modified Eagle's medium (DMEM) supplemented with 10% Fetal Bovine Serum, 1% L-glutamine, and 1% penicillin /streptomycin (LifeTechnologies, Carlsbad, CA, USA). Cells were regularly passaged and kept at 37°C, humidified in 5% CO_2.

Human induced pluripotent stem cells (hiPSCs) were kindly provided from collaborators in the Institute of Biomedical Research of Lleida, Spain (IRBLleida). In this study, we used control iPS cell line (Cat. CS83iCTR-33nxx) and SOD1 H44R iPSCs (Cat. CS04iALS-SOD1H44Rnxx) all purchased from Cedars-Sinai Biomanufacturing Centre (West Hollywood, CA, USA). Stem cells were thawed and cultured in mTeSR Plus medium (Stem Cells Technologies, Vancouver, Canada) following SOP-iPSC-003 directives provided by Cedars-Sinai. Geltrex® (Thermo Fisher Scientific)-coated tissue culture vessels were used at all differentiation steps as we exploited the differentiation media substitution using the recipes found in Table 1. Neuroepithelial media was used on stem cells colonies for 1 week and then sequentially changed with motor neuron progenitor (MNP) media 1 and MNP media 2 for one week each. ROCK inhibitor Y27632 (Stem Cells Technologies) 10µM was added in the first 24 h after splitting that was regularly performed according to confluency.

At the level of MNP 2nd progenitors were either passaged, cryopreserved in CryoStor® CS10 (Stem Cells Technologies) or differentiated into neurospheres using motor neuron (MN) induction media. For the latter, non-tissue culture dishes were used for neurosphere formation. After 6 days in induction media, neurospheres were collected and gently centrifuged for 5 min at 100 g to remove the supernatant. The pelleted spheres were digested in Accumax solution (Sigma) for 10 min and cell clusters were pipetted vigorously to disaggregate them into a homogenous suspension. After a wash with DMEM/F12 (Thermo Fisher Scientific), motor neuron maturation media supplemented with Y27632, 2.5 µg/mL laminin (Thermo Fisher Scientific) and 0.1 µM

Compound-E (Stem Cell Technologies) was used for seeding and motor neuron differentiation in poly-L- lysine (Sigma) coated 24-well plates.

	Neuroepithelial	**MNP 1st**	**MNP 2nd**	**MN induction**	**MN maturation**
DMEM**/F12**	20 ml	20 ml			
Neurobasal	20 ml	20 ml			
Neurobasal +			40 ml	40 ml	40 ml
B27+ supplement	800 µl	800 µl	800 µl	800 µl	800 µl
Ascorbic acid	0.1 mM	0.1 mM	0.1 mM	0.1 mM	0.1 mM
L-Glutamine solution	1:200	1:200	1:200	1:200	1:200
Nonessential amino acids	1:100	1:100	1:100	-	-
CHIR99021	3 µM	1 µM	3 µM	3 µM	
SB43	2 µM	2 µM	2 µM	1 µM	
DMH1	2 µM	2 µM	2 µM	2 µM	
Retinoic acid		0.1 µM	0.1 µM	0.5 µM	0.5 µM
Purmorphamine		0.5 µM	0.5 µM	0.1 µM	0.1 µM
Valproic acid			0.5 mM		
CNTF					20 ng/ml
IGF1					20 ng/ml
Penicillin/Streptomycin	1:400	1:400	1:400	1:400	1:400

Table 1 - Components of the media used for the differentiation of hiPSC to mature motor neurons. Details of the materials suppliers can be retrieved in Table S3 of Ramírez-Nuñez et al, 2021 **(Ramírez-Nuñez et al. 2021)**

6.2 Lipofection

One day after seeding, NSC34, HEK293T and MNP 2nd progenitors cells were transfected with plasmid DNA for the expression of tGFP-tagged human DDX58 NM_014314 (Cat. RG217615, Origene, Rockville, MD, USA) and HA-HIS-tagged human SOD1 wt and G93A protein gently provided us from the Laboratory of Transcriptional Neurobiology led by

Prof. Manuela Basso (Trento, Italy). A ratio of 1.25 μg DNA/million of cells was chosen for lipofection using Lipofectamine™ 3000 Transfection Reagent (L3000015 Invitrogen) following the provided standard protocol with minor modifications. Specifically, the transfected polyplexes were maintained in contact with the cells for at least 24 hours before medium substitution and cells were cultured for an additional day before proceeding with the different experiments. IPS-derived motor neurons were transfected with Lipofectamine™ RNAiMAX Transfection Reagent (13778075 – Invitrogen), following producer instructions.

6.3 Immunocytochemistry

For immunofluorescence (IF), 15 mm diameter coverslips were added on the bottom of 12 well plate and coated with poly-D-lysine (PDL) (P7280, Sigma) diluted 1:1000 in PBS at RT for 45 minutes. After coating, $3x10^5$ NSC34 cells were seeded. The following day cells were transfected for the time required for the experiment. Then, either cells were stained with MitoTracker™ or LysoTracker™ reagents, or the IF protocol proceeded directly with fixation. In detail, MitoTracker Orange (M7510, Invitrogen) was added to a final concentration of 200 nM, while LysoTracker Deep Red (L12492, Invitrogen) was used at 50 nM concentration. Both staining reagents were incubated for 25 minutes at 37 °C. Fixation was performed with pre-heated 4% paraformaldehyde solution (from 37% in methanol stabilized stock, F8775, Sigma) diluted in PBS and incubated with the cells for 10 min. Fixed cells were washed in ice cold PBS three times for 5 min each. For immunostaining, cell membrane permeabilization was obtained by adding 0.1% Triton-X in PBS incubated for 5 min before additional 3 washing steps. For blocking, we used 500 μl of 10% FBS + 0.05% Triton-X solution for 1 h at RT. Primary antibodies were diluted according to the manufacturer instruction in a solution of 0.1% FBS + 0.05% Triton-X. Coverslips were positioned on a drop of primary antibody and incubated at 4 °C overnight. Later, cells were washed three times before incubation with fluorescent AlexaFluor secondary antibody diluted 1:1000 in 0.1% FBS + 0.05% Triton at RT for 1 hour. Secondary Ab was washed and then cell nuclei were labeled with PBS solution of Hoechst33342 (62249 - Invitrogen) 1:8000 for 15 min. At the end, microscope slices were finalized with ProLong™ Diamond Antifade Mountant reagent (Invitrogen) and

dried at RT for at least 2 hours before imaging. Leica TCS SP8 (Leica Microsystems, Wetzlar, Germany) confocal microscope with a HI-PLAN 63X objective was used for images acquisition.

List of antibodies used:

Primary antibodies: anti-DDX58 (3743 – Cell Signaling Technologies) 1:200, anti-DDX58 (700366 – Life Technologies) 1:200, anti SOD1 (711818 – Life Technologies), anti-HA (2367 – Cell Signaling) 1:100, anti-TIA (ab2712 – Abcam) 1:200, anti-DCP1A (ab57654 – Abcam) 1:200.

Secondary antibodies: goat anti-rabbit AlexaFluor-488 (A11034), -633 (A21071); goat anti-mouse AlexaFluor-56 (A11031), -633 (A21052) all diluted 1:1000, all purchased from Invitrogen.

6.4 EV isolation

6.4.1 Nickel-based Isolation (NBI)

For biophysical characterization and EV-RNA extraction from NSC34, HEK293T and primary SOD1 astrocytes, EVs were isolated by nickel-based isolation (NBI), a novel methodology to extract from biofluids polydisperse heterogenous EVs in a rapid and reproducible way (Notarangelo et al. 2019, 2020).

In detail, positively charged Ni Sepharose® High Performance beads (GE Healthcare, 17-5268-01) are re-functionalized following the procedure described by Notarangelo et al (Notarangelo et al. 2020) in order to obtain a suspension of 20 mg/ml in PBS, functionalized using a 0.4 M $NiSO_4$ (Sigma) solution that confers the charge to the matrix necessary to maximize the capture of negatively charged EVs. Isolation was performed on 2,800g spun serum-free media collected from NSC-34, HEK293T, astrocytes and iPS-derived motor neurons. Volume processed varied according to the growth vessel used ranging from 1 mL to 15 mL per condition. In brief, 25 µL/mL of NBI beads were added to the cell-conditioned media and incubated in orbital shaking at RT for 30 min. EV-enriched beads were gently centrifuged (~600-700g) and the supernatant removed. EV elution from the beads was obtained through the addition of EV elution buffer, composed of solution A (16 mM EDTA, UltraPure pH 8.0, ThermoFisher) and solution B

(10 mM NaCl, 225 µM citric acid, Sigma) diluted 5-fold in PBS. A volume of 1X elution buffer equal to the volume of beads added was incubated 15 min at 28°C in a thermoshaker. The suspension was spun 1 min at 1,800g to recover the eluted EVs in the supernatant.

6.4.2 Ultracentrifugation-based methods

For vesicular protein detection via Western blot, EV-RNA biotinylated probe production, RNA immunoprecipitation and EVs cell treatment, EVs were recovered exploiting ultracentrifugation (UC)-based methods.

EVs were pelleted from ~20 mL of cell-conditioned FBS-free DMEM using an Optima XPN-100 ultracentrifuge (Beckman Coulter, Brea, CA, USA). Cell media was centrifuged 10 min at 2,800g and the supernatant was transferred to open-top Ultra-Clear centrifuge tubes (344058, Beckman Coulter) subjected to 100,000g ultracentrifugation for 70 minutes at 4 °C under vacuum using a SW 32 Ti swinging bucket rotor. After centrifugation, the supernatant was decanted, and EV-containing pellet was gently resuspended in an appropriate volume of 0.22 µm filtered PBS for further applications.

For differential ultracentrifugation (dUC), an intermediate step of centrifugation in the same setting was performed at 10,000g for 70 min at 4°C and the resulting supernatant was subjected to the previously described step at 100,000g.

For the OptiPrepTM™ density gradient ultracentrifugation (ODG), EV containing gradient fractions were analyzed following the procedure previously reported with minor changes (Van Deun et al. 2014). Briefly, from a stock solution of 60% iodixanol (OptiPrep™ Density Gradient Medium, D1556, Sigma) a pre-dilution of 50% iodixanol was prepared in working buffer (0.25M sucrose, 6 mM EDTA, 60 mM Tris-HCl, pH 7.4). Consequently, solutions of 5, 10, 20 and 40% iodixanol were prepared in homogenization buffer (0.25M sucrose, 1 mM EDTA, 10 mM Tris-HCl, pH 7.4). The gradient was constituted by layering 4 mL of 40%, 4 mL of 20%, 4 mL of 10% and 3.5 mL of 5% iodixanol on top of each other in a 16.8 mL open-top polyallomer tubes (Beckman Coulter). Tubes were filled with 5% solution and carefully closed with parafilm, gently positioned horizontally for 2 hours, then 1 mL was removed from the top and samples of concentrated cell culture medium (ultrafiltered medium concentrated from 30 to 1

mL) were layered on the tubes. After loading, the tubes were centrifuged using SW41 Ti swinging bucket rotor (Beckman Coulter) for 18 h at 4°C. To prepare the protein samples 1 mL fractions were collected manually in 2 mL tubes. A volume of 500 µL PBS was added together with 150 µL tricarboxylic acid (TCA). Protein precipitation was reached after 10 min incubation at RT, vigorous shaking and 5 min centrifugation at 14,000g in a chilled table centrifuge. The pellet was washed in acetone and dried at 95°C in a heat block. Dry pellets were boiled in Laemmli buffer to proceed onto SDS-PAGE and Western blotting.

6.5. EV biophysical characterization

6.5.1. Nanoparticle Tracking Analysis (NTA)

Nanoparticle Tracking Analysis (NTA) was conducted through NanoSight NS300 instrument (Malvern Panalytical Ltd., Malvern, UK) equipped with a 488 nm blue laser and a sCMOS camera, according to the manufacturer's instructions. Samples were diluted in filtered PBS and the flow cell was washed with milliQ water between different samples. For each sample, three individual consecutive 60 seconds videos were acquired. The syringe pump was fixed at 30 a.u. to have a continuous flow of the suspension in the chamber. The acquisition was performed with camera level set at 15 and the analysis detection threshold was adjusted depending on the individual signal noise between 3 and 5 to reach a ratio of particles valid/invalid at maximum equal to 1:5. The analysis was performed using the built-in NanoSight Software NTA3.3.301 (Malvern). Information of particles concentration, mean and mode diameter was retrieved downstream the processing.

6.5.2 Tunable Resistive Pulse Sensing (tRPS)

In the case of SOD1 mice derived EVs, also tunable Resistive Pulse Sensing measurement were conducted via Izon qNano Gold apparatus (Izon Science, Christchurch, New Zealand) mounting a NP250 nanopore calibrated with CPC200 calibration beads (Izon Science). Nanopore was stretched between 45.5 and 47 mm and instrument voltage was kept below 0.68 mV to reach a stable current baseline around 1000 nA (noise below 10–12 pA) and a linear particle count rate. After acquisition qNano data were processed by the Izon Control Suite v.3.

6.5.3 Dynamic Light Scattering: ζ potential assessment

Astrocytes EVs Zeta potential was assessed using Malvern ZetaSizer Nano ZS instrument. Samples were diluted in millQ water (at least 1:50) and loaded on disposable folded capillary cuvettes (DTS1070 - Malvern). Data reported resulted from three technical measurements with default settings.

6.6 Total cell RNA and EV-RNA extraction

RNA was isolated from cell pellets using TRI Reagent® (T9424, Sigma) following manufacturer's instruction. In particular, a volume of 300-1000 µL of reagent was used for the homogenization of the cell pellet and incubated at RT for 5 min to allow the dissociation of nucleoprotein complexes. Chloroform was added (0.2 mL per 1 mL of TRI Reagent®) to the tube before a vigorous shaking. Then the mixture was left 3 min RT and spun in a pre-chilled table centrifuge at 12,000g for 15 minutes. The upper aqueous phase was carefully recovered avoiding to touch the interphase with the lower organic phase. A volume of 0.5 mL of isopropanol per 1 mL of TRI Reagent® and was used to allow RNA precipitation upon O/N incubation at -80 °C (RNase-free glycogen < 4 mg/mL was added at this step to favor the precipitation). RNA precipitates were centrifuged at 12,000g 10 min and washed with an addition of 75% ethanol. After decanting, RNA pellets were dried and resuspended in RNase-free water and quantified via ThermoFisher Nanodrop 2000 Spectrophotometer.

EV-RNA was extracted from NBI eluates or from PBS-resuspended UC pellets using Single Cell RNA Isolation Kit (51800, Norgen Biotek Corp, Thorold, Canada) with no modifications. EV-RNA was eluted from columns with 10-20 µL of RNase-free water and 1.5 µL aliquots were conserved from RNA profiling. EV-RNA profiling and quantification was performed using Total Eukaryotic RNA Pico chips (Agilent Technologies, Santa Clara, CA, US) following the manufacturer's instruction and loading 1 µL of RNA per well. Chip were analyzed on 2100 Bioanalyzer (Agilent) instrument, data processed on 2100 Expert software (Agilent) were used for the smear analysis.

6.9 Biochemical methods

6.9.1 Immunoprecipitation (IP)

For DDX58 and SOD1 immunoprecipitation experiments, 3 x 10^6 NSC34 cells were cultured in 10 cm^2 tissue culture dishes (Corning Inc, New York, NY, US). Cells were transfected for 24h and then exhaust media were removed, cells were washed in ice cold PBS and 500 µL of cold Buffer IP 1X (50 mM HEPES, 150 mM NaCl, 1 mM $MgCl_2$, 1mM DTT, 0.05% glycerol, Halt™ Protease Inhibitor Cocktail 1X, pH 8.0) and detached using a cell scraper. Cells were sonicated (13 cycles, 40 amplitude, 7 sec ON, 10 sec OFF) and lysed membranes centrifuged for 15 min at maximum speed in a refrigerated microcentrifuge. Lysates were recovered from the supernatant and split with equal volumes in two Eppendorf tubes. Input samples were kept (50 µL/sample) and then 250 µL Buffer IP 1X were added per tube. The following antibodies were added with 2 µg fixed amount per tube: anti-DDX58 antibody (35H2L48 – Invitrogen), anti-SOD1 antibody (711818 – Invitrogen), anti-HA tag antibody (ab1424 – Abcam, Cambridge, UK), Normal rabbit IgG (#2729 – Cell Signaling Technology, Danvers, MA, US). Lysates were incubated with the antibodies for 30 minutes in orbital shaking in cold room. Later, 0.6 mg of Dynabeads™ Protein G (10003D, Invitrogen) washed in Buffer IP were added to the immune-complexes and incubated in shaking for 1 h. Magnetic separation was performed and the flow-through discarded. Then, the IP-beads were washed 3 times with Buffer IP and boiled at 95°C for 10 min in Laemmli buffer for subsequent SDS-PAGE and western blotting analysis.

Similarly, in the Fractionation-IP approach, two 10 cm^2 dishes of cultured NSC34 cells were used as input and mildly lysed with fractionation buffer (10 mM NaCl, 10 mM $MgCl_2$, 10 mM Tris-HCl, 1% Triton-X100, 1% sodium deoxycholate, 1 mM DTT, Halt™ Protease Inhibitor Cocktail 1X, pH 7.5). After lysis, nuclei were pelleted 5 min at 13,000g at 4°C and resuspended in equal volume of buffer after cytosolic proteins-containing supernatant was separated. RNase A was added (2 µg/µL) and incubated in treated samples for 10 minutes RT. The protocol for IP using anti-SOD1 proceeded with no modification, as already described.

6.9.2 Biotinylated EV-RNA Pulldown

Pull down assay was performed on DDX58-tGFP, HA-SOD1 and endogenous TDP-43 from HEK293T cells. For the assay, 40 ng of UC-derived EV-RNA, isolated as previously described, were used as input for the 3' biotinylation strategy. We exploited the first polyadenylation reaction following TaqMan™ Advanced miRNA cDNA Synthesis Kit (Applied Biosystems™ - A28007). Polyadenylated EV-RNA was purified by Norgen columns and eluted in 20 µL, then it was hybridized with a commercial oligo dT-biotinTEG. RNA/DNA hybrid was formed incubating RNA and oligo dT (100 µM stock) in a 19:1 v/v ratio, heating the mixture at 70 °C for 1 min, followed by 10 min at RT before immediate use.

For pull down lysate preparation, one 10 cm^2 culture dish containing 3 million cells was used. DDX58-tGFP-encoding plasmid was transfected as described above. Cells were lysed in Lysis buffer (25 mM HEPES pH 7.5, 100 mM NaCl, 1X Halt™ Protease Inhibitor Cocktail) and sonicated in ice (35-40 amplitude, 6 cycles, 7 sec on and 45 sec off). Lysates were centrifuged at 14,000g for 20 min at 4°C. Supernatant was recovered and protein amount measured via Pierce™ BCA Protein Assay (23228 – ThermoFischerScientific). Streptavidin Dynabeads™ M-280 (Invitrogen, 11205D) were equilibrated in lysis buffer exploiting magnetic rack DynaMag™-2. Then, 300 µg of lysates were pre-cleared for non-specific protein removal, incubating it with 5 µL pre-washed beads for 15 minutes at 4 °C in orbital shaking. Magnetic separation was performed and 6 µL of biotinylated EV-RNA were incubated 20 min at 4°C. Later, 5 µL of streptavidin bead were added to the samples and incubated for 1h at 4 °C in rotation. After the magnetic separation, the Flowthrough (FT) samples was kept, and the beads were washed twice with 300 µL of Lysis buffer. Laemmli buffer 1X was added to the beads and heated at 95°C for 5 minutes before SDS-PAGE.

6.9.3 Subcellular fractionation

For subcellular fractionation, a protocol modified in our lab from Baghirova et al was executed on HEK293T cells. Briefly, HEK293T cells were transfected with DDX58-tGFP for 48 or 96 hours and pelleted in 15 mL falcon tubes. 0.5 µL (roughly corresponding to 1% of the wet pellet volume) was kept as input and boiled at 98°C for 20 minutes in 2X

Laemmli buffer. The fractionation occurred using three lysis buffers with crescent stringency (Lysis buffer A, B and C). Recipes of the buffers are shown in the table below. The remaining pellet was resuspended in 350 µL of ice-cold Lysis Buffer A and incubated on end-over-end rotator for 10 min at 4°C. After a centrifugation step at 2000 x g for 10 min at 4°C, 15 µL of the supernatant, containing the cytosolic proteins, were kept and boiled at 98°C for 5 min in 4X Laemmli buffer. The pellet was resuspended in 350 µL of ice-cold Lysis Buffer B and vortexed.

After a 30min incubation at 4°C the samples were centrifuged at 7000 x g for 10 min at 4°C. Then, 15 µL of the supernatant, containing the proteins from membrane-bound organelles, were kept and boiled at 98°C for 5 min in 4X Laemmli buffer. The pellet was resuspended in 350 µL of ice-cold Lysis Buffer C and 4 µL/sample of benzonase (25 U/ µL) were added. After a 30 min incubation on an end-over-end rotator at 4°C, the samples were subjected to one cycle of water bath sonication (35 Amp, 10 sec on, 5 sec off, 45 sec in total) and centrifuged at 7800 x g for 10 min at 4°C. 15 µL of the supernatant, containing the nuclear proteins, were kept and boiled at 98°C for 5 min in 4X Laemmli buffer.

	Lysis buffer A	**Lysis buffer B**	**Lysis buffer C**
NaCl	10 mM	10 mM	10 mM
$MgCl_2$	10 mM	10 mM	10 mM
HEPES	10 mM	10 mM	10 mM
DTT	1 mM	1 mM	1 mM
Glycerol	10%	10%	10%
Halt™ Protease Inhib. Cocktail 100X	1X	1X	1X
Digitonin	25 µg/mL	-	-
NP-40	-	1%	-
Triton X-100	-	-	1%
Sodium deoxycholate	-	-	1%
PBS 1X	Up to volume	Up to volume	Up to volume

6.9.4 Western blotting

For Western blotting, NSC34, iPS-derived motor neuron progenitors and HeLa cells were lysed in protein lysis buffer (50 mM Tris-HCl, 150 mM NaCl, 1mM EDTA, 0.25% Igepal, 0.1% Triton X-100, 0.1% SDS, Halt™ Protease Inhibitor Cocktail 1X, -ThermoFIsher,78429, pH7.4) and spun in a pre-chilled centrifuge at 14,000g for 20 min. The supernatant was quantified for protein content using Pierce™ BCA Protein Assay Kit (ThermoFisher).

Up to 40 μg of lysates were loaded on 12% acrylamide gel and running was done in Tris-Glycine buffer 1X. Protein transfer was done in Tris-Glycine buffer 1X with 20% methanol, on activated polyvinylidene difluoride (PVDF) membrane. For nonspecific protein blocking, membranes were incubated with a suspension of 5% nonfat-dry milk in Tris-buffered saline for 1 hour. Primary antibodies were diluted in a suspension of 3% nonfat-dry milk in TBS-T (Tris-buffered saline, 0.1% Tween-20) and incubated O/N. After 1 hour incubation with the secondary antibody, the signal was signal was measured with Amersham ECL HRP-Conjugated Antibodies (Cytiva) using Bio-Rad Chemidoc XRS+. Finally, the bands intensities were quantified using ImageJ software.

Primary antibodies used: anti-DDX58 (3743 – Cell Signaling Technologies) 1:1000, anti-DDX58 (700366 – Life Technologies) 1:1000, anti SOD1 (711818 – Life Technologies) 1:1000, anti-HA (2367 – Cell Signaling) 1:1000, anti-syntenin (ab133267 – Abcam) 1:10,000, anti-actin (ab198991 – Abcam) 1:10,000, anti-GAPDH (GTX627408 – GeneTex, Irvine, CA, US) 1:10,000, anti-LaminAC (GTX101127 – GeneTex) 1:10,000, anti-alpha-tubulin (11224-1-AP - ProteinTech Group, Manchester, UK) 1:10,000, anti-VAP-B (14477-1-AP – ProteinTech) 1:1000, anti-H3 (GTX122148 – GeneTex) 1:1000, anti-TDP-43 (10782-2-AP – ProteinTech) 1:1000.

Secondary antibodies used (1:10,000): Goat Anti-Rabbit (Jackson ImmunoResearch Laboratories, Inc.), Goat Anti Mouse (Jackson ImmunoResearch Laboratories, Inc.).

6.10 High-content imaging

To assess the co-distribution of DDX58-tGFP and co-expressed wt or mutant HA-SOD1 protein, High-content imaging measurement was exploited. NSC34 cells were seeded in poly-D-lysine pre-treated CellCarrier-96 Ultra Microplates tissue culture 96-well plates

(Perkin Elmer, Waltham, MA, US) at day 1 with a seeding density of 10,000 cells/well. 50 ng of DNA plasmids were transfected for 48 h as described above. Immunocytochemistry was performed analogously as already described. Imaging and analysis were entirely performed by CIBIO HTS Core facility stuff. ImageXpress MD Microconfocal instrument was used (MolecularDevices) exploiting custom module of MetaXpress analysis software.

6.11 RT-qPCR

One microgram of RNA was retrotranscribed using TaqMan Reverse Transcription Reagent with random hexamers (N8080234, Thermo Fisher Scientific) in the mix. RT-qPCR were performed using a CFX96 instrument (Bio-Rad) with SYBR Select Master Mix (4472908, Thermo). In 20 µl reaction mix 4 µl cDNA, 0.2 nM forward primer and 0.2 nM reverse primer, 10 µl SYBR Select Master Mix, 4 µl water were put. The run protocol was: 50°C for 2 min and 95°C for 2 min, with 40 cycles of 95°C for 15 s and 60°C for 1 min; a melting curve test from 65°C to 95°C at a 0.1°C/s rate was set. Primers employed are listed below:

Actb Fw : GTGACGTTGACATCCGTAAAGA
Actb Rev : GCCGGACTCATCGTACTCC
mY3 Fw : GGTTGGTCCGAGAGTAGTGG
mY3 Rv : AAAGGCTGGTCAAGTGAAGC
p16 Fw : CCCAACGCCCCGAACT
p16 Rev : GCAGAAGAGCTGCTACGTGAA
Ddx58 Fw : CTGATGAAGGCATTGACATTGCT
Ddx58 Rv : CTATCTCGTGCTCTTCCTCG
GAPDH Fw : GTTCGACAGTCAGCCGCATC
GAPDH Rv : GGAATTTGCCATGGGTGGA
hY3 Fw : GGCTGGTCCGAGTGCAGTG
hY3 Rv : GAAGCAGTGGGAGTGGAGAA
DDX58 Fw : CTGATGAAGGCATTGACATTGCA
DDX58 Rv : CTACCTCTTGCTCTTCCTCT
TARDBP Fw : AATTCTGCATGCCCCAGA
TARDBP Rv : GAAGCATCTGTCTCATCCATTTT

6.12 Digital droplet PCR

For digital droplet PCR (ddPCR), cDNA from both vesicular and cellular RNA was obtained using the TaqMan™ Advanced miRNA cDNA Synthesis Kit (Applied Biosystems™ - A28007) following instructions provided by the manufacturer. 2 ng of RNA diluted in UltraPure™ DNase/RNase-Free Distilled Water (Invitrogen™ - 10977015) was used in a 2 µL template for the first reaction. RNA was Poly(A)denylated at the 3' and ligated with a 5' adapter provided by the kit. Then retrotranscribed RNA was stored at -20 °C for maximum 2 months. The final miR-Amp reaction was performed on cDNA product before digital droplet PCR (ddPCR) analysis.

The following commercial Advance TaqMan miRNA assays (Life Technologies) were optimized for ddPCR setting to detect the miRNAs: hsa-miR-1910-3p (479581_mir), hsa-miR-130-5p (mmu480918_mir), mmu-miR-709 (mmu482967_mir). cDNA was firstly diluted 1:80 in UltraPure™ DNase/RNase-Free Distilled Water in 6µL used as input for the droplet generation. Per each sample we added: 1.15 µL of 20X miRNA probe, 11.5 µL of 2X ddPCR Supermix for Probes (Bio-Rad - 1863026) and 4.35 µL of water. Similarly, EvaGreen Supermix was used for the generation and amplification of Y3 RNA as ddPCR internal reference. In this setting, we used the same cDNA input and added 50nM Y3 primers (mouse: mY3 Fw : 5'-GGTTGGTCCGAGAGTAGTGG-3', mY3 Rv : 5'-AAAGGCTGGTCAAGTGAAGC-3'; Human: hY3 Fw : GGCTGGTCCGAGTGCAGTG, hY3 Rv : GAAGCAGTGGGAGTGGAGAA), 11.5 µL of QX200 ddPCR EvaGreen Supermix (Bio-Rad - 1864033) and water up to 23 µL. In both TaqMan and Y3 cases, droplets were transferred on 96 wells plate, which was sealed with PCR Plate Sealer™ for the PCR. According to the different Supermix used, PCR amplification was performed following Bio-Rad instruction and using a deep-well C1000 Thermocycler (Bio-Rad). FAM Signal was detected with a QX200 Droplet Reader™(Bio-Rad). Data processing was done using QuantaSoft Software™ (Bio-Rad).

6.13 DDX58-tGFP cells sorting

For the RNA-Seq on DDX58-tGFP overexpressing cells, a fluorescence associated cell sorting (FACS) procedure was followed. The sorting was entirely performed in collaboration with the CIBIO core facility of Cell Analysis and Separation.

NSC34 cells were plated in 10 cm^2 dishes and transfected, as described above. Cells were trypsinized and resuspended in appropriate volumes of Sorting Buffer (PBS 1X, 1% FBS, 2% penicillin /streptomycin, 1 mM EDTA) and transferred to polypropylene round-bottom tubes after filtering the suspension across a sterile 30 µm filter. BD FACS Aria™ II (Becton, Dickinson and Company, Franklin Lakes, NJ, US) instrumentation equipped with 488 nm blue laser and mounted with a 100 µm nozzle was used for the separation of tGFP-positive and tGFP-negative cells with a 1:1 ratio. Cells were collected in DMEM supplemented with 2% penicillin /streptomycin and plated in two cell culture dishes in a seeding density of 600,000-800,000 cells per dish respectively for tGFP-negative and positive cells. Media was changed after 48h to allow EVs isolation.

6.14 cDNA library preparation

NGS libraries were prepared using QIAseq miRNA Library Kit (Qiagen) following manufacturer instructions. Before cDNA synthesis, NGS adaptor containing Unique Molecular Identifiers (UMI) were ligated to the 3' and 5' end of miRNAs. Reverse transcription (RT) primer binds to a region of the 3' adapter and allows the conversion of ligated miRNAs to cDNA. The products underwent cleanup using a QIAseq miRNA NGS (QMN) beads. Subsequently, amplification was performed with HotStarTaq DNA Polymerase and universal primers that assign the indexes used for sample definition after pool formation. Pools were balanced with the expertise of CIBIO NGS Core Facility, after quality checks. In the lab, we provided them the following QCs: cDNA libraries were assessed at 2100 Bioanalyzer (Agilent) using HS DNA kit. Capillary electrophoresis confirmed the presence of miRNA-sized library (160-175bp). Next, the concentration of prepared libraries was measured with a Qubit Fluorometer (Thermo Fisher Scientific, USA, Waltham).

6.15 Next Generation Sequencing and Bioinformatic Analyses

NGS data were obtained from our NGS CIBIO Core Facility entirely running the sequencing of flow cell on NovaSeq 6000 instrument (Illumina). Data was analyzed by our collaborators Margherita Squillario (UniGE) and Prof. Silvano Piazza (ICGEB, Trieste).

The first analysis was performed following the NFcore smRNA-Seq pipeline (10.5281/zenodo.7789554) and the reported differentially abundance was visualized as box plots kindly provided us by Dr Squillario FDR<0.05 was considered significant.

For the second comprehensive analysis, sRNAtoolbox (Aparicio-Puerta et al. 2022), a collection of small RNA analysis tools, was used to generate the features' counts. The generated feature counts were consequently analyzed using R package DESeq2 (Love, Huber, and Anders 2014). The normalized count matrix was obtained from variance stabilizing transformation (VST) method as implemented in DESeq2 package. In order to explore high-dimensional data property, among the available algorithms, Principal Component Analysis (PCA) coupled with a dimensionality reduction algorithm was used to scale data. In order to select only the statistically significant changing features between comparison of interest, a differential gene expression analysis was performed. The differentially expressed features (DEFs) were selected with a p-adjusted cut off of 0.05 and a log2 Fold Change value greater than 1 (up-regulated DEFs) or lower than -1 (down-regulated DEFs). P-value was adjusted for multiple testing using the Benjamini–Hochberg (BH) correction with a false discovery rate (FDR) ≤ 0.05. DEFs were then visualized with a hierarchical clustering method, using correlation distance. Visualization of log2-normalized values and clustering was obtained with the ComplexHeatmap package (Gu, Eils, and Schlesner 2016). To be able to identify features biological identities and the pathways they belong to, a functional annotation analysis was performed for all the comparisons and for feature list of interest with gprofiler2 package (Raudvere et al. 2019). Different databases were used to annotate the DEFs: Gene Ontology (Molecular Functions – MF, Biological Processes – BP, Cellular Component – CC), Kyoto Encyclopedia of Genes and Genomes (KEGG), Reactome, WikiPathways (WP), Transfac (TF), miRTarBase (MIRNA), Human Protein Atlas (HPA), CORUM (CORUM protein complexes), Human Phenotype Ontology (HP), RNA central. Functional annotation results were visualized with ggpubr package (https://rpkgs.datanovia.com/ggpubr) via Balloon plots.

6.17 NF-κB luciferase reporter assay

HEK293T cells were plated in 96-well plates (for acute treatment) or in transwell (see 6.19, for chronic mimicking experiment). Cells were co-transfected with pGL3-basic-NF-κB-RE, for the expression of NF-κB responsive element and pRL-SV40 vector for Renilla luciferase constitutive expression, used as internal transfection control. Luciferase signal was measured by Dual-Glo® Luciferase Assay System (E2920, Promega) following the instructions of the manufacturer. Briefly, Dual-Glo® Reagent was added in the wells in a 1:1 volume ratio and mixed. NF-κB dependent firefly luminescence signal was measured using Varioskan™ LUX Multimode Microplate Reader (Thermo). Then, similarly Dual-Glo® Stop & Glo® Reagent was added 1:3 in the mixture and after 10 min incubation control Renilla luminescence was measured. The Firefly signal was normalized over the internal Renilla control and plotted in percentage vs control.

6.18 Senescence phenotype induction in mouse primary fibroblast

B6.Cg-Tg(SOD1*G93A)1Gur/J mice were kindly provided by Prof Manuel Portero-Otin and maintained following the guidelines of University of Lleida, Spain. Fibroblasts were sectioned from the ears of G93A and wt mice. Both ears were cut and treated for 45 min at constant shaking at 37°C with 0.2 U/ml type II collagenase (LS004174, Worthington Biochemicals). Fibroblast were isolated from supernatants after short centrifuge to avoid cell damage every 15 min. Fibroblasts were finally seeded in 10 cm^2 dishes and grown in normal conditions. Non-senescent fibroblasts were defined at 10 days-in-vitro (10DIV) while senescent cells when they stopped growing. The treatment had been performed already when we analyzed Ddx58 mRNA. Cells had been treated with dasatinib (250 nM)+quercetin (50 µM), Navitoclax (20 µM) or 0.5% [dimethyl sulfoxide (DMSO)] for 72 h. RNA was extracted using TRIzol.

6.19 Transwell co-culture and cell viability assay

Astrocytes from neonatal pups' spinal cord were cultured by our collaborators and kindly provided (lab led by Prof. Giambattista Bonanno and by Prof Manuela Basso, respectively UniGE and CIBIO, UniTN). At the time of the experiment, sent astrocytes were trypsinized and plated at a density of 50,000 cell/well in 24-well plates. Meanwhile, NSC-34 cells were plated (10,000 cells/vessel) in transwell vessels (TC insert, CO 0.4 µm,

PET, transparent, 83.3932.041 – Sarstedt, Germany). The day after transwell were transfected for DDX58-tGFP expression. Astrocytes and NSC34 were co-incubated for 24 h and then viability was measured via ATP detection through CellTiter-Glo® Luminescent Cell Viability Assay (Promega). ATP was used as positive control and simple DMEM as negative. The protocol detailed by the manufacturer was followed with no modification. The reagent was used 1:1 with the exhausted media on NSC34-harboring transwells and transferred on 96 well plates. After 5 minutes shaking to allow lysis, the plate containing the mixture was put in Varioskan™ LUX Multimode Microplate Reader (Thermo) for luminescence signal reading.

6.20 Statistical analyses

In figure legends are indicated the number of independent experiments relative test performed. GraphPad Prism Software v 9 was used to calculate ANOVA, t-test, and Pearson r coefficient and the results were considered statistically significant when P value was <0.05 (*), <0.01 (**), <0.001 (***).

Bibliography

Abels, Erik R., and Xandra O. Breakefield. 2016. “Introduction to Extracellular Vesicles: Biogenesis, RNA Cargo Selection, Content, Release, and Uptake.” *Cellular and Molecular Neurobiology* 36(3): 301–12.

Ablasser, Andrea et al. 2009. “RIG-I-Dependent Sensing of Poly(DA:DT) through the Induction of an RNA Polymerase III-Transcribed RNA Intermediate.” *Nature Immunology* 10(10): 1065–72.

Ahadi, Alireza et al. 2016. “Long Non-Coding RNAs Harboring MiRNA Seed Regions Are Enriched in Prostate Cancer Exosomes.” *Scientific Reports* 6: 1–14.

Alrafiah, Aziza Rashed. 2018. “From Mouse Models to Human Disease: An Approach for Amyotrophic Lateral Sclerosis.” *In vivo (Athens, Greece)* 32(5): 983–98.

Aparicio-Puerta, Ernesto et al. 2022. “SRNAbench and SRNAtoolbox 2022 Update: Accurate MiRNA and SncRNA Profiling for Model and Non-Model Organisms.” *Nucleic Acids Research* 50(W1): W710–17.

Baghirova, Sabina, Bryan G. Hughes, Michael J. Hendzel, and Richard Schulz. 2015. “Sequential Fractionation and Isolation of Subcellular Proteins from Tissue or Cultured Cells.” *MethodsX* 2: e440–45. http://dx.doi.org/10.1016/j.mex.2015.11.001.

Banack, Sandra Anne, Rachael Anne Dunlop, and Paul Alan Cox. 2020. “An MiRNA Fingerprint Using Neural-Enriched Extracellular Vesicles from Blood Plasma: Towards a Biomarker for Amyotrophic Lateral Sclerosis/Motor Neuron Disease.” *Open Biology* 10(6).

Baradaran-Heravi, Yalda, Christine Van Broeckhoven, and Julie van der Zee. 2020. “Stress Granule Mediated Protein Aggregation and Underlying Gene Defects in the FTD-ALS Spectrum.” *Neurobiology of Disease* 134(January 2019): 104639. https://doi.org/10.1016/j.nbd.2019.104639.

Basso, Manuela et al. 2013. “Mutant Copper-Zinc Superoxide Dismutase (SOD1) Induces Protein Secretion Pathway Alterations and Exosome Release in Astrocytes: Implications for Disease Spreading and Motor Neuron Pathology in Amyotrophic Lateral Sclerosis.” *Journal of Biological Chemistry* 288(22): 15699–711. http://dx.doi.org/10.1074/jbc.M112.425066.

Belrose, Jillian Corinne, and Michael Frederick Jackson. 2018. “TRPM2: A Candidate Therapeutic

Target for Treating Neurological Diseases." *Acta pharmacologica Sinica* 39(5): 722–32.

Berdyński, Mariusz et al. 2022. "SOD1 Mutations Associated with Amyotrophic Lateral Sclerosis Analysis of Variant Severity." *Scientific Reports* 12(1): 1–11. https://doi.org/10.1038/s41598-021-03891-8.

Bhaskar, Meenakshi, Sriparna Mukherjee, and Anirban Basu. 2021. "Involvement of RIG-I Pathway in Neurotropic Virus-Induced Acute Flaccid Paralysis and Subsequent Spinal Motor Neuron Death." *mBio* 12(6): 1–19.

Billmeier, Martina et al. 2022. "Mechanistic Insights into Non-Coding Y RNA Processing." *RNA Biology* 19(1): 468–80. https://doi.org/10.1080/15476286.2022.2057725.

Boelens, Mirjam C. et al. 2014. "Exosome Transfer from Stromal to Breast Cancer Cells Regulates Therapy Resistance Pathways." *Cell* 159(3): 499–513. http://dx.doi.org/10.1016/j.cell.2014.09.051.

Bourgeois, Cyril F., Franck Mortreux, and Didier Auboeuf. 2016. "The Multiple Functions of RNA Helicases as Drivers and Regulators of Gene Expression." *Nature Reviews Molecular Cell Biology* 17(7): 426–38.

Brockington, Alice et al. 2013. "Unravelling the Enigma of Selective Vulnerability in Neurodegeneration: Motor Neurons Resistant to Degeneration in ALS Show Distinct Gene Expression Characteristics and Decreased Susceptibility to Excitotoxicity." *Acta neuropathologica* 125(1): 95–109.

Brown, Anna Leigh et al. 2022. "TDP-43 Loss and ALS-Risk SNPs Drive Mis-Splicing and Depletion of UNC13A." *Nature* 603(7899): 131–37.

Brown, Robert H, and Ammar Al-Chalabi. 2017. "Amyotrophic Lateral Sclerosis." *The New England journal of medicine* 377(2): 162–72.

Chen, Lin et al. 2023. "Proteomics Analysis Indicates the Involvement of Immunity and Inflammation in the Onset Stage of SOD1-G93A Mouse Model of ALS." *Journal of proteomics* 272: 104776.

Chen, Xingyuan, Xiaomei He, Yen Yu Yang, and Yinsheng Wang. 2022. "Amyotrophic Lateral Sclerosis-Associated Mutants of SOD1 Modulate MiRNA Biogenesis through Aberrant Interactions with Exportin 5." *ACS Chemical Biology* 17(12): 3450–57.

Chen, Y. Grace et al. 2017. "Sensing Self and Foreign Circular RNAs by Intron Identity." *Molecular*

Cell 67(2): 228-238.e5. http://dx.doi.org/10.1016/j.molcel.2017.05.022.

Cheng, Lesley, Robyn A Sharples, Benjamin J Scicluna, and Andrew F Hill. 2014. "Exosomes Provide a Protective and Enriched Source of MiRNA for Biomarker Profiling Compared to Intracellular and Cell-Free Blood." *Journal of extracellular vesicles* 3.

Chiang, Jessica J. et al. 2018. "Viral Unmasking of Cellular 5S RRNA Pseudogene Transcripts Induces RIG-I-Mediated Immunity Article." *Nature Immunology* 19(1): 53–62. http://dx.doi.org/10.1038/s41590-017-0005-y.

Chow, Kwan T., Michael Gale, and Yueh Ming Loo. 2018. "RIG-I and Other RNA Sensors in Antiviral Immunity." *Annual Review of Immunology* 36: 667–94.

Christ, Liliane et al. 2017. "Cellular Functions and Molecular Mechanisms of the ESCRT Membrane-Scission Machinery." *Trends in Biochemical Sciences* 42(1): 42–56. http://dx.doi.org/10.1016/j.tibs.2016.08.016.

Clarke-Bland, Charlotte E., Roslyn M. Bill, and Andrew Devitt. 2022. "Emerging Roles for AQP in Mammalian Extracellular Vesicles." *Biochimica et Biophysica Acta - Biomembranes* 1864(3): 183826. https://doi.org/10.1016/j.bbamem.2021.183826.

D'Arrigo, Giulia et al. 2021. "Astrocytes-Derived Extracellular Vesicles in Motion at the Neuron Surface: Involvement of the Prion Protein." *Journal of Extracellular Vesicles* 10(9).

Van Deun, Jan et al. 2014. "The Impact of Disparate Isolation Methods for Extracellular Vesicles on Downstream RNA Profiling." *Journal of Extracellular Vesicles* 3(1): 1–14.

Díaz-Amarilla, Pablo et al. 2011. "Phenotypically Aberrant Astrocytes That Promote Motoneuron Damage in a Model of Inherited Amyotrophic Lateral Sclerosis." *Proceedings of the National Academy of Sciences of the United States of America* 108(44): 18126–31.

Dickey, T. H., B. Song, and A. M. Pyle. 2019. "RNA Binding Activates RIG-I by Releasing an Autorepressed Signaling Domain." *Science Advances* 5(10).

Didonna, Alessandro et al. 2020. "Ataxin-1 Regulates B Cell Function and the Severity of Autoimmune Experimental Encephalomyelitis." *Proceedings of the National Academy of Sciences of the United States of America* 117(38): 23742–50.

Dobrowolny, Gabriella et al. 2021. "A Longitudinal Study Defined Circulating MicroRNAs as Reliable Biomarkers for Disease Prognosis and Progression in ALS Human Patients." *Cell death discovery* 7(1): 4.

Donoso-Quezada, Javier, Sergio Ayala-Mar, and José González-Valdez. 2021. “The Role of Lipids in Exosome Biology and Intercellular Communication: Function, Analytics and Applications.” *Traffic (Copenhagen, Denmark)* 22(7): 204–20.

Driedonks, Tom A.P. et al. 2020. “Y-RNA Subtype Ratios in Plasma Extracellular Vesicles Are Cell Type- Specific and Are Candidate Biomarkers for Inflammatory Diseases.” *Journal of Extracellular Vesicles* 9(1).

Driedonks, Tom A.P., and Esther N.M. Nolte-T’Hoen. 2019. “Circulating Y-RNAs in Extracellular Vesicles and Ribonucleoprotein Complexes; Implications for the Immune System.” *Frontiers in Immunology* 10(JAN): 1–15.

Dunker, William et al. 2021. “TDP-43 Prevents Endogenous RNAs from Triggering a Lethal RIG-I-Dependent Interferon Response.” *Cell Reports* 35(2): 108976. https://doi.org/10.1016/j.celrep.2021.108976.

Eitan, Chen et al. 2022. “Whole-Genome Sequencing Reveals That Variants in the Interleukin 18 Receptor Accessory Protein 3’UTR Protect against ALS.” *Nature Neuroscience* 25(4): 433–45.

Enderle, Daniel et al. 2015. “Characterization of RNA from Exosomes and Other Extracellular Vesicles Isolated by a Novel Spin Column-Based Method.” *PLoS ONE* 10(8): 1–19.

Eshima, Jarrett et al. 2023. “Molecular Subtypes of ALS Are Associated with Differences in Patient Prognosis.” *Nature Communications* 14(1).

Esser-Nobis, Katharina, Lauren D Hatfield, and Michael Jr Gale. 2020. “Spatiotemporal Dynamics of Innate Immune Signaling via RIG-I-like Receptors.” *Proceedings of the National Academy of Sciences of the United States of America* 117(27): 15778–88.

Fabbiano, Fabrizio et al. 2020. “RNA Packaging into Extracellular Vesicles: An Orchestra of RNA-Binding Proteins?” *Journal of Extracellular Vesicles* 10(2).

Fabbri, Muller et al. 2012. “MicroRNAs Bind to Toll-like Receptors to Induce Prometastatic Inflammatory Response.” *Proceedings of the National Academy of Sciences of the United States of America* 109(31).

Fallini, Claudia, Bilal Khalil, Courtney L. Smith, and Wilfried Rossoll. 2020. “Traffic Jam at the Nuclear Pore: All Roads Lead to Nucleocytoplasmic Transport Defects in ALS/FTD.” *Neurobiology of Disease* 140(March).

Feiler, Marisa S. et al. 2015. “TDP-43 Is Intercellularly Transmitted across Axon Terminals.” *Journal of Cell Biology* 211(4): 897–911.

Ferrara, Deborah, Laura Pasetto, Valentina Bonetto, and Manuela Basso. 2018. “Role of Extracellular Vesicles in Amyotrophic Lateral Sclerosis.” *Frontiers in neuroscience* 12: 574.

Friedman, Constantin S. et al. 2008. “The Tumour Suppressor CYLD Is a Negative Regulator of RIG-I-Mediated Antiviral Response.” *EMBO Reports* 9(9): 930–36.

Gabrielli, Martina et al. 2022. “Microglial Large Extracellular Vesicles Propagate Early Synaptic Dysfunction in Alzheimer’s Disease.” *Brain* 145(8): 2849–68.

Gagliardi, Delia, Nereo Bresolin, Giacomo Pietro Comi, and Stefania Corti. 2021. “Extracellular Vesicles and Amyotrophic Lateral Sclerosis: From Misfolded Protein Vehicles to Promising Clinical Biomarkers.” *Cellular and molecular life sciences : CMLS* 78(2): 561–72.

Gal, Jozsef et al. 2016. “ALS Mutant SOD1 Interacts with G3BP1 and Affects Stress Granule Dynamics.” *Acta neuropathologica* 132(4): 563–76.

Le Gall, Laura et al. 2022. “Muscle Cells of Sporadic Amyotrophic Lateral Sclerosis Patients Secrete Neurotoxic Vesicles.” *Journal of Cachexia, Sarcopenia and Muscle* 13(2): 1385–1402.

Gagliardi, S., Zucca, S., Pandini, C., Diamanti, L., Bordoni, M., Sproviero, D., Arigoni, M., Olivero, M., Pansarasa, O., Ceroni, M., Calogero, R., & Cereda, C. (2018). Long non-coding and coding RNAs characterization in Peripheral Blood Mononuclear Cells and Spinal Cord from Amyotrophic Lateral Sclerosis patients. Scientific reports, 8(1), 2378. https://doi.org/10.1038/s41598-018-20679-5

Garcia-Martin, Ruben et al. 2022. “MicroRNA Sequence Codes for Small Extracellular Vesicle Release and Cellular Retention.” *Nature* 601(7893): 446–51.

Gelibter, Stefano et al. 2022. “The Impact of Storage on Extracellular Vesicles: A Systematic Study.” *Journal of extracellular vesicles* 11(2): e12162.

Gerstberger, Stefanie, Markus Hafner, Manuel Ascano, and Thomas Tuschl. 2014. “Evolutionary Conservation and Expression of Human RNA-Binding Proteins and Their Role in Human Genetic Disease.” *Advances in experimental medicine and biology* 825: 1–55.

Gerstberger, Stefanie, Markus Hafner, and Thomas Tuschl. 2014. “A Census of Human RNA-Binding Proteins.” *Nature Reviews Genetics* 15(12): 829–45.

Goldstein, Laura H., and Sharon Abrahams. 2013. “Changes in Cognition and Behaviour in Amyotrophic Lateral Sclerosis: Nature of Impairment and Implications for Assessment.” *The Lancet Neurology* 12(4): 368–80. http://dx.doi.org/10.1016/S1474-4422(13)70026-7.

Gomes, Catarina, Cristina Escrevente, and Júlia Costa. 2010. “Mutant Superoxide Dismutase 1 Overexpression in NSC-34 Cells: Effect of Trehalose on Aggregation, TDP-43 Localization and Levels of Co-Expressed Glycoproteins.” *Neuroscience letters* 475(3): 145–49.

Gómora-García, Juan Carlos, Cristian Gerónimo-Olvera, Xochitl Pérez-Martínez, and Lourdes Massieu. 2021. “IRE1α RIDD Activity Induced under ER Stress Drives Neuronal Death by the Degradation of 14-3-3 θ MRNA in Cortical Neurons during Glucose Deprivation.” *Cell Death Discovery* 7(1). http://dx.doi.org/10.1038/s41420-021-00518-9.

Gu, Zuguang, Roland Eils, and Matthias Schlesner. 2016. “Complex Heatmaps Reveal Patterns and Correlations in Multidimensional Genomic Data.” *Bioinformatics* 32(18): 2847–49.

Guan, Lihuan, Karen C Crasta, and Andrea B Maier. 2022. “Assessment of Cell Cycle Regulators in Human Peripheral Blood Cells as Markers of Cellular Senescence.” *Ageing research reviews* 78: 101634.

Hao, Qian et al. 2015. “ A Non-canonical Role of the P97 Complex in RIG -I Antiviral Signaling .” *The EMBO Journal* 34(23): 2903–20.

Hardiman, Orla et al. 2017. “Amyotrophic Lateral Sclerosis.” *Nature Reviews Disease Primers* 3.

Van Harten, Alexandra C.M., Hemali Phatnani, and Serge Przedborski. 2021. “Non-Cell-Autonomous Pathogenic Mechanisms in Amyotrophic Lateral Sclerosis.” *Trends in Neurosciences* 44(8): 658–68. https://doi.org/10.1016/j.tins.2021.04.008.

Hondele, Maria et al. 2019. “DEAD-Box ATPases Are Global Regulators of Phase-Separated Organelles.” *Nature* 573(7772): 144–48. http://dx.doi.org/10.1038/s41586-019-1502-y.

Horbay, Rostyslav et al. 2022. “Role of Ceramides and Lysosomes in Extracellular Vesicle Biogenesis, Cargo Sorting and Release.” *International journal of molecular sciences* 23(23).

Iguchi, Yohei et al. 2016. “Exosome Secretion Is a Key Pathway for Clearance of Pathological TDP-43.” *Brain : a journal of neurology* 139(Pt 12): 3187–3201.

Jackson, Noel A., Marcos J. Guerrero-Muñoz, and Diana L. Castillo-Carranza. 2022. “The Prion-like Transmission of Tau Oligomers via Exosomes.” *Frontiers in Aging Neuroscience* 14(August): 1–9.

Jankowsky, Eckhard. 2011. “RNA Helicases at Work: Binding and Rearranging.” *Trends in Biochemical Sciences* 36(1): 19–29. http://dx.doi.org/10.1016/j.tibs.2010.07.008.

Jarmoskaite, Inga, and Rick Russell. 2014. “RNA Helicase Proteins as Chaperones and Remodelers.” *Annual Review of Biochemistry* 83: 697–725.

Jarry, J. et al. 2014. “The Validity of Circulating MicroRNAs in Oncology: Five Years of Challenges and Contradictions.” *Molecular Oncology* 8(4): 819–29.

Jeon, Hyejin et al. 2012. “Plasminogen Activator Inhibitor Type 1 Regulates Microglial Motility and Phagocytic Activity.” *Journal of Neuroinflammation* 9: 1–22.

Jin, Yong et al. 2022. “Extracellular Signals Regulate the Biogenesis of Extracellular Vesicles.” *Biological Research* 55(1): 1–16. https://doi.org/10.1186/s40659-022-00405-2.

Karlsen, Tommy A, and Jan E Brinchmann. 2013. “Liposome Delivery of MicroRNA-145 to Mesenchymal Stem Cells Leads to Immunological off-Target Effects Mediated by RIG-I.” *Molecular therapy : the journal of the American Society of Gene Therapy* 21(6): 1169–81.

Katsu, Masataka et al. 2019. “MicroRNA Expression Profiles of Neuron-Derived Extracellular Vesicles in Plasma from Patients with Amyotrophic Lateral Sclerosis.” *Neuroscience Letters* 708(June): 134176. https://doi.org/10.1016/j.neulet.2019.03.048.

Kim, Kyoung Mi et al. 2017. “RNA in Extracellular Vesicles.” *Wiley interdisciplinary reviews. RNA* 8(4).

Kmetzsch, Virgilio et al. 2021. “Plasma MicroRNA Signature in Presymptomatic and Symptomatic Subjects with C9orf72-Associated Frontotemporal Dementia and Amyotrophic Lateral Sclerosis.” *Journal of neurology, neurosurgery, and psychiatry* 92(5): 485–93.

Kmetzsch, Virgilio et al. 2022. “MicroRNA Signatures in Genetic Frontotemporal Dementia and Amyotrophic Lateral Sclerosis.” *Annals of Clinical and Translational Neurology* 9(11): 1778–91.

Kudo, Lili C. et al. 2010. “Integrative Gene-Tissue Microarray-Based Approach for Identification of Human Disease Biomarkers: Application to Amyotrophic Lateral Sclerosis.” *Human Molecular Genetics* 19(16): 3233–53.

Kugeratski, Fernanda G. et al. 2021. 23 Nature Cell Biology *Quantitative Proteomics Identifies the Core Proteome of Exosomes with Syntenin-1 as the Highest Abundant Protein and a Putative Universal Biomarker*. Springer US. http://dx.doi.org/10.1038/s41556-021-00693-

y.

Laneve, P., Tollis, P., & Caffarelli, E. (2021). RNA Deregulation in Amyotrophic Lateral Sclerosis: The Noncoding Perspective. *International journal of molecular sciences*, *22*(19), 10285. https://doi.org/10.3390/ijms221910285

Lässig, Charlotte et al. 2015. "ATP Hydrolysis by the Viral RNA Sensor RIG-I Prevents Unintentional Recognition of Self-RNA." *eLife* 4.

Lee, Na-Rae et al. 2018. "Activation of RIG-I-Mediated Antiviral Signaling Triggers Autophagy Through the MAVS-TRAF6-Beclin-1 Signaling Axis." *Frontiers in immunology* 9: 2096.

Leidal, Andrew M et al. 2020. "The LC3-Conjugation Machinery Specifies the Loading of RNA-Binding Proteins into Extracellular Vesicles." *Nature cell biology* 22(2): 187–99.

Leitão, Ana Lúcia, Marina C. Costa, and Francisco J. Enguita. 2015. "Open Accessunzippers, Resolvers and Sensors: A Structural and Functional Biochemistry Tale of RNA Helicases." *International Journal of Molecular Sciences* 16(2): 2269–93.

Lerner, M R, J A Boyle, J A Hardin, and J A Steitz. 1981. "Two Novel Classes of Small Ribonucleoproteins Detected by Antibodies Associated with Lupus Erythematosus." *Science (New York, N.Y.)* 211(4480): 400–402.

Li, Shufang et al. 2022. "MiR-203, Fine-Tunning Neuroinflammation by Juggling Different Components of NF-KB Signaling." *Journal of neuroinflammation* 19(1): 84.

Liu, Feng, Su Wu, Hongwei Ren, and Jun Gu. 2011. "Klotho Suppresses RIG-I-Mediated Senescence-Associated Inflammation." *Nature cell biology* 13(3): 254–62.

Liu, Guan Qun, and Michaela U. Gack. 2020. "Distinct and Orchestrated Functions of RNA Sensors in Innate Immunity." *Immunity* 53(1): 26–42. https://doi.org/10.1016/j.immuni.2020.03.017.

Liu, GuanQun et al. 2015. "Influenza A Virus Panhandle Structure Is Directly Involved in RIG-I Activation and Interferon Induction." *Journal of Virology* 89(11): 6067–79.

Liu, GuanQun et al. 2018. "Nuclear-Resident RIG-I Senses Viral Replication Inducing Antiviral Immunity." *Nature communications* 9(1): 3199.

Lööv, Camilla et al. 2016. "α-Synuclein in Extracellular Vesicles: Functional Implications and Diagnostic Opportunities." *Cellular and Molecular Neurobiology* 36(3): 437–48.

Love, Michael I., Wolfgang Huber, and Simon Anders. 2014. “Moderated Estimation of Fold Change and Dispersion for RNA-Seq Data with DESeq2.” *Genome Biology* 15(12): 1–21.

Macnair, Laura et al. 2016. “MTHFSD and DDX58 Are Novel RNA-Binding Proteins Abnormally Regulated in Amyotrophic Lateral Sclerosis.” *Brain* 139(1): 86–100.

Malathi, Krishnamurthy, Beihua Dong, Michael Gale, and Robert H. Silverman. 2007. “Small Self-RNA Generated by RNase L Amplifies Antiviral Innate Immunity.” *Nature* 448(7155): 816–19.

McAlary, Luke, Steven S. Plotkin, Justin J. Yerbury, and Neil R. Cashman. 2019. “Prion-Like Propagation of Protein Misfolding and Aggregation in Amyotrophic Lateral Sclerosis.” *Frontiers in Molecular Neuroscience* 12(November): 1–21.

McCauley, Madelyn E et al. 2020. “C9orf72 in Myeloid Cells Suppresses STING-Induced Inflammation.” *Nature* 585(7823): 96–101.

McCluskey, Gavin et al. 2022. “Extracellular Vesicles in Amyotrophic Lateral Sclerosis.” *Life (Basel, Switzerland)* 13(1).

Mead, Richard J. et al. 2023. “Amyotrophic Lateral Sclerosis: A Neurodegenerative Disorder Poised for Successful Therapeutic Translation.” *Nature Reviews Drug Discovery* 22(3): 185–212.

Mullani, Nowsheen et al. 2021. “Reduced RNA Turnover as a Driver of Cellular Senescence.” *Life science alliance* 4(3).

Nabet, Barzin Y. et al. 2017. “Exosome RNA Unshielding Couples Stromal Activation to Pattern Recognition Receptor Signaling in Cancer.” *Cell* 170(2): 352-366.e13. http://dx.doi.org/10.1016/j.cell.2017.06.031.

Nguyen, Thuy Linh et al. 2020. “The Internal Loops in the Lower Stem of Primary MicroRNA Transcripts Facilitate Single Cleavage of Human Microprocessor.” *Nucleic acids research* 48(5): 2579–93.

van Niel, Guillaume et al. 2022. “Challenges and Directions in Studying Cell–Cell Communication by Extracellular Vesicles.” *Nature Reviews Molecular Cell Biology* 23(5): 369–82.

Van Niel, Guillaume, Gisela D’Angelo, and Graça Raposo. 2018. “Shedding Light on the Cell Biology of Extracellular Vesicles.” *Nature Reviews Molecular Cell Biology* 19(4): 213–28. http://dx.doi.org/10.1038/nrm.2017.125.

Nijssen, Jik, Laura H. Comley, and Eva Hedlund. 2017. “Motor Neuron Vulnerability and Resistance in Amyotrophic Lateral Sclerosis.” *Acta Neuropathologica* 133(6): 863–85.

Notarangelo, Michela et al. 2019. “Ultrasensitive Detection of Cancer Biomarkers by Nickel-Based Isolation of Polydisperse Extracellular Vesicles from Blood.” *EBioMedicine* 43: 114–26. https://doi.org/10.1016/j.ebiom.2019.04.039.

Notarangelo, Michela et al. 2020. “Rapid Nickel-Based Isolation of Extracellular Vesicles from Different Biological Fluids.” *Bio-Protocol* 10(3): 1–12.

O’Brien, Killian et al. 2020. “RNA Delivery by Extracellular Vesicles in Mammalian Cells and Its Applications.” *Nature Reviews Molecular Cell Biology* 21(10): 585–606. http://dx.doi.org/10.1038/s41580-020-0251-y.

Onódi, Zsófia et al. 2018. “Isolation of High-Purity Extracellular Vesicles by the Combination of Iodixanol Density Gradient Ultracentrifugation and Bind-Elute Chromatography From Blood Plasma.” *Frontiers in physiology* 9: 1479.

Ouweneel, Amber B., Michael J. Thomas, and Mary G. Sorci-Thomas. 2020. “The Ins and Outs of Lipid Rafts: Functions in Intracellular Cholesterol Homeostasis, Microparticles, and Cell Membranes.” *Journal of Lipid Research* 61(5): 676–86. http://dx.doi.org/10.1194/jlr.TR119000383.

Ozato, Keiko, Dong Mi Shin, Tsung Hsien Chang, and Herbert C. Morse. 2008. “TRIM Family Proteins and Their Emerging Roles in Innate Immunity.” *Nature Reviews Immunology* 8(11): 849–60.

Ozgur, Sevim et al. 2015. “The Conformational Plasticity of Eukaryotic RNA-Dependent ATPases.” *The FEBS journal* 282(5): 850–63.

Pantazi, Paschalia et al. 2022. “Distinct Non-Coding RNA Cargo of Extracellular Vesicles from M1 and M2 Human Primary Macrophages.” *Journal of Extracellular Vesicles* 11(12).

Pérez-Boza, Jennifer, Michelle Lion, and Ingrid Struman. 2018. “Exploring the RNA Landscape of Endothelial Exosomes.” *RNA (New York, N.Y.)* 24(3): 423–35.

Pessina, Fabio et al. 2021. “DNA Damage Triggers a New Phase in Neurodegeneration.” *Trends in Genetics* 37(4): 337–54. https://doi.org/10.1016/j.tig.2020.09.006.

Pinto, Sara et al. 2017. “Exosomes from NSC-34 Cells Transfected with HSOD1-G93A Are Enriched in Mir-124 and Drive Alterations in Microglia Phenotype.” *Frontiers in*

Neuroscience 11(MAY).

Provenzano, F., Nyberg, S., Giunti, D., Torazza, C., Parodi, B., Bonifacino, T., Usai, C., Kerlero de Rosbo, N., Milanese, M., Uccelli, A., Shaw, P. J., Ferraiuolo, L., & Bonanno, G. (2022). Micro-RNAs Shuttled by Extracellular Vesicles Secreted from Mesenchymal Stem Cells Dampen Astrocyte Pathological Activation and Support Neuroprotection in In-Vitro Models of ALS. *Cells*, *11*(23), 3923. https://doi.org/10.3390/cells11233923

Ramírez-Nuñez, Omar et al. 2021. "Nuclear Lipidome Is Altered in Amyotrophic Lateral Sclerosis: A Pilot Study." *Journal of Neurochemistry* 158(2): 482–99.

Raudvere, Uku et al. 2019. "G:Profiler: A Web Server for Functional Enrichment Analysis and Conversions of Gene Lists (2019 Update)." *Nucleic Acids Research* 47(W1): W191–98.

Rehwinkel, Jan, and Michaela U Gack. 2020. "RIG-I-like Receptors: Their Regulation and Roles in RNA Sensing." *Nature reviews. Immunology* 20(9): 537–51.

van Rheenen, Wouter et al. 2021. "Common and Rare Variant Association Analyses in Amyotrophic Lateral Sclerosis Identify 15 Risk Loci with Distinct Genetic Architectures and Neuron-Specific Biology." *Nature genetics* 53(12): 1636–48.

Da Ros, Matteo et al. 2021. "Wild-Type and Mutant SOD1 Localizes to RNA-Rich Structures in Cells and Mice but Does Not Bind RNA." *Journal of neurochemistry* 156(4): 524–38.

Rosen, Daniel R. et al. 1993. "Mutations in Cu/Zn Superoxide Dismutase Gene Are Associated with Familial Amyotrophic Lateral Sclerosis." *Nature* 362(6415): 59–62.

Rotunno, Melissa S, and Daryl A Bosco. 2013. "An Emerging Role for Misfolded Wild-Type SOD1 in Sporadic ALS Pathogenesis." *Frontiers in cellular neuroscience* 7: 253.

Runge, Simon et al. 2014. "In Vivo Ligands of MDA5 and RIG-I in Measles Virus-Infected Cells." *PLoS Pathogens* 10(4).

Ryan, Marie, Mark Heverin, Russell L. McLaughlin, and Orla Hardiman. 2019. "Lifetime Risk and Heritability of Amyotrophic Lateral Sclerosis." *JAMA Neurology* 76(11): 1367–74.

Saá, Paula et al. 2014. "First Demonstration of Transmissible Spongiform Encephalopathy-Associated Prion Protein (PrPTSE) in Extracellular Vesicles from Plasma of Mice Infected with Mouse-Adapted Variant Creutzfeldt-Jakob Disease by in Vitro Amplification." *Journal of Biological Chemistry* 289(42): 29247–60.

Sánchez-Aparicio, M T et al. 2017. "Subcellular Localizations of RIG-I, TRIM25, and MAVS

Complexes." *Journal of virology* 91(2).

Sánchez, Ivelisse, Eudald Balagué, and Antoni Matilla-Dueñas. 2016. "Ataxin-1 Regulates the Cerebellar Bioenergetics Proteome through the GSK3β-MTOR Pathway Which Is Altered in Spinocerebellar Ataxia Type 1 (SCA1)." *Human molecular genetics* 25(18): 4021–40.

Schnell, Gretja, Yueh Ming Loo, Joseph Marcotrigiano, and Michael Gale. 2012. "Uridine Composition of the Poly-U/UC Tract of HCV RNA Defines Non-Self Recognition by RIG-I." *PLoS Pathogens* 8(8).

Scoles, Daniel R et al. 2020. "ALS-Associated Genes in SCA2 Mouse Spinal Cord Transcriptomes." *Human molecular genetics* 29(10): 1658–72.

Silverman, Judith M. et al. 2019. "CNS-Derived Extracellular Vesicles from Superoxide Dismutase 1 (SOD1)G93A ALS Mice Originate from Astrocytes and Neurons and Carry Misfolded SOD1." *Journal of Biological Chemistry* 294(10): 3744–59. http://dx.doi.org/10.1074/jbc.RA118.004825.

Song, SungWon et al. 2016. "Major Histocompatibility Complex Class I Molecules Protect Motor Neurons from Astrocyte-Induced Toxicity in Amyotrophic Lateral Sclerosis." *Nature medicine* 22(4): 397–403.

Sork, Helena et al. 2018. "Heterogeneity and Interplay of the Extracellular Vesicle Small RNA Transcriptome and Proteome." *Scientific Reports* 8(1): 1–12.

Tamaki, Yoshitaka, and Makoto Urushitani. 2022. "Molecular Dissection of TDP-43 as a Leading Cause of ALS/FTLD." *International Journal of Molecular Sciences* 23(20).

Tazelaar, Gijs H P et al. 2020. "ATXN1 Repeat Expansions Confer Risk for Amyotrophic Lateral Sclerosis and Contribute to TDP-43 Mislocalization." *Brain communications* 2(2): fcaa064.

Théry, Clotilde et al. 2018. "Minimal Information for Studies of Extracellular Vesicles 2018 (MISEV2018): A Position Statement of the International Society for Extracellular Vesicles and Update of the MISEV2014 Guidelines." *Journal of extracellular vesicles* 7(1): 1535750.

Tóth, Eszter et al. 2021. "Formation of a Protein Corona on the Surface of Extracellular Vesicles in Blood Plasma." *Journal of Extracellular Vesicles* 10(11).

Tunçer, Sinem et al. 2018. "Low Dose Dimethyl Sulfoxide Driven Gross Molecular Changes Have the Potential to Interfere with Various Cellular Processes." *Scientific reports* 8(1): 14828.

Vahsen, Björn F. et al. 2021. "Non-Neuronal Cells in Amyotrophic Lateral Sclerosis — from

Pathogenesis to Biomarkers." *Nature Reviews Neurology* 17(6): 333–48.

Valadi, Hadi et al. 2007. "Exosome-Mediated Transfer of MRNAs and MicroRNAs Is a Novel Mechanism of Genetic Exchange between Cells." *Nature cell biology* 9(6): 654–59.

Varcianna, André et al. 2019. "Micro-RNAs Secreted through Astrocyte-Derived Extracellular Vesicles Cause Neuronal Network Degeneration in C9orf72 ALS." *EBioMedicine* 40: 626–35.

Verheijen, M et al. 2019. "DMSO Induces Drastic Changes in Human Cellular Processes and Epigenetic Landscape in Vitro." *Scientific reports* 9(1): 4641.

Wang, Dan et al. 2021. "Ginsenoside Rb1 Attenuates Microglia Activation to Improve Spinal Cord Injury via MicroRNA-130b-5p/TLR4/NF-KB Axis." *Journal of cellular physiology* 236(3): 2144–55.

Wang, Lijun, David H. Gutmann, and Raymond P. Roos. 2011. "Astrocyte Loss of Mutant SOD1 Delays ALS Disease Onset and Progression in G85R Transgenic Mice." *Human Molecular Genetics* 20(2): 286–93.

Wang, Wenzhang et al. 2016. "The Inhibition of TDP-43 Mitochondrial Localization Blocks Its Neuronal Toxicity." *Nature Medicine* 22(8): 869–78.

Weydt, Patrick, Eric C. Yuen, Bruce R. Ransom, and Thomas Möller. 2004. "Increased Cytotoxic Potential of Microglia from ALS-Transgenic Mice." *Glia* 48(2): 179–82.

Witzel, Simon et al. 2022. "Fast versus Slow Disease Progression in Amyotrophic Lateral Sclerosis-Clinical and Genetic Factors at the Edges of the Survival Spectrum." *Neurobiology of aging* 119: 117–26.

Wolf, Martin et al. 2022. "A Functional Corona around Extracellular Vesicles Enhances Angiogenesis, Skin Regeneration and Immunomodulation." *Journal of Extracellular Vesicles* 11(4).

Xian, Huifang et al. 2020. "LRRC59 Modulates Type I Interferon Signaling by Restraining the SQSTM1/P62-Mediated Autophagic Degradation of Pattern Recognition Receptor DDX58/RIG-I." *Autophagy* 16(3): 408–18. https://doi.org/10.1080/15548627.2019.1615303.

Xiao, Qin et al. 2007. "Mutant SOD1G93A Microglia Are More Neurotoxic Relative to Wild-Type Microglia." *Journal of Neurochemistry* 102(6): 2008–19.

Xiong, Luyang et al. 2022. “Inflammation-Dependent Oxidative Stress Metabolites as a Hallmark of Amyotrophic Lateral Sclerosis.” *Free Radical Biology and Medicine* 178: 125–33. https://doi.org/10.1016/j.freeradbiomed.2021.11.031.

Xu, Xiao xiao et al. 2018. “RIG-I: A Multifunctional Protein beyond a Pattern Recognition Receptor.” *Protein and Cell* 9(3): 246–53.

Yáñez-Mó, María et al. 2015. “Biological Properties of Extracellular Vesicles and Their Physiological Functions.” *Journal of extracellular vesicles* 4: 27066.

Yelick, Julia et al. 2020. “Elevated Exosomal Secretion of MiR-124-3p from Spinal Neurons Positively Associates with Disease Severity in ALS.” *Experimental neurology* 333: 113414.

Yu, W, M Clyne, M J Khoury, and M Gwinn. 2010. “Phenopedia and Genopedia: Disease-Centered and Gene-Centered Views of the Evolving Knowledge of Human Genetic Associations.” *Bioinformatics (Oxford, England)* 26(1): 145–46.

Zetterström, Per, Peter M Andersen, Thomas Brännström, and Stefan L Marklund. 2011. “Misfolded Superoxide Dismutase-1 in CSF from Amyotrophic Lateral Sclerosis Patients.” *Journal of neurochemistry* 117(1): 91–99.

Zhang, Hong Xin et al. 2013. “Rig-I Regulates NF-KB Activity through Binding to Nf-Kb1 3′-UTR MRNA.” *Proceedings of the National Academy of Sciences of the United States of America* 110(16): 6459–64.

Zhao, Lianzhong et al. 2015. “Identification of Cellular MicroRNA-136 as a Dual Regulator of RIG-I-Mediated Innate Immunity That Antagonizes H5N1 IAV Replication in A549 Cells.” *Scientific Reports* 5(October): 1–13.

Zhao, Weihua et al. 2010. “Extracellular Mutant SOD1 Induces Microglial-Mediated Motoneuron Injury.” *Glia* 58(2): 231–43.

Zomer, Anoek, Sander Christiaan Steenbeek, Carrie Maynard, and Jacco Van Rheenen. 2016. “Studying Extracellular Vesicle Transfer by a Cre-LoxP Method.” *Nature Protocols* 11(1): 87–101.

Acknowledgments

With these few words, I encourage the reader to think that none of this work could have existed without the presence of many people.

I would like to acknowledge Prof. Vito D'Agostino, who gave me the opportunity to work in his lab, to explore different approaches and to share my work with many collaborators in Italy and abroad. I thank the group of Prof. Giambattista Bonanno for the part regarding SOD1 mouse model samples. A particular remark goes to Prof. Manuel Portero-Otin from the University of Lleida and all of the friendly researchers I met there; you represented an enlightening part of my professional and personal life.

I want to sincerely thank all of the members of my PhD evaluation committee, Prof. Alberto Inga, Prof. Marta Biagioli, Prof. Marco Milanese and Dr. Orazio Fortunato, who critically read through my thesis and provided insightful and careful suggestions. I really appreciated your kindness and scientific integrity in your comments.

I thank the PhD Program in Biomolecular Sciences and the exiting and living environment of CIBIO department. With this, I extend my gratitude to anyone who helped me and to anyone I had the pleasure to give a hand to. CIBIO facilities, especially NGS and HTS that allowed me to learn and exploit cutting-edge lab equipment and technologies.

A particular notice will naturally go to the closest people of all, my lab mates from the FAB-ulous Purple6 Lab! Thank you for all the laughs and all the good moments, to the people that were active part of the life in the lab and outside of it. To the people that passed by, to the ones who left, to the ones who will stay, Purple6 will always be an ideal to chase, a metaphorical place for unplugging from hard times! Thank you all, may the FABlab be with you!

A special thanks to the most special person I've met during these years. It was an amazing journey and a huge growth opportunity to be able to trouble-shoot with you and to face different challenges in multiple ways. I cannot wait to see what life has saved for us in the future. You deserved to be mentioned inside these "words" too, thank you Jess.

Finally, I wish to thank my family and my dearest friends that always encouraged me to pursue the truth and to look for the right path for my life. You will always guide me with your support, even from far away.